Max-Planck-Institut
für Meteorologie

MAX-PLANCK-GESELLSCHAFT

The influence of precipitating solar and magnetospheric energetic charged particles on the entire atmosphere
Simulations with HAMMONIA

Jens Kieser

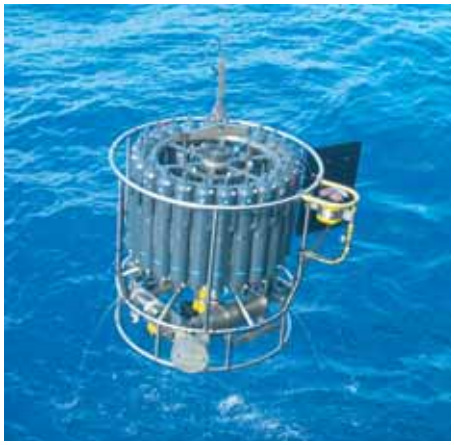

Berichte zur Erdsystemforschung 98/2011

Reports on Earth System Science

Hinweis

Die Berichte zur Erdsystemforschung werden vom Max-Planck-Institut für Meteorologie in Hamburg in unregelmäßiger Abfolge herausgegeben.

Sie enthalten wissenschaftliche und technische Beiträge, inklusive Dissertationen.

Die Beiträge geben nicht notwendigerweise die Auffassung des Instituts wieder.

Die "Berichte zur Erdsystemforschung" führen die vorherigen Reihen "Reports" und "Examensarbeiten" weiter.

Notice

The Reports on Earth System Science are published by the Max Planck Institute for Meteorology in Hamburg. They appear in irregular intervals.

They contain scientific and technical contributions, including Ph. D. theses.

The Reports do not necessarily reflect the opinion of the Institute.

The "Reports on Earth System Science" continue the former "Reports" and "Examensarbeiten" of the Max Planck Institute.

Anschrift / Address

Max-Planck-Institut für Meteorologie
Bundesstrasse 53
20146 Hamburg
Deutschland

Tel.: +49-(0)40-4 11 73-0
Fax: +49-(0)40-4 11 73-298
Web: www.mpimet.mpg.de

Layout:

Bettina Diallo, PR & Grafik

Titelfotos:
vorne:
Christian Klepp - Jochem Marotzke - Christian Klepp
hinten:
Clotilde Dubois - Christian Klepp - Katsumasa Tanaka

Berichte zur Erdsystemforschung 98/2011

The influence of precipitating solar and magnetospheric energetic charged particles on the entire atmosphere Simulations with HAMMONIA

Jens Kieser

aus Karl-Marx-Stadt

Hamburg 2011

Reports on Earth System Science 98/2011

ISSN 1614-1199

Jens Kieser
Max-Planck-Institut für Meteorologie
Bundesstrasse 53
20146 Hamburg
Germany

Als Dissertation angenommen
vom Department Geowissenschaften der Universität Hamburg

auf Grund der Gutachten von
Prof. Dr. Guy P. Brasseur
und
Dr. Hauke Schmidt

Hamburg, den 12. Juli 2011
Prof. Dr. Jürgen Oßenbrügge
Leiter des Departments für Geowissenschaften

ISSN 1614-1199

The influence of precipitating solar and magnetospheric energetic charged particles on the entire atmosphere
Simulations with HAMMONIA

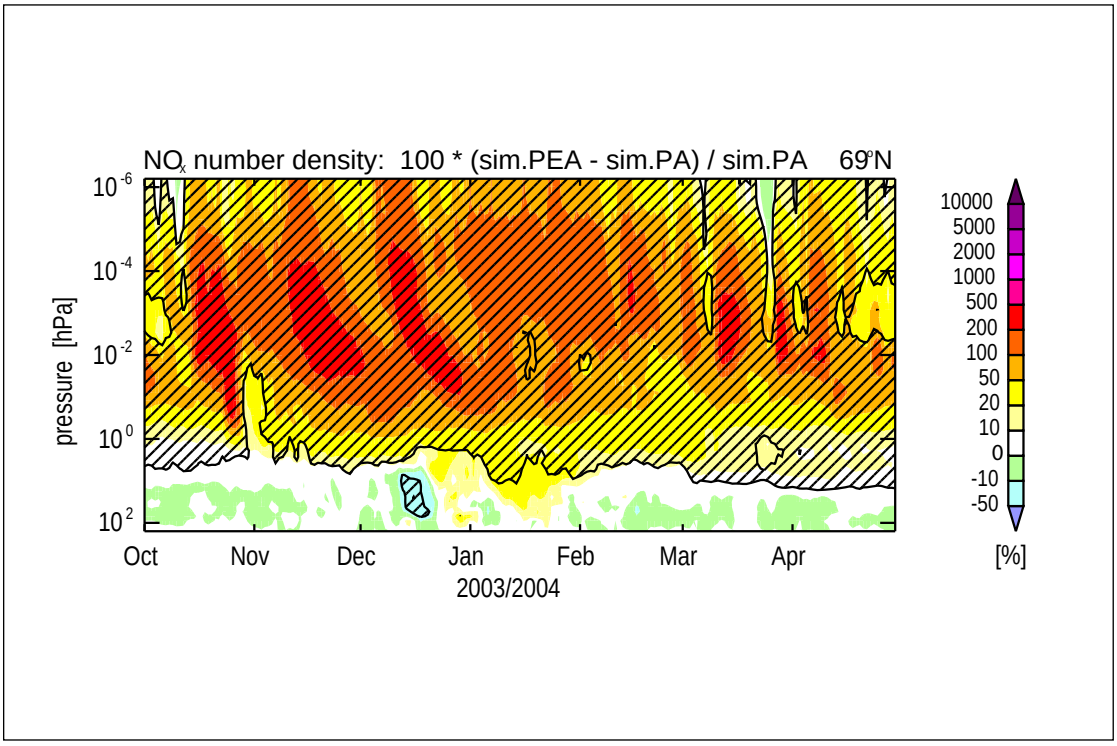

Jens Kieser

Hamburg 2011

Cover picture sources

Reprinted from Figure 6.15 in the text. It shows the simulated influence of precipitating electrons on NO_x at geomagnetic latitude of 69°N.

Abstract

The General Circulation and Chemisty model HAMMONIA (Hamburg Model of the Neutral and Ionized Atmosphere) is used in order to study the influence of an extreme solar energetic particle storm on the Earth's atmosphere. HAMMONIA uses ionisation rates describing precipitation of protons, electrons, and α-particles of solar and magnetospheric origin into the entire atmosphere up to the thermosphere. This allows to consider interactions between the effects of the prominent particle precipitation event which is dominated by solar protons and the effects of subsequent solar and magnetospheric particle precipitation events. The geomagnetically very active period from October 2003 to April 2004 is considered which includes one of the strongest solar particle precipitation events ever observed in the atmosphere. With the background of an assessment of potential effects of particle storms on the terrestrial climate the study is focussed on the influence of energetic charged particles on the atmospheric chemical composition. Aspects of energetics and dynamics are also considered. One important question is concerned with the contributions of single particle components. Moreover, the influence of precipitating particles on processes which cause temperature changes in the upper atmosphere are studied.
It is shown that particularly in the stratosphere and mesosphere at high latitudes the concentration of NO_x ($NO + NO_2$) is elevated by several thousand percents due to the influence of high-energy protons whose appearance is more or less confined to the solar particle event. While the influence of protons considerably decreases after a few weeks, and the contribution of α-particles is in general marginal, the NO_x concentration in the upper stratosphere and above at auroral and polar latitudes is controlled by precipitating electrons. In the middle atmosphere the NO_x concentration is substantially enhanced by descending NO_x originating from the thermosphere where it is primarily induced by electron precipitation. A comparison with observational studies indicates that downward transport of NO_x is underestimated by HAMMONIA. Therefore, it is guessed that the influence of electrons on the middle atmosphere is even stronger than predicted.
The influence of particle precipitation on HO_x ($H + OH + HO_2$) is confined to the middle atmosphere. In the summer hemisphere significant enhancements of the HO_x number density are confined to the short period of the prominent proton precipitation event. While the increase of the HO_x number density in the summer hemisphere is less than 50%, at high latitudes of the winter hemisphere precipitating protons and electrons cause a series of short-term increases of several thousand percents. However, except from a few events in October and early November, the resulting HO_x concentrations are very small.
In the mesosphere at high latitudes the prominent particle precipitation event is associated with an ozone depletion of more than 50% in summer and more than 75% in winter. Further events dominated by electron precipitation lead to short-term ozone depletions similar in magnitude. In the stratosphere in winter a longer-term ozone depletion of up to 30% is predicted primarily due to precipitating protons. Here, the

contribution of precipitating electrons is in general lower than 20%. Considering a possible underestimation of ozone depletion due to underestimation of NO_x decent, it is guessed that electron precipitating provides an important contribution to the longer-term ozone depletion.
A temperature increase of more than 10 K is shown for nearly the entire lower thermosphere resulting from particle-induced increases of chemical heating and heating through dissipative interactions between neutral and ionized gas. The influence of these dissipative processes leads to a cooling of more than 5 K in the lower thermosphere in summer at high latitues.
This work points out that precipitation of electrons must be taken into account in addition to high-energy solar protons when the effects of severe solar particle storms on the Earth's atmosphere are studied.

Zusammenfassung

Das Allgemeine-Zirkulations- und Chemiemodell HAMMONIA (Hamburg Model of the Neutral and Ionized Atmosphere) wird verwendet um den Einfluss eines außergewöhnlich starken solaren Partikelsturms auf die gesamte Atmosphäre der Erde zu untersuchen. Hierzu verwendet HAMMONIA Ionisationsraten, welche den Einfall von Protonen, Elektronen, und α-Partikeln solaren und magnetosphärischen Ursprungs in die gesamte Atmosphäre bis in die Thermosphäre beschreiben. Dadurch können die Auswirkungen des Ereigisses, welches durch solare Protonen dominiert wird, im Zusammenspiel mit dem Einfluss nachfolgender solarer und magnetosphärischer Partikelereignisse betrachtet werden. Hierzu wird der Zeitraum von Oktober 2003 bis April 2004 betrachtet, welcher sich durch starke geomagnetische Aktivität auszeichnet und der eines der stärksten jemals beobachteten solaren Partikelevents beinhaltet.
Vor dem Hintergrund einer Beurteilung möglicher Auswirkungen von Partikelstürmen auf das terrestrische Klima beziehen sich die Untersuchungen besonders auf den Einfluss energetisch geladener Partikel auf die chemische Zusammensetzung der Atmosphäre, aber auch auf Aspekte der Energetik und Dynamik. Von besonderem Interesse ist hierbei die Klärung der Frage, welchen Beitrag die einzelnen Partikelkomponenten leisten. Außerdem wird der Einfluss von Partikeln auf verschiedene Prozesse untersucht, welche Temperaturänderungen in der oberen Atmosphäre hervorrufen.
Es wird gezeigt, dass der massive Einfall von hochenergetischen Protonen, welcher nahezu auf das starke solare Partikel-Ereignis beschränkt ist, die Teilchenzahldichte von NO_x ($NO + NO_2$) besonders in der Stratosphäre und Mesosphäre hoher Breiten um mehrere tausend Prozent erhöht. Dabei wird in diesen Regionen nahezu alles NO_x durch den Einfluss von Protonen gebildet. Während der Einfluss der Protonen bereits nach einigen Wochen stark abnimmt und α-Teilchen generell kaum einen signifikanten Beitrag liefern, wird die NO_x-Konzentration in der oberen Stratosphäre, sowie in der Mesosphäre und Thermosphäre der Aurora- und Polargebiete über mehrere Monate, besonders im Winter, durch den Einfall von Elektronen bestimmt. Dabei wird die NO_x-konzenration in der mittleren Atmosphäre wesentlich durch abwärts transportiertes NO_x erhöht, welches hauptsächlich durch den Einfluss von Elektronen in der Thermosphäre produziert wurde. Vergleiche mit Messungen deuten an, dass der Abwärtstransport von NO_x in HAMMONIA noch deutlich unterschätzt wird. Das lässt vermuten, dass der tatsächliche Einfluss von Elektronen auf die mittlere Atmosphäre noch bedeutender ist.
Der Einfluss von Partikeln auf HO_x ($H + OH + HO_2$) beschränkt sich hauptsächlich auf die mittlere Atmosphäre. Während hier die HO_x-Teilchenzahldichte in der Sommerhemisphäre nur kurzfristig durch den starken Protoneneinfall um bis zu 50% erhöht wird, tragen in der Winterhemisphäre sowohl Protonen als auch Elektronen zu kurzfristigen Erhöhungen um mehrere tausend Prozent bei. Abgesehen vom starken protonendominierten Event und wenigen weiteren Events liegen die resul-

tierenden Konzentrationen jedoch auf sehr niedrigem Niveau.
In der Mesosphäre in hohen Breiten findet man in Verbindung mit dem außergewöhnlich starken Partikelevent eine kurzfristige Ozonabnahme von über 50% im Sommer und über 75% im Winter. Weitere durch Elektronen dominierte Partikelevents sorgen kurzfristig für ähnlich starke Abnahmen. Die Simulationen zeigen eine langfristige um bis zu 30%-ige Ozonabnahme in der Stratosphäre im Winter. Diese wird im wesentlichen durch Protoneneinfall hervorgerufen, während der Einfluss von Elektronen im Allgemeinen weniger als 20% beträgt. Berücksichtigt man jedoch eine mögliche Unterschätzung der Ozonabnahme durch abwärts transportiertes NO_x, lässt sich vermuten, dass Elektronen auch hier einen wichtigen Beitrag liefern. Die Ergebisse zeigen überdies eine mittlere Temperaturerhöhung um mehr als 10 K in weiten Teilen der Thermosphäre, welche sich auf den Einfall von Partikeln zurückführen lässt. Diese wird besonders durch verstärktes chemisches Heizen und Heizen durch dissipative Wechselwirkungen zwischen Neutralgas und Plasma hervorgerufen. Durch die Wirkung dieser dissipativen Effekte auf die atmosphärische Dynamik findet eine partikelbedingte Abkühlung um mehr als 5 K in der unteren Thermosphäre im Sommer statt.
Um die mittel- und langfristigen Auswirkungen starker solarer Partikelstürme auf die Erdatmosphäre zu untersuchen, muss neben dem Einfall hochenergetischer solarer Protonen auch der Einfall weniger energiereicher Elektronen berücksichtigt werden, welche im Wesentlichen magnetosphärischen Ursprungs sind.

Contents

Chapter 1

Introduction

The assessment of natural and anthropogenic sources of the observed climate trend is a substantial scientific issue since a couple of decades. At this, the response of the Earth's atmosphere to variable solar input is a considerable uncertainty. It involves the 11-year sunspot cycle, the 27-day solar rotational cycle, and precipitation of energetic charged particles. The investigation of the atmospheric response to the latter is the purpose of this work. Even though, this work is not focussed on climate effects, the results can be used in future climate prediction studies. Before the influence of precipitating energetic charged particles on the atmosphere is discussed in detail a short overview about the nature of the involved particles and the phenomenon of particle precipitation is given in the following.

1.1 Energetic charged particles within the Sun Earth system

Energetic charged particles enter the Earth's atmosphere from the interplanetary space and from the Earth's magnetosphere. The particle spectrum primarily comprises electrons, protons, and α-particles exhibiting typical energies from a few tens of eV to several GeV but also heavier ionized particles of H, He, up to Zn can be found (*Breneman and Stone*, 1985). Although these particles exhibit high energies, in comparison with the total energy input by solar electromagnetic radiation energetic charged particles constitute a minor source of energy in the atmosphere. However, within the high latitude upper and middle atmosphere these particles can substantially contribute to the energy budget, becoming the dominant energy source in the absence of insolation. Energetic charged particles are originally generated by the Sun, planetary ionospheres, or other sources in the interstellar space. However, with regard to the location of particle acceleration these particles are commonly referred to as solar energetic particles (SEPs) and magnetospheric energetic particles (MEPs). A detailed definition of these particle populations is given in the following.

1.1.1 Definition of SEPs and MEPs

Streams of charged matter originating from the Sun propagate along the interplanetary magnetic field (IMF) lines (*Kallenrode*, 2004). These streams of plasma, commonly referred to as solar winds, usually consist of solar particles of relatively low energies. Their influence on the atmosphere is rather secondary and will be discussed in detail in conjunction with MEPs. Occasionally, large amounts of high-energy particles are ejected by the Sun. Such SEP events are strongly coupled with the occurrence of solar flares and coronal mass ejections (CMEs). Some CMEs cause migrating shock waves which further accelerate energetic particles while traveling through the interplanetary space. If the location of particle acceleration is connected by the lines of the interplanetary magnetic field (IMF) with the Earth's magnetosphere, SEPs can enter the atmosphere over the polar regions where the magnetic field lines are open. When SEPs penetrate into the atmosphere their energy is gradually delivered to the atmosphere in order to ionize and heat the ambient air. While the duration of a SEP event at the Sun typically is of a few minutes up to one hour the corresponding particles reach the Earth's orbit a few hours up to one or two days past their ejection. Since interactions between these particles and the atmosphere lead to increased ionization in the polar region and consequently cause radio wave absorption such events are sometimes termed as polar cap absorption (PCA) events. Under the assumption that protons are the dominating particle species of SEP events they are often named solar proton events (SPEs). However, also electron rich SEP events occur which may affect the Earth's atmosphere and therefore, in this work the term SEP event corresponds to the complete particle spectrum. Besides solar energetic particles the interplanetary space is populated by energetic particles of interstellar origin. Such corpuscles may be accelerated by shock waves and attached to streams of solar matter (*Kallenrode*, 2004).

In contrast to SEPs which basically originate from the Sun, MEPs not necessarily are generated in the Earth's magnetosphere. Their name is owing to the location of acceleration before they penetrate into the Earths atmosphere. Actually, a substantial amount of MEPs is formed by solar wind plasma and hence of solar origin. A further portion consists of ionospheric plasma. In addition, a couple of processes take place in the magnetosphere creating new plasma. In the magnetosphere charged particles are stably trapped within radiation belts and the plasma sheet of the magneto tail. The mechanisms of particle generation and trapping within the magnetosphere are quite complex and a discussion is beyond the scope of this work. In this regard it is referred to the literature (see e.g. *Kallenrode*, 2004; *Li and Temerin*, 2001; *Hultqvist et al.*, 1999).

During magnetic storms which are caused by fast solar wind streams or interplanetary shock waves, disturbances of the Earth's magnetic field lead to acceleration of charged particles from the radiation belts and the plasma sheet into the atmosphere of subauroral and auroral regions respectively.

In the following, SEPs and MEPs which precipitate into the Earth's atmosphere

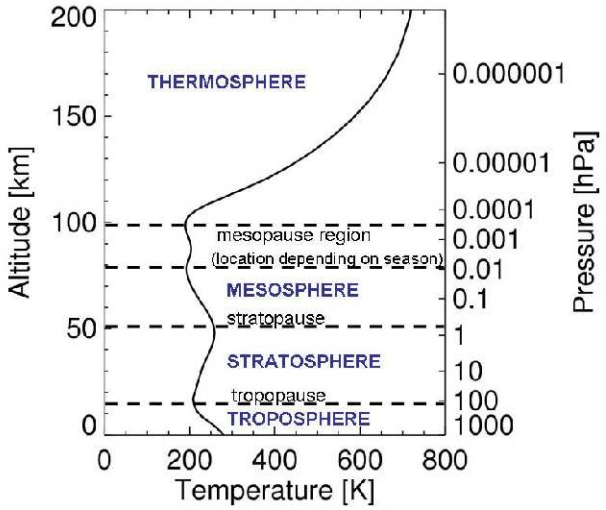

Figure 1.1— Globally averaged atmospheric temperature structure and corresponding atmospheric layers. The temperature profile is taken from a GCM simulation and represents the mean over period December 2003-February 2004.

are collectively referred to as precipitating energetic particles (PEPs).

1.1.2 PEPs in the atmosphere

While the region of precipitation is determined by PEP's origin the penetration depth is primarily controlled by the energy of PEPs. The penetration depth and the altitude regions where particles act on the atmosphere are in the following usually described by different atmospheric layers. As indicated in Figure 1.1, which shows the globally averaged altitude profile of the temperature and different layers, these layers can be described by characteristic features of the temperature profile. It must be noted, that the presented temperature profile is taken from calculations with the general circulation model (GCM). The lowermost 10-15 km, called troposphere, are characterized by a continuous temperature decrease in upward direction. The upper boundary of the troposphere is the tropopause where a local temperature minimum can be identified. Above the tropopause the temperature increases with increasing altitude reaching a local maximum at an altitude of about 50 km. That temperature maximum corresponds with the stratopause which forms the upper boundary of the stratosphere. The lowest temperatures anywhere in the atmosphere can be found at the mesopause, the upper boundary of the mesosphere. The corresponding altitude varies seasonally between about 80 and 100 km. The stratosphere and the mesosphere form the middle atmosphere. Above the absolute temperature minimum strong temperature increases can be found in the thermosphere, the lowermost part of the upper atmosphere.

Typically, auroral PEPs exhibit energies of 1-10 keV resulting in a precipitation into the lower thermosphere within a narrow band between 70° and 75° geomagnetic latitude (*Thorne*, 1980). Subauroral particles, mainly radiation belt electrons with energies of 10 keV up to several MeV, are sufficiently energetic to reach the mesosphere equatorward of 70° geomagnetic latitude. Occasionally, PEPs of solar origin have extremely high energies allowing them to enter the stratosphere. When PEPs traverse the atmosphere collisions between PEPs and atoms or molecules lead to ionization, dissociation, and excitation of these atmospheric components. Thereby a substantial amount of the initial energy is carried to secondary particles causing further ionizations, dissociations, and excitations (*Thorne*, 1980). In addition, the energy of PEPs can be converted into Bremsstrahlung (*Chapman and Little*, 1957), high-energy electromagnetic radiation which can cover long distances and penetrate into the atmosphere much deeper than the initial particle could.
The direct impact of primary and secondary particles on atmospheric gases initializes a series of subsequent chemical reactions consequently leading to substantially altered abundances of minor compounds. Additionally, numerous direct and indirect effects influence atmospheric dynamics and the energy budget. The underlying mechanisms interact with each other strongly coupled to the spatially and temporally highly variable appearance of PEPs, making the investigation of the influence of PEPs to a challenge since a couple of decades. Based on rather incidental observations and measurements which suggest the existence of PEPs and their influence on the atmosphere, concepts of the involved mechanisms have been developed. Later systematic measurements and complex model studies allowed a verification of these concepts. Chapter 2 will give an overview of the historical development of research concerning PEP effects on the atmosphere.

1.2 Motivation

Already early observations have revealed that the incidence of energetic charged particles can significantly influence the chemical composition of the atmosphere (e.g. *Weeks et al.*, 1972; *McPeters*, 1986) and consequences for the energy budget and dynamics seemed likely. In order to identify the responsible mechanisms a series of model studies have been performed. A large part of these model studies considered the influence of SEP events on the middle atmosphere. As a main result they showed SEP-induced increases of the chemically very active species of the NO_x (N, NO, NO_2) and HO_x (H, OH, HO_2) family and a resulting ozone depletion (e.g. *Jackman et al.*, 2005; *Verronen et al.*, 2005). Besides the influence of SEPs on the atmospheric chemical composition also changes of the energy budget and dynamics due to SEP impact have been studied (e.g. *Krivolutsky et al.*, 2006; *Jackman et al.*, 2007). These model studies usually consider precipitation of high-energy protons into the middle atmosphere, only. That excludes consideration of a series of important processes which are associated with SEP events. Not included are the effects of incident α-particles and high-energy electrons of solar

origin, or precipitation of MEPs. The latter can be induced by SEP precipitation. These magnetospheric particles can exhibit sufficiently high energies so that they penetrate into the middle atmosphere where they superpose SEP effects. In a model study by *Wissing et al.* (2010) in addition to solar protons also solar electrons and magnetospheric particles are considered, but the examinations are constrained on altitudes below the thermosphere. Therefore, not considered are the effects of the main part of MEPs which directly act within the thermosphere and, as suggested by early theories (e.g. *Solomon et al.*, 1982) and corroborated by more recent observations (e.g. *Randall et al.*, 2006, 2009), subsequently can indirectly affect lower atmospheric layers.
Besides model studies which examine the effects of SEP events also model simulations have been performed which focussed on the influence of low-energy magnetospheric particles on the chemical composition, energy balance, and dynamics of the thermosphere (e.g. *Siskind et al.*, 1989a,b; *Dobbin et al.*, 2006). These studies neglect the incidence of energy-rich particles into altitudes below the thermosphere. Thereby potential PEP-induced effects remain unconsidered, which appear in the upper atmosphere as a consequence of interactions with lower atmospheric layers.
Since energy balance, dynamics, and chemical composition react on diverse processes (e.g. *Roble*, 1995; *Mlynczak*, 2000) which in turn undergo complex interactions, it can be guessed that model simulation which only consider a relatively small part of the spectrum of PEP-induced processes cannot reproduce the complex interactions. This is an important reason that the mechanisms of the response of energy budget and dynamics to PEP impact are poorly understood until today.

The goal of this work is to improve our knowledge of the influence of PEPs on the Earths atmosphere. In order to reach this goal a model study is accomplished which simulates the effects of particle precipitation during the "Halloween" particle storm, one of the largest particle precipitation events ever detected in the Earth's atmosphere, and subsequent particle precipitation during the following six months. The study uses a 3-D general circulation and chemistry model which covers an altitude range from the surface up to the thermosphere. The model uses ionization rates of solar and magnetospheric protons, electrons, and α-particles. That gives the possibility, for the first time, to investigate simultaneously, and assess the relative importance of, the effects of both solar and magnetospheric particles taking into account interactions between the effects of both particle classes. The model study is accomplished to clarify the following question:
• What is the influence of an extreme solar particle precipitation event and subsequent solar and magnetospheric particle precipitation on NO_x, HO_x, ozone, and temperature?
Along with the clarification of the general question, this work is concerned with the following aspects:
• What are the individual contributions of precipitating electrons, protons, and α-particles? Such a consideration can help to assess potential errors in conventional

model simulations excluding precipitating electrons or α-particles.
• Which role plays NO_x production by precipitating magnetospheric particles, in particular electrons, and downward transport for the NO_x concentration in the middle atmosphere?
• What are the responsible mechanisms for PEP-induced temperature changes?

1.3 Outline of the Thesis

The following chapter gives an overview of previous work concerning PEP effects on the atmosphere. After that, a theoretical view on middle and upper atmospheric processes which are included in the model is given in chapter 3. Chapter 4 presents PEP-induced ionization rates which are of particular importance for the model simulations forming the basis of this work. Chapter 5 compares nitric oxide densities within the thermosphere calculated by HAMMONIA and obtained from an empirical model and discusses potential sources of errors. The investigation of PEP-induced atmospheric changes is presented in chapter 6. Here, at first, the influence of PEPs on chemical key components and temperatures is shown. The contributions of precipitating electrons, α-particles, and protons are examined. In this context the importance of interactions between the thermosphere, mesosphere, and stratosphere are discussed. The results of this work are summarized and conclusion are given in chapter 7. This chapter also discusses future activities.

Chapter 2

Review of Conceptual and Historical Understanding of PEP Effects

In the late 50s and early 60s of the twentieth century rocket and satellite based measurements provided evidence of high-energy charged particles in the Earth's environment. Long time before, several incidental observations and indirect studies suggested the existence of such particles and their interactions with the atmosphere. A couple of these indirectly obtained findings are presented in section 2.1. After that, a review of the historical development of observational and theoretical studies investigating the influence of PEPs on the atmosphere is given. Since initial research of PEP effects concentrated either on SEPs in the middle atmosphere or MEPs in the upper atmosphere the review separately considers the investigation of SEP and MEP effects. In the final part of this review studies are presented which consider couplings between atmospheric layers and the combined effects of SEPs and MEPs.

2.1 Indirect Findings

In the late 1870s the aurora was traced back to PEPs by Henry Becquerel (*Kallenrode*, 2004). He guessed that Sun spots are a source of fast protons which can reach the Earth, where they are guided by the magnetic field lines towards the auroral ovals. Although, later investigations suggest that the relation between Sun spots and aurora is based on more complex mechanisms, Becquerels interpretation is noteworthy, since he ascribed the Sun to emit energetic particles which can affect the Earth's environment. These thoughts were revisited by *Chapman and Ferraro* (1931). They developed the idea that the aurora is caused by magnetic storms which are induced when solar matter hits the Earth. *Forbush* (1946) reported several solar flares associated with extraordinary increases in cosmic ray intensity which were measurable

in high and mid-latitude regions but not at low latitudes. He guessed that energetic charged particles emitted by the Sun are responsible for the observed phenomenon. A few years earlier *Vegard* (1939) detected the Balmer H line in auroral spectra which he interpreted as hydrogen showers of solar origin. In a later theory *Vegard* (1948) recognized that H lines in the auroral spectrum are related to fast protons nearing the Earth. Later studies confirmed the existence of protons during aurora events (e.g. *Eather*, 1967; *Edgar et al.*, 1973), even though it is thought that the aurora is primarily caused by electrons.
The investigation of disturbed radio wave propagation occurring over high geomagnetic latitudes shortly after solar flare observations led to consideration of the influence of PEPs on atomic and molecular processes in the atmosphere. The disturbances were attributed to increased ion concentrations in the ionospheric D-region. *Bailey* (1957) suggested that the additional D-region ions are caused by enhanced input of chemical components with low ionization potential. Due to their low ionization potential these components, such as alkali metal compounds, would be easily ionized by solar ultraviolet radiation leading to enhanced ion concentrations. This theory was substantiated by the fact that the disturbances appear to be much stronger at daytime. However, *Herzberg* (1960) ascribed the increased ion concentration to enhanced NO^+ amount. This results from PEP-induced production of nitric oxide (NO) which is relatively easy to ionize by solar photons. The assumption that PEPs are responsible for the production of nitric oxide is noteworthy since the production of nitric oxides by PEPs plays a key role in later studies considering the influence of PEPs on the atmosphere.

2.2 SEP effects

2.2.1 Chemistry

Probably the first in situ measurements showing the influence of SEPs on the atmosphere were accomplished by two Sidewinder rockets instrumented to measure ozone during the initial and the final phase of a solar proton event on 2 and 4 November 1969 (*Weeks et al.*, 1972). These measurements revealed a substantial ozone decline during the SPE within the northern polar mesosphere. The observed ozone decrease disagreed with the results of photochemical calculations by *Maeda and Aikin* (1968) predicting an increase of ozone in consequence of extraordinary strong particle precipitation in that altitude range. *Weeks et al.* (1972) guessed that the observed ozone decrease was caused by PEP-induced NO. This hypothesis was contradicted by the results of a theoretical study by *Swider and Keneshea* (1973) suggesting that the ozone depletion in the mesosphere observed during the SPE in November 1969 was basically caused by the influence of PEP-induced odd hydrogen (HO_x: H, OH, HO_2). During the initial phase of research on atmospheric response to energetic particle precipitation it was already assumed that PEPs are responsible for odd nitrogen (NO_x: N, NO, NO_2) production and a subsequent ozone destruction. In a fundamental theoretical work *Crutzen et al.* (1975) formulated

the chemical relationship explaining the importance of SPEs for the production of NO and the resulting destruction of ozone in the stratosphere. They guessed that initially dissociation, ionization, and dissociating ionization of molecular nitrogen, primarily by secondary electrons, form nitrogen ions and un-ionized atomic nitrogen which in turn can create NO through a couple of reactions. The importance of NO_x for the ozone budget, recognized by *Crutzen* (1970), results from the fact that the ozone destruction by NO takes place within a catalytic cycle which regenerates NO continuously:

$$NO + O_3 \rightarrow NO_2 + O_2 \tag{2.1}$$

$$NO_2 + O \rightarrow NO + O_2. \tag{2.2}$$

Results of a model study by *Heath et al.* (1977) suggested that NO_x induced by solar protons caused a substantial ozone depletion which was observed in the stratosphere after a severe solar proton event on 4 August 1972. The above mentioned theoretical studies dealing with the influence of solar proton events on the chemical composition of the stratosphere and mesosphere, already used ionization rates which were derived from satellite based particle flux measurements in order to prescribe the energy input into the atmosphere due to SEPs. Under the assumption that the influence of precipitating electrons, α-particles, and heavier ions would be negligible, only solar protons were considered. *Rusch et al.* (1981) and *Solomon et al.* (1981) give a detailed description of the relationship between PEP controlled ionization processes and the production of NO_x and HO_x in the middle atmosphere. They provided production rates for NO_x and HO_x depending on PEP-induced ion pair production rates.
Although, theoretical considerations by *Herzberg* (1960) and *Crutzen et al.* (1975) suggest that NO_x might be produced in consequence of solar proton events, an increase of NO was for the first time measured by satellite during a solar proton event in July 1982 (*McPeters*, 1986). In situ measurements of such a NO increase were for the first time performed by a rocket campaign over the Indian Ocean during October 1989 when a series of extraordinarily strong solar proton events happened (*Zadorozhny et al.*, 1992, 1994).
Satellite measurements during and past the October 1989 solar proton events showed substantially more ozone depletion in the winter than in the summer hemisphere (*Jackman et al.*, 1993). Using 2-D and 3-D simulations *Jackman et al.* (1993) studied the causes of the inter-hemispheric differences in the middle atmosphere after strong solar proton events of October 1989. While the 2-D model predicts insignificant inter-hemispheric differences, 3-D model calculations show, in consistence with observations, significantly stronger ozone depletion in the winter than in the summer hemisphere. It was suggested that the observed differences were caused by different dynamical conditions. A pronounced polar vortex, as usually found in the winter hemisphere, inhibits mixing of air from polar latitudes which is perturbed by PEP influence with unperturbed air from middle latitudes, while in the summer hemisphere mixing of perturbed air from the polar region with unperturbed lower latitude air weakens the effect of ozone depletion induced by a solar proton event.

The effects of a strong solar proton event on NO, NO_2, and O_3 were, for the first time, simultaneously observed by satellite for the severe solar proton event which occurred on 14-16 July 2000. These measurements confirmed previous findings of the dramatic influence of strong solar proton events on ozone in the middle atmosphere (*Jackman et al.*, 2000).
In October and November 2003 several solar storms caused a series of intense SEP events. Owing to the time range of their occurrence around the 31 October these events are often referred to as Halloween storm events. The influence of the Halloween storm events on the atmosphere have been studied as much as no other SEP event before. That notable interest is on the one hand due to the extreme intensity of these events and the strong impact on the Earth's atmosphere and on the other hand to a couple of new instruments and methods which were for the first time available to measure such atmospheric consequences. Instruments like MIPAS (Michelson Interferometer for Passive Atmospheric Sounding) and GOMOS (Global Ozone Monitoring by Occultation of Stars) on board of the Environmental Satellite (ENVISAT) of the European Space Agency observed for the first time the effects of a large SEP event on ozone, NO, NO_2, and a series of additional chemical components simultaneously over the southern and northern polar regions. GOMOS supplied the first satellite observations of a NO_2 increase and an ozone decrease in the polar region of the winter hemisphere after a SEP event (*Seppälä et al.*, 2004). MIPAS measurements revealed that the NO_x increase and ozone decrease after the Halloween storm events were weaker and of shorter duration in the summer than in the winter polar region (*López-Puertas et al.*, 2005).
The causes of inter-hemispheric differences of ozone depletion induced by solar proton events in the middle atmosphere were studied by *Rohen et al.* (2005) using a combination of ozone measurements by SCIAMACHY (Scanning Imaging Absorption Spectrometer for Atmospheric Chartography) and simulations with a 2-D chemistry and transport model. They pointed out that due to a smaller solar zenith angle (SZA) and subsequent stronger photolysis of H_2O in the SH polar region the effect of solar proton event produced HO_x is not as strong as in the NH polar region. Since in the NH polar region solar illumination is weak or absolutely absent NO_x is almost protected against photochemical destruction. This also strengthens the ozone depletion in the NH induced by a solar proton event. Additionally, in absence of O_2 photolysis in the NH polar region the ozone recovery is rather slow. It is interesting that *Jackman et al.* (1993) and *Rohen et al.* (2005) found completely different mechanisms which should be responsible for the inter-hemispheric differences in ozone depletion induced by solar proton events. However, it can be guessed that ozone depletion is a result of the combination of both effects.
A couple of SZA dependent mechanisms which cause inter-hemispheric differences of the ozone response to the solar proton event also control the daily variations of the ozone response as indicated by a combination of GOMOS measurements and model simulations (*Verronen et al.*, 2005).
A 3-D model study by *Jackman et al.* (2009) addressed the long-term effects of solar proton events over the time period of 1963-2004. They showed strong statistically

significant NO_y (N, NO, NO_2, NO_3, N_2O_5, HNO_3, HO_2NO_2, HONO, $ClONO_2$, $ClNO_2$, $BrONO_2$) enhancements caused by very large solar proton events in the mesosphere and stratosphere in both hemispheres. Only modest statistically significant signals in ozone are computed for the same events. An analysis of the ozone content indicates that even very large solar proton events do not lead to any statistically significant change in annually averaged total ozone.

2.2.2 Temperature and Dynamics

After fundamental investigations had revealed the prominent influence of solar proton events on chemistry, a couple of studies considered solar proton event effects on temperature and dynamics. Since it was recognized that ozone plays a key role for absorption of ultraviolet solar radiation in the atmosphere (*Hartley*, 1880; *Chappuis*, 1882; *Huggins and Huggins*, 1890) and in consequence ozone controls the temperature distribution, particularly in the stratosphere, the influence of ozone depletion due to solar proton events on temperature has been studied. Model simulations by *Reagan et al.* (1981) and *Reid et al.* (1991) indicated a substantial temperature decrease in the sunlit upper stratosphere due to a massive ozone depletion which was caused by strong solar proton events in August 1972 and October 1989. Rocket-based measurements during the solar proton events in October 1989 confirmed the temperature decrease in the stratosphere (*Zadorozhny et al.*, 1994). Model simulations by *Krivolutsky et al.* (2006) indicate a substantial temperature decrease in the sunlit stratopause region in consequence of substantial ozone depletion due to the solar proton event of July 2000. They also showed a strong temperature increase in the mesosphere, which was attributed to dynamical effects. Qualitatively similar results were provided by further studies which considered temperature effects of the Halloween storm events (*Jackman et al.*, 2007) and a solar proton event in January 2005 (*Becker and von Savigny*, 2010). The temperature increase in the upper summer mesosphere was traced back to a complex interaction between several of dynamical processes, which are initialized by the temperature decrease in the stratopause region. Using a general circulation model, *Jackman et al.* (2009) studied long-term effects of solar proton events on chemical composition and temperature. Although very large solar proton events occurred during the time period, especially from 2000 to 2004, and significant ozone changes have been found in annual averages, no corresponding significant polar temperature variations could be identified. In the above mentioned model studies which investigate the atmospheric consequences of solar proton events only precipitation of energetic solar protons into the middle atmosphere is considered.

2.3 MEP effects

Simultaneously to the investigation of SEP effects, separate studies considered precipitating MEPs. Early model studies showed a variability of ion and neutral

chemistry due to the occurrence of MEPs (e.g. *Jones and Rees*, 1973; *Rees*, 1975; *Roble and Rees*, 1977). Similar to the NO_x production in the middle atmosphere which is caused by SEPs, also a substantial increase of NO_x in the thermosphere was predicted as consequence of MEP precipitation and associated changes of ion chemistry. This was confirmed by satellite observations in the upper mesosphere and lower thermosphere which revealed substantially higher NO_x concentrations in polar latitudes than in middle latitudes, which were attributed to auroral MEP precipitation (*Rusch and Barth*, 1975).

In addition to the influence of precipitating MEPs on atmospheric chemistry also temperature and dynamical effects have been studied focussing principally on the thermosphere. In that context effects of MEP precipitation on interactions between plasma and neutral gas dynamics play an important role. These interactions which are known as ion drag and Joule heating can strongly influence winds and temperature. Using a general circulation model of the thermosphere *Roble and Ridley* (1987) and *Roble et al.* (1987a) showed that ion drag and Joule heating associated with precipitation of auroral MEPs lead to alteration of the horizontal wind pattern and increasing temperatures with the strongest effects in the winter lower thermosphere.

The relationship between chemical processes and temperature changes which are affected by MEP precipitation has been discussed by a couple of authors. *Siskind et al.* (1989a,b) describe an increase of NO in the lower thermosphere in consequence of an auroral particle storm. The NO increase was observed at high latitudes as well as at middle latitudes. Model simulations indicated that at high latitudes the major part of the additional NO is a result of MEPs direct influence on chemistry. In contrast to that the NO enhancements at middle latitudes are ascribed to MEP-induced Joule heating, which causes a warming also at middle latitudes. This warming leads to a modified NO chemistry. Besides the MEP-induced increase of NO a study of *Roble* (1992) also indicated N_2 and O_2 increases and decrease of O as response to auroral activity. Model simulations indicate that such a response is caused by upwelling driven by auroral particle precipitation and Joule heating.

The episode of the Halloween storms was not only characterized by SEP precipitation but also accompanied by strong geomagnetic activity and MEP precipitation. *Dobbin et al.* (2006) studied the development of the thermospheric NO concentration and temperatures during the Halloween storm events. A comparison between measurements and 3-D model results showed the influence of aurorally produced NO and associated 5.3 μm radiative cooling on temperature. This study indicated that variations of the NO density must be taken into account for a realistic prediction of thermospheric temperatures during periods of high geomagnetic activity.

Although *Thorne* (1977) has already noted that during geomagnetically disturbed conditions high-energy electrons from the Earth's radiation belts can penetrate into the mesosphere and stratosphere where they form an important source of ionization, the majority of studies which considered the influence of PEPs on the middle atmosphere have been focussed on solar proton events. Only a few studies examined the effects of MEPs below thermospheric heights. A combination of satellite

based observations of electron fluxes and NO content revealed the importance of precipitating magnetospheric electrons for the NO formation in middle and high latitudes of the mesosphere and lower thermosphere (MLT) (*Callis et al.*, 1996a). Further observational and model studies indicated that stratospheric NO_y and ozone content might be significantly affected by NO which is produced by MEPs and subsequently advected downward from the MLT region (*Callis et al.*, 1996b, 1998). Thus the authors suggested that model simulations which deal with PEP effects on the middle atmosphere should generally take magnetospheric electron precipitation into account.
Based on the findings of *Callis et al.* (1998) 3-D simulations were carried out by *Rozanov et al.* (2005). These simulations indicated that magnetospheric electron precipitation leads to a net cooling within the stratosphere and increased surface air temperatures over wide areas of the northern continental regions.
In contrast to the above mentioned model simulations of SEP effects, model simulations which deal with MEP precipitation use ionization rates derived from electron flux measurements by a polar-orbiting satellite or from parameterizations related to the strength of the geomagnetic activity. While it was early recognized that precipitating MEPs cause substantial NO enhancements in the MLT region, the mechanisms of NO_x downward transport and its importance for the lower mesospheric and stratospheric NO_x and ozone budget are still under debate. The historical development of investigation of this coupling process between the upper and the middle atmosphere is part of the following section 2.4.

2.4 Couplings and interactions

Photochemical simulations involving the meridional circulation provided first evidence of a photochemical coupling between the thermosphere and stratosphere (*Solomon et al.*, 1982). They pointed out that the NO_x-production in the thermosphere significantly exceeds the NO_x-production in the stratosphere. During the polar winter, thermospheric NO_x can experience downward transport enhancing the stratospheric NO_x abundance. Taking into account that in polar winter PEPs are the main source of NO_x in the thermosphere the findings by *Solomon et al.* (1982) were groundbreaking for later studies concerning the coupling of the upper and middle atmosphere involving PEPs.
The idea of NO_x transport from the thermosphere down to the stratosphere inside the polar vortex was revisited by *Callis and Natarajan* (1986) in order to explain the occurrence of the substantial ozone decrease which was observed since the late 1970s during Antarctic spring (*Farman et al.*, 1985) and known as ozone hole. *Callis and Natarajan* (1986) contradicted the theory of *Farman et al.* (1985) that the considerable ozone decrease is caused by enhanced emissions of chlorofluorocarbons of anthropogenic origin and subsequent increase of chlorine species within the

stratosphere. Measurements (e.g. *Noxon*, 1978; *McKenzie and Johnston*, 1984; *Fahey et al.*, 1989) raised doubts about the NO_x transport theory and today it is generally accepted that chlorine plays the major role. NO_x minima were found in both the time and altitude range of the strongest ozone decline. A detailed overview of the research concerning the causes of the ozone hole is given by *Solomon* (1999). Satellite observations revealed a substantial ozone decrease in the southern polar stratosphere in consequence of the pronounced solar proton event of July 2000. The ozone decrease was accompanied by the strongest NO_x increase ever observed by satellite in the SH stratosphere (*Randall et al.*, 2001). *Randall et al.* (2001) interpret the extreme NO_x increase as a consequence of downward transport within the SH polar vortex which carries NO_x induced by a solar proton event from the upper atmosphere into the stratosphere. *Randall et al.* (2005) analyzed remarkable NO_x enhancements which were observed a few months past the Halloween storms, in the advanced NH winter 2003/2004, in the stratosphere. Their analysis suggests that the Halloween storm and subsequent PEP events produced substantial amounts of NO_x in the upper atmosphere. Unusual meteorological conditions led to an unusually strong polar vortex from late January through March 2004 which likely transported NO_x downward into the stratosphere. The downward transport hypothesis was supported by observations of carbon monoxide (CO) which is chemically inactive and therefore used as an indicator of downward transport (*Randall et al.*, 2006). The findings of *Randall et al.* (2001, 2005, 2006) are noteworthy since they show impressively a coupling mechanism of the upper and middle atmosphere involving PEP-induced chemical processes. It was shown that the main portion of descending NO_x in NH winter 2003/2004 was not produced by the Halloween storm SPEs but generated by subsequent auroral activity and corresponding MEP precipitation (*Semeniuk et al.*, 2005; *Clilverd et al.*, 2006).
Strong downward transport of NO_x leading to exceptionally large NO_x amounts within the stratosphere was observed during several of the following NH winters (e.g. *Randall et al.*, 2006, 2009; *Siskind et al.*, 2007). The majority of these winters were characterized by extraordinarily weak PEP activity and polar vortex anomalies indicated by unusual middle atmospheric temperatures. It was deduced that extreme variations of the NO_x content in the NH polar stratosphere are less a result of variable PEP activity but rather caused by anomalous meteorological conditions. Analyses showed changes of the stratospheric NO_x content in SH polar winter, where the polar vortex is more stable than in the NH, are mainly caused by PEP activity (*Randall et al.*, 2007).
In order to assess the long-term influence of NO_x intrusion on stratospheric chemistry *Reddmann et al.* (2010) carried out 3-D model simulations. A time range from July 2002 to March 2004 is considered including the Halloween storm PEP events. Since the model could not reproduce the dynamical conditions which cause strong downward transport events, the corresponding large enhancements of NO_x are prescribed by MIPAS measured NO_x concentrations. The model results show the strongest stratospheric ozone depletions occurring in SH spring 2003 and in NH spring 2004, the periods after pronounced NO_x downward transports into the

stratosphere.
The first model study which considers both solar and magnetospheric precipitating protons and electrons was carried out by *Wissing et al.* (2010). The period of the Halloween storm PEP events was simulated. Model results suggest that ionization by magnetospheric electrons directly produces NO_x above the stratopause and in consequence significantly affect the mesospheric ozone content. It is also shown that magnetospheric electrons cause a significant impact on stratospheric ozone during polar winter. However, these simulations are constrained on altitudes below the thermosphere and cannot reflect effects which are caused by particle precipitation into the upper atmosphere.

Chapter 3

Middle and Upper Atmospheric Processes in HAMMONIA

The influence of PEPs on the atmosphere is studied using simulations with the Hamburg Model of the Neutral and Ionized Atmosphere (HAMMONIA). HAMMONIA is a general circulation and chemistry model which treats chemistry, radiation, and dynamics interactively for an altitude range from the surface up to the thermosphere ($1.7 \cdot 10^{-7}$ hPa). A detailed description of the model is given by *Schmidt et al.* (2006). In order to simulate the effects of particle precipitation it was necessary to implement a couple of parameterizations or to modify the existing ones in HAMMONIA. These model modifications are described in the following. Here, the original version of the model is referred to as HAMMONIA-1, while the modified version is named as HAMMONIA-2. A brief description of the associated atmospheric processes is also given. Finally, the simulation setup is presented.

3.1 Chemistry

As described by *Schmidt et al.* (2006) HAMMONIA-1 uses a condensed version of the MOZART3 chemistry module (*Kinnison et al.*, 2007) with 48 components, 46 photolysis, and 107 bi- and termolecular gas phase reactions. This set of chemical reactions is completely adopted in HAMMONIA-2, whereas the corresponding reaction rate coefficients are updated to values given by *Sander et al.* (2006).
As already mentioned, in this work the influence of PEPs on chemical composition, dynamics, and energetics is studied. It has been recognized that the associated atmospheric changes are mainly initialized by interactions between PEPs and the ionosphere. This means in particular the generation of ions in consequence of collisions between PEPs and neutral atmospheric components.
For an accurate description of the thermospheric chemistry and in order to reflect the PEP-induced changes of the ionospheric composition an ion chemistry module has been implemented into HAMMONIA-2 representing the ion chemistry of the iono-

spheric E- and F-regions. The E-region comprises the lowermost thermosphere up to about 130 km, while the F-region extends over a couple of hundred kilometers above the E-region. The ion chemistry module in HAMMONIA-2 consists of 13 ion-neutral reactions (listed in Table A.15) and 5 ion-electron recombination reactions (listed in Table A.14) involving the six constituents O^+, O_2^+, N^+, N_2^+, NO^+, and electrons. Additionally, HAMMONIA-2 considers 5 ionizing reactions directly involving PEPs. These PEP-induced reactions are listed in Table A.1. Following the formulations of *Roble and Ridley* (1987), ionization of O, O_2, and N_2 is calculated using particle-induced ion pair production rates which are provided by the Atmospheric Ionization Module Osnabrück (AIMOS) (*Wissing and Kallenrode*, 2009). The algorithm of determination of ionization rates is briefly described in section 4.1 and their application in HAMMONIA-2 is discussed in section 4.3. PEP-involving reactions are complemented by a reaction which describes pure dissociation of molecular nitrogen, as also shown in Table A.1. It must be noted, that the explicit consideration of PEPs in chemical reactions is constrained to the thermosphere. In the middle atmosphere where the ion density is significantly smaller than above ion chemistry is dominated by complex processes involving negative and cluster ions. Since the present work is interested in NO_x and HO_x production resulting from the interactions between PEPs and ion chemistry, parameterizations are used which describe the production of atomic nitrogen and HO_x in the middle atmosphere resulting from the interaction of PEPs and complex ion chemistry. These parameterizations are depending on the PEP-induced ionization rates and therefore they are discussed more detailed in conjunction with the ionization rates in section 4.3.

While PEPs are the main source of ions at high latitudes, particularly in the absence of solar irradiance, solar photons corresponding to Lyman-α and shorter wavelengths are the main source of ions in the sunlit atmosphere. Therefore, HAMMONIA-2 considers 6 ionizing reactions involving radiation at wavelengths between Lyman-α and soft X-rays. Additionally, pure dissociation of molecular nitrogen by extreme ultraviolet radiation is considered. Ionization and dissociation of O, O_2, and N_2 by radiation of wavelengths less than 121 nm and by subsequent secondary electrons are calculated using the parameterization of *Solomon and Qian* (2005). Here, the irradiance in bin λ is given by:

$$I_\lambda = I_\lambda^0 \cdot \left[1 + A_\lambda \cdot \left(\frac{F10.7 + F10.7a}{2} - I_{min}\right)\right] \tag{3.1}$$

where $I_{min} = 80 sfu$ ($1 sfu = 10^{-22} W/m^2/Hz$). The parameters I_λ^0 and A_λ are taken from Table A1 in *Solomon and Qian* (2005). The solar activity represented by the solar radio flux at wavelength of 10.7 cm (F10.7) is obtained from the National Geophysical Data Center of the National Oceanic and Atmospheric Administration (NOAA, http://www.ngdc.noaa.gov). $F10.7a$ is the 81 day average of $F10.7$. Due to its relatively low ionization threshold NO is ionized by the intense solar Lyman-α line at 121.6 nm. This important ion source is also considered in HAMMONIA-2, using a cross section of $2{\cdot}10^{-18}$ taken from *Kazil* (2002). Table A.2 summarizes the reactions caused by the impact of solar radiation in spectral range between

Lyman-α and soft X-ray.
In addition to chemical reactions involving ions, electrons, PEPs, and hard solar irradiance the chemistry module has been extended by 13 neutral bi- and termolecular reactions which are assumed to be relevant for NO_x chemistry or heating by release of chemical potential energy. These reactions are included in Tables A.4-A.7.

3.2 Energetics and Dynamics

3.2.1 Heating by exothermic chemical reactions

As mentioned above, energy-rich photons and PEPs can dissociate, excite, or ionize atmospheric gases. Through these processes kinetic energy of photons and PEPs is converted into chemical potential energy of the resulting species. In atmospheric regions with high density these species recombine immediately or they are rapidly quenched. Consequently, the associated release of chemical potential energy causes a warming of the atmosphere close to the point where an individual PEP hits another atmospheric particle. In the upper atmosphere, at low density, the life time of ions, excited species, and dissociation products increases considerably. Hence, these products can travel long distances before they release their chemical potential energy and warm the atmosphere. The so-called chemical heating is the most important heating mechanism in the upper atmosphere. In HAMMONIA-1 chemical heating is calculated for 7 neutral reactions (see Tables A.16). In HAMMONIA-2 they are complemented by 44 additional reactions (see Table A.17) which are primarily related to ion chemistry, the impact of PEPs, and short wave solar radiation.

3.2.2 Direct heating by PEPs and solar extreme ultraviolet radiation

An additional neutral gas heat source is the direct thermalization by collisions with secondary electrons resulting from the impact of PEPs or solar extreme ultraviolet (EUV) radiation comprising wavelenghts between Lyman-α and 0.05 nm. Following *Roble et al.* (1987b), it is assumed in HAMMONIA-2 that 5% of the energy of each absorbed EUV photon is directly converted to heat. Concerning direct thermalization of energy from PEPs, we adopt a similar approach from *Marsh et al.* (2007) which calculates it as the product of the particle induced ionization rate, 35eV ($5.6077 \cdot 10^{-18}$J) per produced ion pair, and a heating efficiency of 5%.

3.2.3 NO cooling

Infrared cooling by NO emissions at 5.3 μm (called NO cooling) is a significant cooling mechanism particularly in the thermosphere (*Kockarts*, 1980). It is not explicitly taken into account in HAMMONIA-1. In HAMMONIA-2 this process is parameterized using an approach of *Kockarts* (1980). This approach considers excitation and deactivation of NO due to collisions with atmospheric constituents and spontaneous emission of photons. As indicated by measurements the dominating collision partner is atomic oxygen. Using thermodynamic considerations the parameterization of *Kockarts* (1980) calculates the NO cooling rate as function of the predicted kinetic temperature and concentrations of nitric oxide and atomic oxygen.

3.2.4 Ion drag and Joule heating

The neutral gas flow is mainly governed by the pressure gradient and the Coriolis force in a wide altitude range. The motion of ionospheric plasma is additionally controlled by magnetic and electric forces. Even though the density of the ionospheric plasma is far less than that of the neutral gas, in the thermosphere dissipative effects act between plasma and neutral gas. They can significantly affect thermospheric winds and temperatures. The corresponding force on atmospheric motions is referred to as ion drag and the resulting temperature effect is known as Joule heating.
In HAMMONIA-1 the effects of ion drag and Joule heating are calculated following an approach of *Hong and Lindzen* (1976). This simple approach calculates the effects of plasma on the neutral gas flow as function of the geopotential height and geomagnetic latitude and therefore it cannot reflect variations associated with geomagnetic activity and particle precipitation. In order to reflect the effects of PEPs on ion drag and Joule heating HAMMONIA-2 uses a parameterization of *Zhu et al.* (2005). This parameterization uses the model-predicted electron and ion concentrations. Besides the electron and ion concentrations, ion drag and Joule heating also depend on the ion drift velocity which is calculated from the so-called $\overrightarrow{E} \times \overrightarrow{B}$ velocity. In HAMMONIA the Earth's magnetic field ($\overrightarrow{B}$) is assumed to be a dipole field centered at the geomagnetic poles. Its strength is $B = 2.82 \cdot 10^{-5}\sqrt{1 + 3sin^2\theta}$ (*Roble and Ridley*, 1987) where θ is the geomagnetic latitude. The shape of the electric field $\overrightarrow{E}$, which is defined by the gradient of the polar cap potential, is calculated using a model of *Heelis et al.* (1982). This model, which is taken from a software package from the "ModelWeb Catalogue and Archive" of the NASA Goddard Space Flight Center (http://modelweb.gsfc.nasa.gov), describes the form of the polar cap potential or the large-scale global convection characteristics of the high latitude ionosphere, respectively. The calculated shape of the polar cap potential is shown in Figure 3.1 for different times. It must be noted that the strength of the polar cap potential is correlated to the geomagnetic activity. As suggested by *Foster*

et al. (1986) the strength of the electric field is determined by the product of 7.8 kV and an empirical derived scale factor based on the K_p-index which is associated with the geomagnetic activity. The relation between K_p-index and scale factor is shown in Table 3.1. In HAMMONIA-2, for K_p-indices between the listed ones the scale factor is derived from linear interpolation. For K_p-index greater than 6- a scale factor of 10 is assumed. The time dependent Kp-index is taken from NOAA (http://ngdc.noaa.gov). The strength of the polar cap potential shown in Figure 3.1 is associated with a scale factor of 1 representing weak geomagnetic activity.

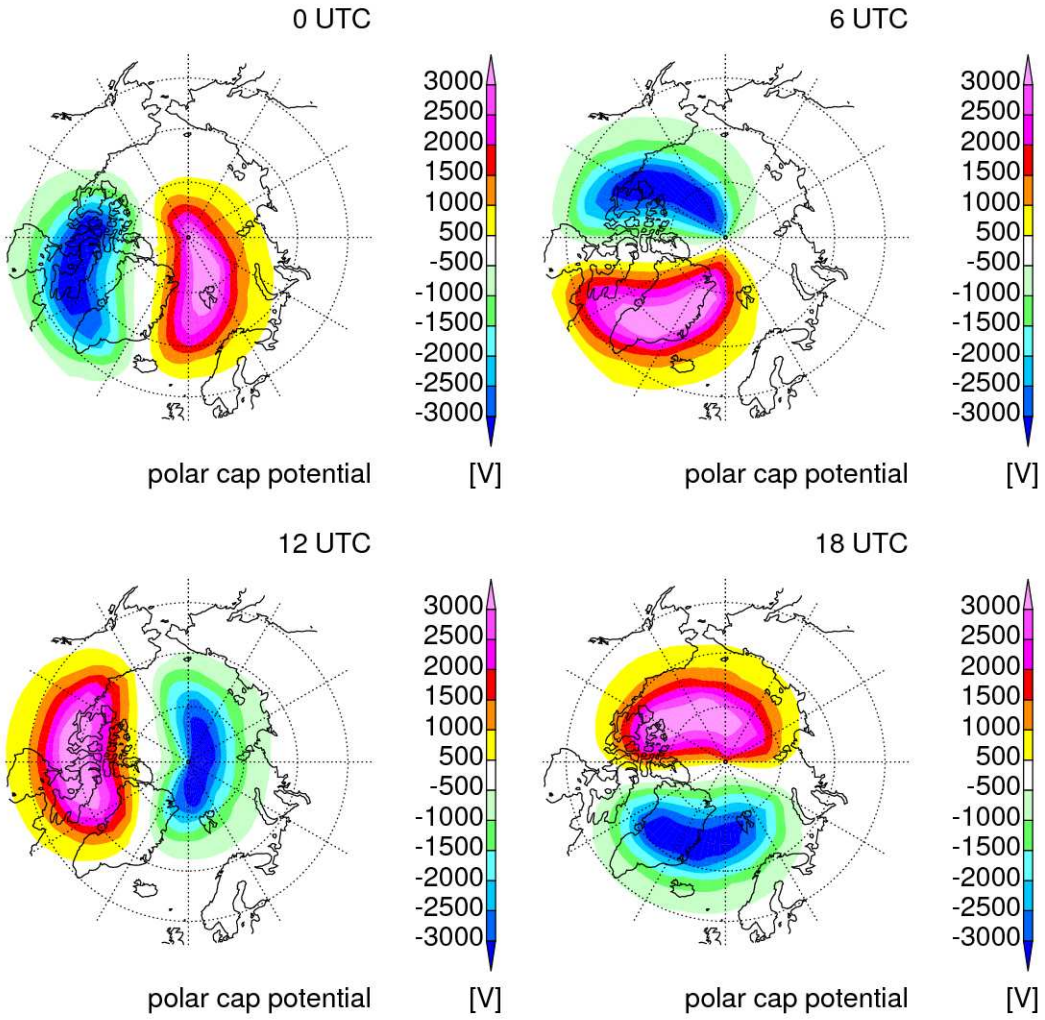

Figure 3.1— North polar cap potential configuration at 0 UTC (top, left), 6 UTC (top, right), 12 UTC (bottom, left), and 18 UTC (bottom, right) corresponding to a precipitation index of 1.

For the simulations in this work the northern pole of the geomagnetic field is assumed to be located at 79.7°N/71.7°W. This is approximately the position where

Table 3.1— Relation between K_p-index and scale factor as given by *Foster et al.* (1986).

K_p-index	1-	1	1+	2-	2+	3-	3+	4	5-	6-
Scale factor	1	2	3	4	5	6	7	8	9	10

the geomagnetic pole was located in late 2003 and early 2004. Additionally, the parameterization of *Zhu et al.* (2005) requires the calculated Pedersen and Hall conductivities. These conductivities are computed using formulations of *Kertz* (1971) depending on the modeled densities of ions and electrons and their gyro and collision frequencies.
In contrast to the parameterization of *Hong and Lindzen* (1976), which is used in HAMMONIA-1 in order to simulate the effects of ion drag and Joule heating, the parameterization of *Zhu et al.* (2005) in HAMMONIA-2 allows to reflect some aspects of the response of ion drag and Joule heating to variable geomagnetic activity. Moreover, it allows a more realistic representation of the spatial pattern of ion drag and Joule heating, even though, the applicability of the approach to magnetospheric physics is limited by the exclusion of large magnitude small-scale features of plasma flows as mentioned by *Heelis et al.* (1982). A further limitation of the calculation algorithm in HAMMONIA-2 is caused by the simple assumption of a fixed Earths magnetic field. As a consequence, changes of the terrestrial magnetic field due to variations in particle precipitation cannot be reflected in HAMMONIA-2.

3.3 Experiment configurations

In order to study the effects of the complete particle spectrum and to assess the contribution of different particle classes four experiments have been performed. The first experiment considers the complete spectrum of precipitating energetic charged particles comprising protons, electrons, and α-particles. In the following, it is named as experiment PEA. Two further experiments, named as PE and PA, consider protons and electrons or protons and α-particles, respectively. The experiment composition is completed by a reference experiment excluding particle forcing. In the following, it is named as experiment REF. An overview about the experiments is given in Table 3.2.
The corresponding model simulations cover a time range from March 2003 to April 2004. For the first five months a single simulation has been performed for each experiment. The modeled atmospheric state of 1st of August 2003 00 UTC has been used to start five one-month simulations per experiment. The purpose of these simulations is to generate five slightly different states of the modeled atmosphere. Therefore, each simulation has been carried out with small differences of the gravity wave drag parameterization. The resulting five states are used to initialize five ensemble simulations per experiment starting on 1st of September 2003 00 UTC. The analyses in this work are related to the full ensemble experiments and therefore they

Table 3.2— Experiments and involved precipitating particle classes.

Experiment	involved particle classes
PEA	protons, electrons, α-particles
PE	protons, electrons
PA	protons, α-particles
REF	without precipitating particles

consider a time period after August 2003.
In order to avoid numerical instabilities which can occur when high wind speeds resulting from ion drag violate the Courant Friedrichs Levi criterion (*Courant et al.*, 1967), all experiments have been performed with a numerical time step of 180 seconds. This time resolution is significantly higher than that of 10 minutes as used in HAMMONIA-1 (*Schmidt et al.*, 2006). Simulations have been performed on 67 vertical equidistant log-pressure levels ranging from the surface up to $1.7{\cdot}10^{-7}$ hPa. Tri-angular truncation T31 is used corresponding to a horizontal resolution of about $3.75° \times 3.75°$. Using Newtonian relaxation technique the simulations are nudged to ECMWF-analyzed fields of sea surface temperature, air temperature, vorticity, and divergence up to pressure level of 170 hPa. For all model simulations in this work HAMMONIA-2 is used. In the following that model version is referred to as HAMMONIA.

Chapter 4

Ionization Rates

In HAMMONIA the PEP impact on the atmosphere is represented by ion pair production rates which are calculated by colleagues from the University of Osnabrück using AIMOS (Atmospheric Ionization Module Osnabrück). They are provided as time dependent 3-D data sets for protons, electrons, and α-particles. The algorithms used to determine the ionization rates are briefly presented in the following. A detailed description of the ionization rates and their determination by AIMOS is given by *Wissing and Kallenrode* (2009).

4.1 Calculation

The determination of ionization rates in AIMOS is based on multi-satellite measurements of particle fluxes. The instruments TED (Total Energy Detector) and MEPED (Medium Energy Proton and Electron Detector) on board of the polar orbiting NOAA POES (Polar-orbiting Operational Environmental Satellite) satellites 15 and 16 provide information on the incidence of protons with energies ranging from 154 eV to 6.9 MeV and electrons with energies from 154 eV to 2.5 MeV. Protons of higher energies up to 500 MeV as well as α-particles in an energy range from 4 to 500 MeV are detected by Energetic Particle Sensor (EPS) on board of GOES (Geostationary Operational Environmental Satellite). These measurements provide the possibility to calculate three dimensional ionization rates considering almost the complete particle spectrum. Combination of measurements from both polar orbiting satellites is used to determine a horizontal precipitation pattern. The width of the polar cap over which SEPs enter the atmosphere is derived from the geomagnetic activity and proton observations by POES at the maximum detectable energy (6.9 MeV). For higher energetic SEPs (GOES is able to detect protons of up to 500 MeV) the area of precipitation is extended equatorward. The determination is limited to two hourly temporal resolution due to the orbital time of the POES satellites.
In addition to the horizontal distribution of the particle precipitation also the penetration depth and the location of the energy deposition has to be computed. While α-particles and protons propagate more or less straightforward, electrons undergo multiple scattering, whereby their covered distance in the atmosphere can substan-

tially exceed the penetration depth. This effect is important in the less dense upper atmosphere. Additionally, the location where PEP energy is finally deposited is also dependent on the creation of secondary electrons and Bremsstrahlung. In order to determine the location of deposition of PEP energy, taking into account interactions between PEPs and the atmosphere, AIMOS applies a Monte Carlo simulation. It uses absorber atmospheres which were provided by HAMMONIA for different geographic latitudes, seasons, and solar activity strengths.

4.2 Ionization of different particle species in different regions

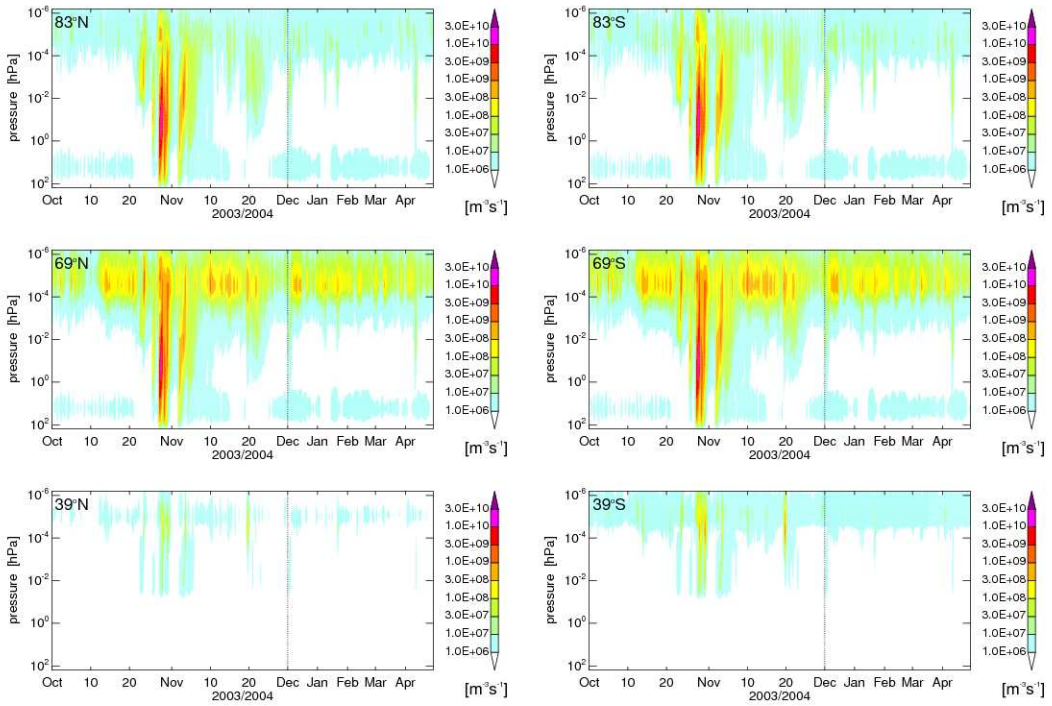

Figure 4.1— Time evolution of ionization rates of precipitating protons at geomagnetic latitudes of about 83°, 69°, and 39° north (left) and south (right). The unit of ionization rate is $m^{-3}s^{-1}$ and the time range is from October 2003 to April 2004. Note the higher resolution of the time axis for October and November.

The time evolution of ionization rates at different geomagnetic latitudes is presented for protons, electrons, and α-particles in Figures 4.1-4.3. Here, the geomagnetic latitudes of 83° represent the polar caps, the regions where SEPs usually penetrate into the atmosphere. At 69° geomagnetic latitude, the edge of the auroral oval, the main precipitation area of MEPs is located. Geomagnetic latitudes of 39° are usually outside of the main particle precipitation regions.

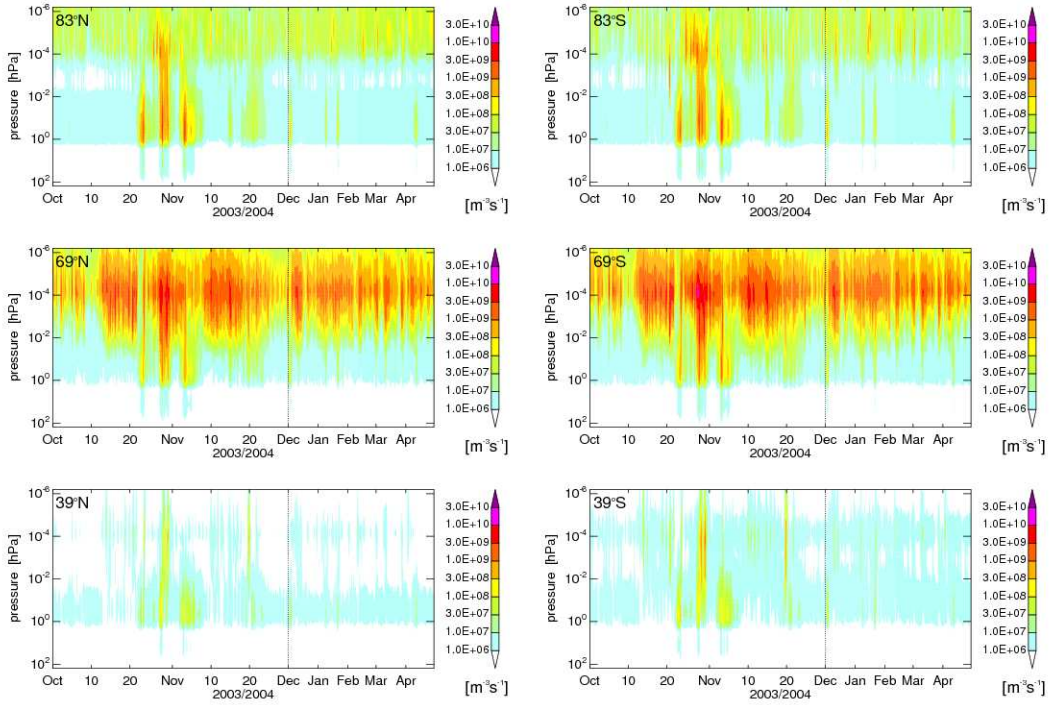

Figure 4.2— Same as Figure 4.1 but for precipitating electrons.

The figures show minor inter-hemispheric differences of ionization rates but regionally they distinguish substantially. In the polar cap regions ionization by protons is usually small. Exceptions occur during the Halloween storm period in October and November 2003 when protons cause intense ionization in the mesosphere and stratosphere. These extreme ionization events also appear at geomagnetic latitudes of 69°, regions usually outside of the main precipitation of SEPs. Nevertheless, it can be assumed that solar protons are responsible for this extraordinary ionization, since during strong SEP events the polar caps temporarily extend equatorward. Moderate ionization by protons occurs in the lower thermosphere of the main MEP precipitation (69°) area over the entire time period. At geomagnetic latitudes of 39° ionization by protons is usually small, with a slight increase during the Halloween storm period. Ionization by electrons exhibits substantial regional variations. Three remarkable ionization events are produced by precipitating electrons from 20 October through 10 November 2003 in the polar cap with their maximum in the lower mesosphere. Both, the temporal and the spatial characteristic of these events show considerable differences to the ionization events which are caused by precipitating protons. Additionally, the mesosphere experiences a series of weaker ionization events caused by electrons. In the lower thermosphere and upper mesosphere of the MEP precipitation area (69°) electrons lead to moderate or strong ionization during the whole time. Except for a few short-term enhancements, ionization by electrons is rather weak below the upper mesosphere. A similar behaviour can be

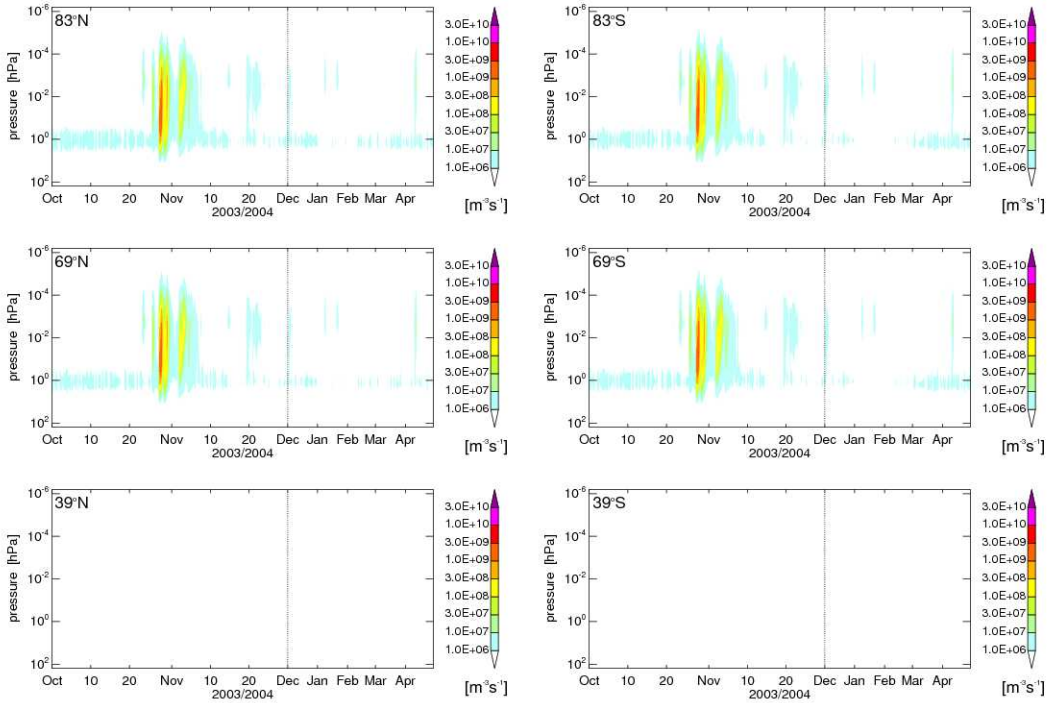

Figure 4.3— Same as Figure 4.1 but for precipitating α-particles.

found, in general, for the entire altitude range at 39°. With the exception of the Halloween storm PEP events ionization by α-particles plays a minor role. Large ionization rates during these events particularly affect the mesosphere of the polar cap regions. Here they show a similar pattern like ionization by protons. High ionization rates at 69° can be explained by an equatorward extension of the polar cap during the strong SEP events leading to precipitation of large amounts of solar α-particles into that area.

4.3 Application of ionization rates within HAMMONIA

While AIMOS calculates time-dependent 3-D sets of ionization rates, HAMMONIA utilizes this data in order to simulate the impact of PEPs on the atmosphere. Depending on the altitude two different approaches are used. Above 0.001 hPa (in the thermosphere) a set of six chemical reactions describes the influence of PEPs on chemistry. These reactions which are listed in Table 4.1 involve PEPs and result in ionization, ionizing dissociation, dissociation, and excitation of O, O_2, and N_2, where the ionization rates serve as reaction rates.
In the middle atmosphere ion chemistry is substantially more complex involving a variety of negative and water cluster ions. Here, HAMMONIA follows param-

eterizations of *Jackman et al.* (2005) describing the net effects of this complex ion chemistry on atomic nitrogen and odd hydrogen. These parameterizations are based on a formulation of *Porter et al.* (1976) which suggests that 0.7 electronically excited (^{2}D) state and 0.55 ground state nitrogen atoms are produced per ion pair, and a formulation of *Solomon et al.* (1981) providing the production rate of H and OH as a function of altitude and ionization rate as shown by Table 4.2.

Table 4.1— Ionization and dissociation reactions caused by PEPs, secondary electrons, and X-ray Bremsstrahlung. Branching ratios for ionizing reactions are taken from *Roble and Ridley* (1987) and the rate for the lowermost reaction is taken from *Verronen* (2006).

reaction	rate
$O_2 + p^* \rightarrow O_2^+ + e^- + p^*$	$Q \cdot [O_2] \ / \ \delta$
$O_2 + p^* \rightarrow O^+ + O + e^- + p^*$	$Q \cdot 0.5 \cdot [O_2] \ / \ \delta$
$O + p^* \rightarrow O^+ + e^- + p^*$	$Q \cdot 0.56 \cdot [O] \ / \ \delta$
$N_2 + p^* \rightarrow N_2^+ + e^- + p^*$	$Q \cdot 0.76 \cdot [N_2] \cdot 0.92 \ / \ \delta$
$N_2 + p^* \rightarrow N^+ + 0.5 \cdot N(^4S) + 0.5 \cdot N(^2D) + e^- + p^*$	$Q \cdot 0.24 \cdot [N_2] \cdot 0.92 \ / \ \delta$
$N_2 + p^* \longrightarrow 0.8 \cdot N(^4S) + 1.2 \cdot N(^2D) + p^*$	$Q \cdot 0.8$
δ=0.92 $\cdot$ [N_2] + 1.5 $\cdot$ [O_2] + 0.56 $\cdot$ [O]	
$p^* \equiv$ primary or secondary particle, Q $\equiv$ total ionization rate, [X] $\equiv$ number density of species X	

Table 4.2— HO_x production per ion pair as function of altitude for Baseline Ionization Rates (BIR). Values are taken from *Jackman et al.* (2005).

	HO_x production per ion pair		
altitude km	BIR $10^2 cm^{-3} s^{-1}$	BIR $10^3 cm^{-3} s^{-1}$	BIR $10^4 cm^{-3} s^{-1}$
40	2.00	2.00	1.99
45	2.00	1.99	1.99
50	1.99	1.99	1.98
55	1.99	1.98	1.97
60	1.98	1.97	1.94
65	1.98	1.94	1.87
70	1.94	1.87	1.77
75	1.84	1.73	1.60
80	1.40	1.20	0.95
85	0.15	0.10	0.00
90	0.00	0.00	0.00

Table 4.3— Locations of ISR instruments. Values are taken from *Wissing et al.* (2010).

station	latitude	longitude
Tromsø	69°35'11"N	19°13'38"E
Svalbard	78°09'11"N	16°01'44"E
Sondrestrom	66°59'12"N	309°03'02"E
Millstone Hill	42°37'10"N	288°30'30"E

4.4 Discussion

In this section uncertainties of the determination of ionization rates and consequences for the ion chemistry are discussed. This is of particular importance as it can help to assess potential error sources for the results of this work.
A direct comparison of modeled ionization rates and measurements is not possible as it would require continuous in-situ measurements of the ionization rates at various locations and altitudes. Alternatively, modeled electron densities can be compared with observations. The electron density is a characteristic physical quantity of ion chemistry and directly coupled to the ionization rates which are processed in HAMMONIA. In contrast to the ionization rates electron densities are continuously measurable, e.g. by incoherent scatter radar (ISR) instruments at different locations and over a wide altitude range. Such a comparison of electron densities which are calculated by the AIMOS/HAMMONIA model chain with ISR measurements has been carried out in collaboration with the AIMOS working group and scientists involved in generation of the observational data. That work is presented in *Wissing et al.* (2011). Based on that study, in the following obvious discrepancies between simulation and observations, and responsible error sources are discussed.
The comparison uses observations from the European Incoherent Scatter (EISCAT) radar instruments located in Tromsø and Svalbard, and from additional ISR instruments in Sondrestrom and Millstone Hill. As can be seen in Table 4.3 all of these instruments are positioned at NH middle and high latitudes. While the measurements at Tromsø are mostly within the auroral oval the stations Svalbard and Sondrestrom are located within the polar cap. The Millstone Hill instrument is normally situated equatorward of the auroral oval.
It has to be mentioned that a comparison between model and measurements based on identical time resolution is not possible. The reason is that the time resolution of observational data, although it is strongly dependent on the specific ISR instrument, is in general sufficiently high to resolve extreme short-time variations. Such short-time variations of particle activity (time scales lower than one hour) cannot be resolved by the AIMOS/HAMMONIA model chain since the AIMOS resolution is two hours, only. Consequently, the ionization rates are provided as two hourly means and the particle forcing applied in the model is constant over two hours. Therefore, the comparison uses snap-shots of the modeled electron densities at the end of the two hour intervals and a time mean of ISR data with an integration time of one hour ending

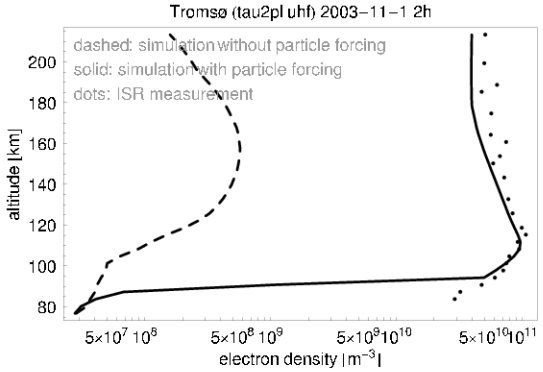

Figure 4.4— A typical auroral night-time comparison of a simulation with and without particle forcing in contrast to the result of the incoherent scatter radar measurements. The illustration is adopted from *Wissing et al.* (2011).

at the time of the snap-shot. Only time intervals are considered with a maximum of 10% gaps and 10% differing viewing direction. For the latter it must be noted that the viewing direction changes continuously in some ISR experiments. All available ISR data (from the Madrigal data base: http://www.eiscat.se:8080/madrigal) for the period of October 2003 to April 2004 are used which satisfy the above-mentioned criteria. Note, that none of the instruments provides continuous data during the entire time period. They provide data for a series of sporadic measurements each typically covering a time period of several minutes, hours, up to days.

Figure 4.4 shows a typical example of high-latitude night-time electron densities which are obtained from model simulations with and without particle forcing compared to the electron density measured by ISR. While the electron density from a simulation without particle forcing, where ions are only produced by electromagnetic radiation, is about two to four orders of magnitude smaller than the measured values, electron densities from simulation with particle forcing and measured values are in the same order of magnitude. Discrepancies at day-time and lower latitudes are in general smaller. The simulated electron density drops strongly close to 90 km. The reason is that HAMMONIA uses full ion chemistry above 90 km, only. Therefore, the comparison is constrained to heights above 95 km.

In the following, the ratio between modeled and observed electron densities is used in order to illustrate the strength of discrepancy between simulation and measurements. First, the dependence on local time of these ratios is considered using all available pairs of values. The left part of Figure 4.5 shows height profiles of the ratio for simulation without particle forcing. A strong dependency on local time is obvious. While at noon simulations show relatively good agreement with observations, at night-time the modeled electron densities are two to three orders of magnitudes smaller than the observed ones. The reason is that at day-time the electron density is mainly controlled by photo-ionization which is included in HAMMONIA. Therefore, in particular night-time comparison provides useful information about potential errors of PEP-induced ionization rates, while at day-time also the

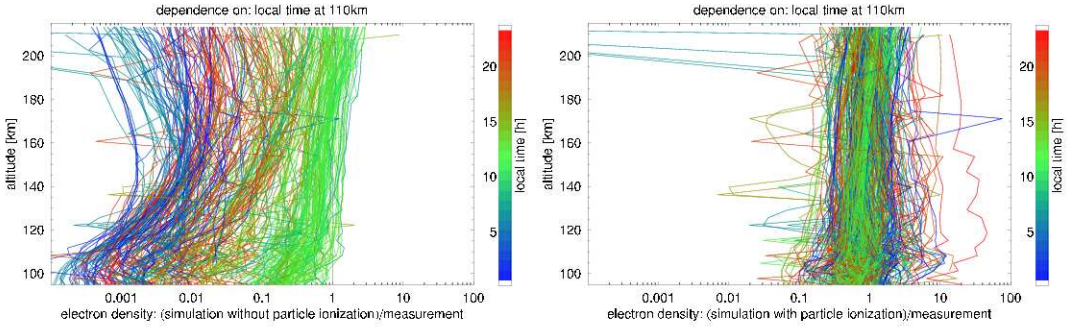

Figure 4.5— Ratios of electron density modeled by HAMMONIA without (left) and with (right) particle forcing and the according electron density derived from ISR measurements. Colors indicate the local time at 110 km according to the viewing direction. Even though the dependency on local time is very obvious, it should be mentioned that the local time is just a rough indicator of daylight since some areas might be affected by polar night. The illustrations are adopted from *Wissing et al.* (2011).

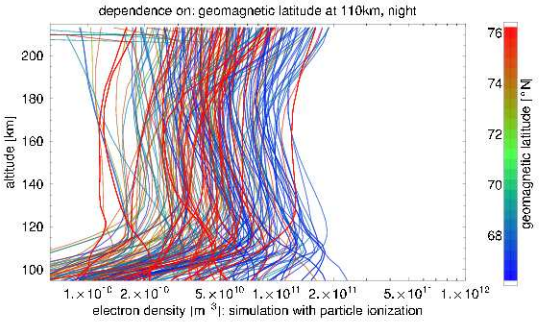

Figure 4.6— Night-time HAMMONIA-modeled electron density including particle forcing depending on altitude. Colors indicate the corresponding geomagnetic position. The auroral oval leads to a maximum of electron density at approximately 66°N. The illustration is adopted from *Wissing et al.* (2011).

influence of potential errors of photo-ionization has to be considered. The right part of Figure 4.5 shows the ratio for the HAMMONIA simulation with particle forcing. Here the values are centered around 1, but a spread of about two orders of magnitude remains. In order to assess these deviations, in the following, dependences on location, geomagnetic activity, and time are studied.

Figure 4.6 shows the dependence of the night-time electron density from simulation with particle forcing (PEA) on altitude and geomagnetic latitude. Since for night-time conditions only PEPs contribute to ionization it can be assumed that electron densities exhibit a similar horizontal distribution as the PEP-induced ionization rates. The curves in Figure 4.6 show that electron densities within the thermosphere tend to have lower values within the polar cap and higher values within the auroral oval ($\lessapprox 70°$).

Figure 4.7 shows for day-time (right) and night-time (left) the ratio between simulated and measured electron density. During night-time the spread is wider than at

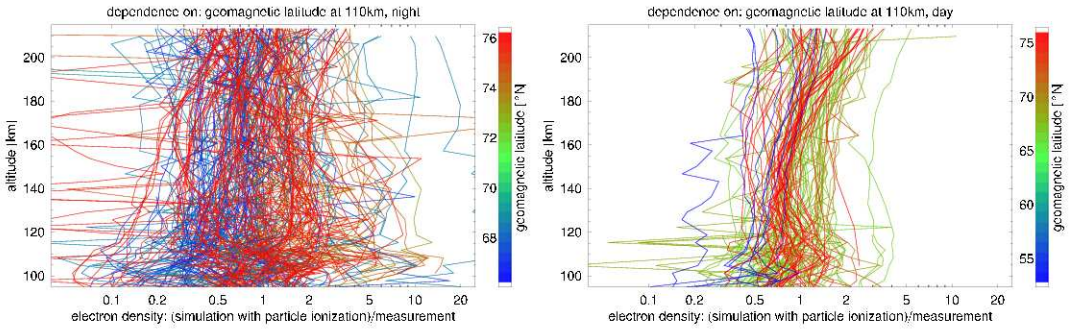

Figure 4.7— Relation of HAMMONIA-modeled and ISR-derived electron density for conditions without (left) and with (right) daylight. The illustrations are adopted from *Wissing et al.* (2011).

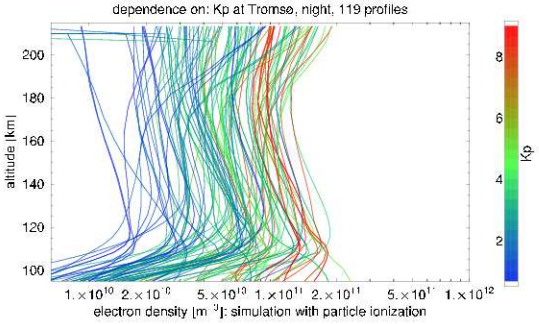

Figure 4.8— Dependence of HAMMONIA-modeled electron density on geomagnetic disturbance (K_p-index, indicated by color) at one particular location: Tromsø. The illustration is adopted from *Wissing et al.* (2011).

day-time. The reason is that at day-time electromagnetic irradiance is normally the main ionization source, which is obviously well reflected by HAMMONIA. It is also revealed that at night-time in the auroral oval the model tends to underestimate the electron density as indicated by the blue color range in Figure 4.7. No systematic bias is indicated for the polar cap. Figure 4.8 shows modeled altitude profiles of the electron density as function of geomagnetic activity during night-time above Tromsø. It is obvious, that the electron density increases with increasing K_p-index which represents the geomagnetic activity. Figure 4.9 shows the ratio of simulated to measured electron density at night-time for Svalbard (left) and Tromsø (right). For the polar cap the ratio is on average close to 1 with values ranging from 0.2 to 10. It seems that for very high K_p-index the modeled electron densities tend to be overestimated. However, the number of profiles is relatively small. For Tromsø , which is located within the auroral oval, at night-time electron densities seem to be underestimated by the model. This is confirmed by Figure 4.7. This underestimation seems to be independent from the K_p-index.

Although the main motivation of the comparison is an evaluation of the PEP-induced ionization rates, it must be discussed if the detected discrepancies might be a result also of uncertain reaction rates of the PEP-initialized ion chemistry, uncertain

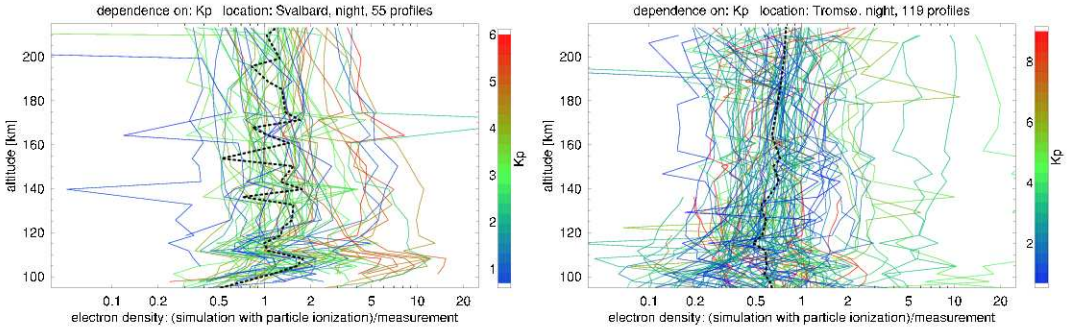

Figure 4.9— Ratio of the HAMMONIA-modeled electron density and the corresponding electron density derived from ISR at two different locations: Svalbard (left) and Tromsø (right). The dashed line indicates the median of all ratios at the specific location. The illustrations are adopted from *Wissing et al.* (2011).

photo-ionization rates, uncertain recombination rates in HAMMONIA, or observational errors.

It can be assumed that wrong reaction rates result in a clear trend of deviation of modeled electron densities independent of location, time, and geomagnetic activity. Indeed, deviations clearly show dependencies on these quantities indicating uncertainties of ionization rates. Uncertainties in the parameterization of solar irradiance on which the photo-ionization rates in HAMMONIA are based on cannot be excluded, but the comparison shows clear night-time discrepancies indicating that the PEP-induced ionization is a main cause of uncertainty.

Discrepancies between modeled electron densities and observations might be caused by the chosen technique of the comparison which uses a different time resolution of the compared values. Further error causes can be guessed in the algorithm of determination of ionization rates in AIMOS. The calculation is based on measurements of polar-orbiting satellites which cannot continuously detect the particle incidence over a certain area. The ionization rates are provided as two hour means but they are derived from observations in much shorter time intervals. Therefore, short-time variations of the particle incidence cannot be resolved by AIMOS.

As already mentioned the calculation of ionization rates also uses a Monte Carlo simulation which considers interactions between particles and the atmosphere. Information about the atmospheric structure is given by altitude profiles of density, temperature, and chemical composition which were calculated by HAMMONIA without considering PEPs. These profiles are taken from simulations of low and high solar activity, respectively, for latitudes which represent the SH and NH auroral oval and polar cap, and for different seasons. AIMOS uses the most appropriate profile with respect to the actual conditions. However, it can be expected that atmospheric conditions during high particle activity are strongly altered and hence probably deviate from the given model atmosphere. This might be an error source particularly during periods with high particle activity. Further error sources concerning the calculation of the PEP-induced ionization rates are discussed in *Wissing and Kallenrode* (2009) und references therein.

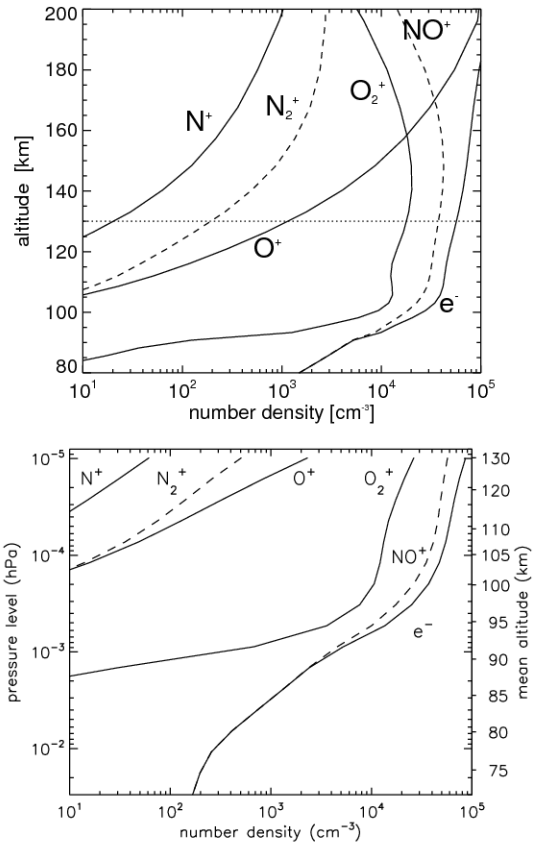

Figure 4.10— Top: HAMMONIA simulated global mean ion and electron density profiles for January 2004. Bottom: WACCM simulated ion densities for July solar minimum conditions. The lower part of this figure is adopted from *Marsh et al.* (2007). Note, that the upper panel considers an altitude range of about 80 to 200 km, while the altitude range in the lower panel is 70 to 130 km.

After evaluation of modeled electron densities the following paragraph considers the corresponding positive ion species. The upper part of Figure 4.10 shows the HAMMONIA simulated global average number densities of five positive ion species and electrons. It can be seen that NO^+ is the dominating positive ion species in the lower thermosphere while above about 160 km O^+ becomes dominant. It is difficult to get observational data appropriate for a comparison with HAMMONIA simulated ion densities. A comparison with ion densities from the WACCM model (*Marsh et al.*, 2007) is also shown in Figure 4.10. It indicates that HAMMONIA simulated ion densities are consistent with earlier modeling work.

Chapter 5

Uncertainties in Representation of Modeled Thermospheric NO_x

The NO_x family consists of the odd nitrogen constituents NO and NO_2. A few authors (e.g. *Marsh et al.*, 2007) also consider atomic nitrogen (N) to be a NO_x component, but in this work the former variant is preferred. Section 2.2 emphasizes the particular importance of NO_x, which is owing to the fact that its components are both chemically and radiatively active and therefore play an important role in determining the composition and structure of the atmosphere. In the thermosphere NO_x production is mainly initialized by the impact of solar EUV radiation and MEPs. Subsequently, downward transport can act as an important source of NO_x in the mesosphere and stratosphere. Since in this work the investigation of thermospheric processes plays a central role the present chapter considers NO_x in the thermosphere. An evaluation of modeled gas concentration is followed by a detailed discussion of possible reasons for errors in the NO_x representations in the model.

5.1 Comparison between HAMMONIA and the Nitric Oxide Empirical Model

In the thermosphere concentrations of NO exceed that of NO_2 and N by several orders of magnitude. Therefore, in these altitudes NO_x is mainly represented by NO which is presented in the following. In order to evaluate the skill of HAMMONIA in simulating NO under the influence of PEPs Figures 5.1 and 5.2 present NO number densities at three selected geomagnetic latitudes of the lower NH and SH thermosphere, respectively. In both figures the left side corresponds to HAMMONIA simulation involving the complete particle spectrum (simulation PEA), while on the right side NO number densities calculated by the nitric oxide empirical model (NOEM) (*Marsh et al.*, 2004) are shown.
Since for the considered altitude and time range observational data of NO are

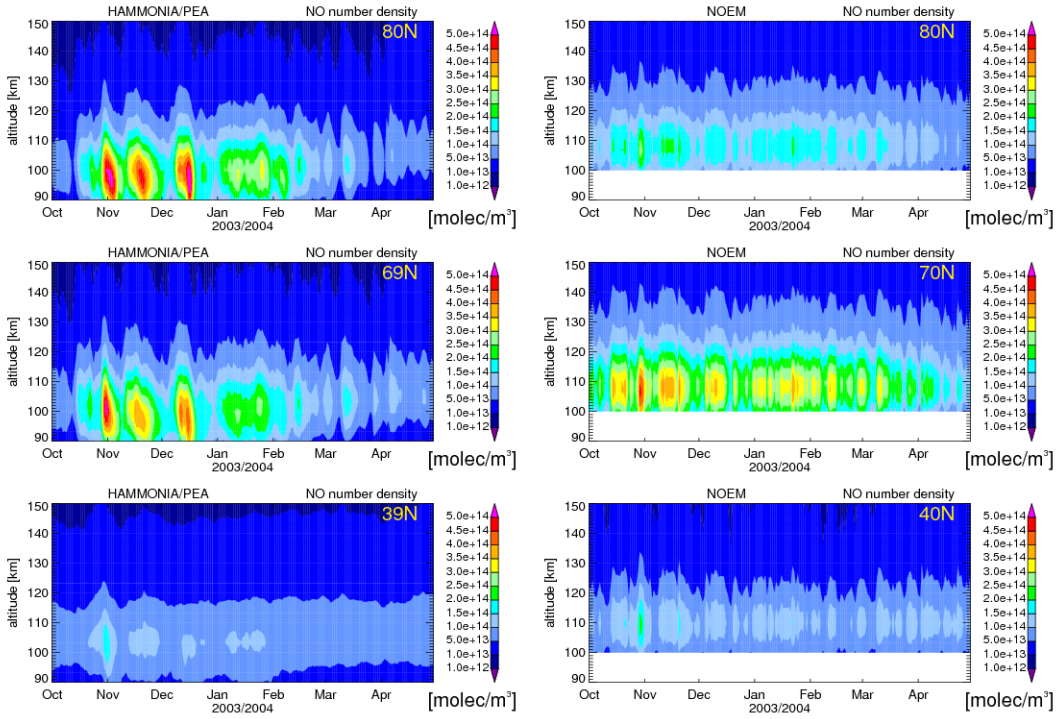

Figure 5.1— Time-height cross sections of NO number density in the lower thermosphere for a period from October 2003 to April 2004. The left side corresponds to HAMMONIA-PEA simulation, while the values on the right are calculated by NOEM. Zonal means at geomagnetic latitudes of about 80° (top), 70° (center), and 40° (bottom) north are shown. No values are provided by NOEM below 100 km.

rare, an empirical model of nitric oxide such as NOEM is a useful tool in order to assess the HAMMONIA simulated NO concentrations. NOEM is based on over 2.5 years of near-continuous NO observations by the Student Nitric Oxide Explorer (SNOE) satellite. It uses the method of empirical orthogonal functions in order to calculate lower thermospheric NO number densities taking into account auroral forcing, changes in solar declination, and solar soft X-ray flux variations. A detailed description of NOEM is given in *Marsh et al.* (2004). In order to create a time series of NOEM-calculated NO number densities which can be compared with HAMMONIA-simulated NO densities, NOEM is driven for the period from October 2003 to April 2004 using appropriate daily K_p and F10.7 values both obtained from NOAA (*www.ngdc.noaa.gov*).

The upper panels of Figures 5.1 and 5.2 show NO number densities at 80° geomagnetic latitude, which is located within the polar cap. As indicated by the ionization rates (see Figures 4.1, 4.2, and 4.3) energetic particle precipitation in this thermospheric region is relatively weak. In contrast, the energetic particle input into the auroral thermosphere, for which the NO densities are presented by the central panels of Figures 5.1 and 5.2, is large albeit highly variable. The lower panels are associated with the mid-latitude thermosphere which, in general,

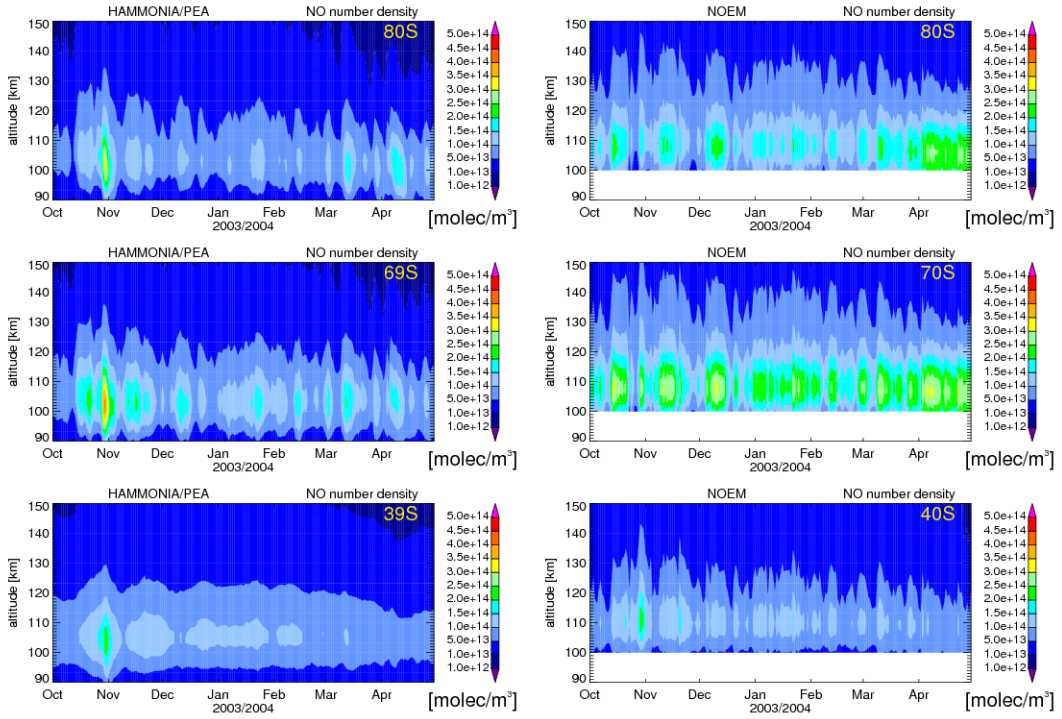

Figure 5.2— As in Figure 5.1 but for 80° (top), 70° (center), and 40° (bottom) south.

is beyond the main particle precipitation area.
Qualitatively good agreement exists between HAMMONIA and NOEM-calculated values. Both HAMMONIA and NOEM show a local maximum of the NO densities in the lower thermosphere, although in HAMMONIA the height of this maximum is in general 5-10 km below the height calculated by NOEM. NOEM calculations indicate that in both hemispheres the maximum NO densities appear within the auroral regions, with the highest values in the winter hemisphere. Except in the north polar cap this behavior is well reflected by HAMMONIA, although it seems that in general HAMMONIA values are somewhat smaller than NOEM-calculated NO densities. However, as can be seen in the upper panels of Figure 5.1 there are three pronounced events in November and December where NO densities in the northern hemisphere at 80° geomagnetic latitude in HAMMONIA significantly exceed the NOEM values at this location. A few additional but smaller events appear in January and February. In the following the causes of differences between HAMMONIA and NOEM-calculated NO densities are examined.

5.2 Discussion of uncertainties

Differences between HAMMONIA and NOEM-calculated NO densities have to be discussed starting with the question of the quality of NOEM values. A multi-year comparison between NOEM-calculated and SNOE-observed NO densities in the lower thermosphere is presented by *Marsh et al.* (2004). It doesn't show a systematic bias in NOEM values. Assuming that the observations are correct, that indicates a general underestimation of lower thermospheric NO densities in HAMMONIA. Potential causes for this behavior are discussed in section 5.2.3. The comparison between NOEM and observations also reveals that in the auroral region, particularly in winter, the empirical model underestimates short-term NO maxima. Additionally, it shows that on average, differences between NOEM and observations increase with increasing latitude below a height of about 120 km. This could be explained by missing measurements at high latitudes during winter (*Barth et al.*, 2003) indicating that events of high NO density which are simulated by HAMMONIA at 69°N and 80°N during late fall and winter may be not unrealistic, but a critical examination is given in section 5.2.2.

5.2.1 Mechanisms of NO production and loss

Regarding the question of causes of the under- and overestimated HAMMONIA-calculated NO densities, the production and loss mechanisms of NO have to be discussed. In the thermosphere, NO is primarily formed by the reaction of molecular oxygen and excited atomic nitrogen:

$$N(^2D) + O_2 \rightarrow NO + O. \tag{5.1}$$

NO is also produced by the reaction of molecular oxygen and ground state atomic nitrogen:

$$N(^4S) + O_2 \rightarrow NO + O \tag{5.2}$$

but this reaction proceeds much more slowly and depends strongly on temperature. The primary NO loss is through the so-called "cannibalistic" reaction with ground state atomic nitrogen:

$$N(^4S) + NO \rightarrow N_2 + O. \tag{5.3}$$

In the presence of solar irradiance, loss of NO by photolysis is also important:

$$NO + h\nu \rightarrow N(^4S) + O. \tag{5.4}$$

The charge transfer reaction:

$$NO + O_2^+ \rightarrow NO^+ + O_2 \tag{5.5}$$

is an additional NO loss mechanism. While reaction 5.3 destroys two odd nitrogen components reactions 5.4 and 5.5 only recycle odd nitrogen, although reaction 5.4

produces a ground state nitrogen atom which can participate in reaction 5.3 destroying one odd nitrogen component. Atomic nitrogen in different energetic states can be formed by the dissociation of N_2:

$$N_2 + p^* \rightarrow N + N + p^*, \tag{5.6}$$

or by ionizing dissociation of N_2:

$$N_2 + p^* \rightarrow N^+ + N + e^- + p^*, \tag{5.7}$$

through the impact of PEPs, solar extreme ultraviolet radiation, or soft X rays. Here, p^* represents a primary PEP, photon, or a secondary electron resulting from the impact of the former.
The impact of hard solar radiation and PEPs can indirectly result in the following ion chemistry reactions which additionally create atomic nitrogen:

$$NO^+ + e^- \rightarrow N + O, \tag{5.8}$$

$$N_2^+ + e^- \rightarrow N + N, \tag{5.9}$$

$$N^+ + O_2 \rightarrow O_2^+ + N, \tag{5.10}$$

$$N_2^+ + O \rightarrow NO^+ + N(^2D). \tag{5.11}$$

For reactions 5.6-5.10 HAMMONIA uses N(^{2}D):N(^{4}S) production ratios which are given in Table 5.1.
Ground state atomic nitrogen is also created by the following reactions:

$$N^+ + O \rightarrow O^+ + N(^4S), \tag{5.12}$$

$$O^+ + N_2 \rightarrow NO^+ + N(^4S), \tag{5.13}$$

and quenching of N(^{2}D) by an electron:

$$N(^2D) + e^- \rightarrow N(^4S) + e^-, \tag{5.14}$$

or by atomic oxygen

$$N(^2D) + O \rightarrow N(^4S) + O. \tag{5.15}$$

Table 5.1— N(^{2}D):N(^{4}S) ratios which are used in HAMMONIA for reactions producing atomic nitrogen of different energetic states.

Reaction	N(^{2}D):N(^{4}S)	Reference
5.6	60:40	(*Rusch et al.*, 1981)
5.7	50:50	(*Rees*, 1982)
5.8	85:15	(*Bates*, 1988)
5.9	50:50	(*Mul and McGowan*, 1979)
5.10	65:35	(*Rees*, 1989)

5.2.2 Potential temporary errors

Short-term overestimations of the NO density at northern high latitudes are indicated in Figure 5.1. From the chemical scheme, presented in the previous section, it can be recognized that the NO budget strongly depends on the influence of PEPs and incident hard solar irradiance. Both directly produce N(^{2}D) and N(^{4}S), the former being the major source and the latter either a sink or a source of NO. Additionally, impact of PEPs and hard solar irradiance initializes sequences of ion reactions resulting in production or loss of NO. Therefore, at first, uncertainties in the representation of the influence of PEPs and EUV radiation on ion chemistry are discussed.

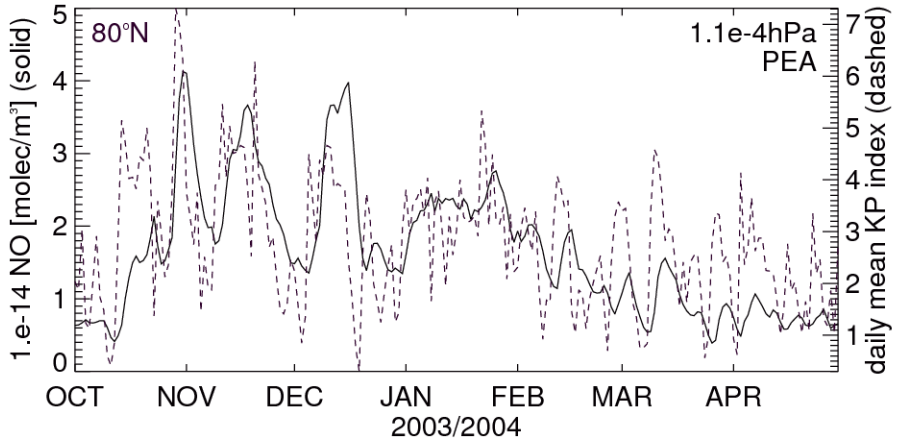

Figure 5.3— Time series of nitric oxide number density at 80°N, on pressure level of $1.1 \cdot 10^{-4}$ hPa (about 105 km) (solid) and daily averaged K_p-index (dashed), ranging from October 2003 to April 2004. Note, that NO number densities are multiplied by 10^{-14}.

Uncertainties in the representation of PEP- and EUV-induced NO production

In HAMMONIA the initial impact of solar EUV radiation is represented by photodissociation and ionization rates which are calculated using a parameterization of *Solomon and Qian* (2005) (see section 3). Dissociation and ion production by PEPs are determined by PEP-induced ionization rates (see sections 4.3). An evaluation of photo-ionization and PEP-induced ionization rates might give information about the causes of differences between NO densities in HAMMONIA and NOEM calculations. Even though it is not possible to assess the ionization rates directly, a comparison between the modeled and ISR measured electron densities gives the possibility to evaluate indirectly the ionization rates and modeled ion chemistry. Such a comparison is presented in *Wissing et al.* (2011). This comparison also provides useful information for the assessment of NO_x production. Appropriate parts of the comparison are presented in section 4.4. Note, that the observational part of the

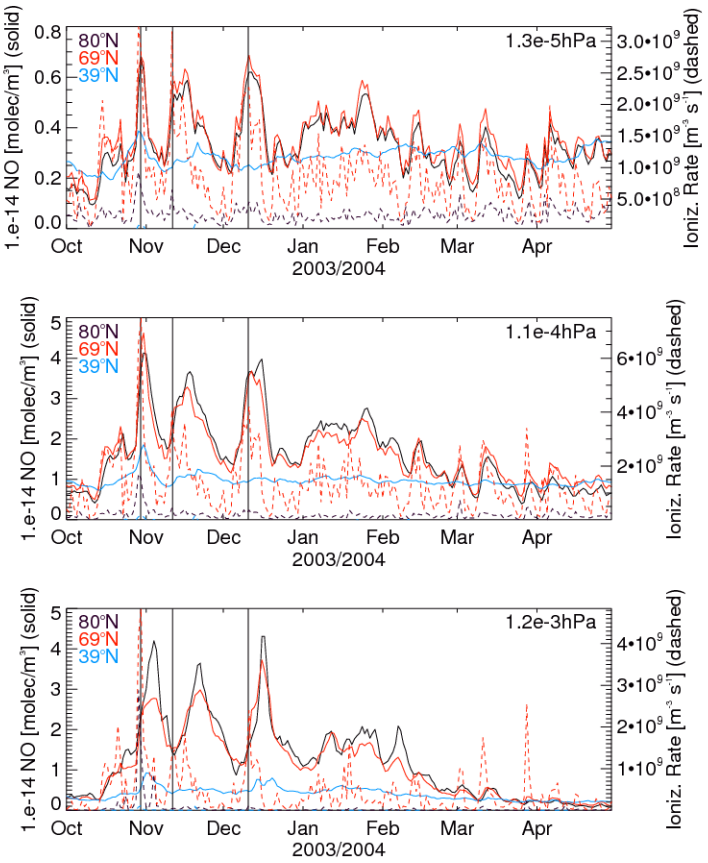

Figure 5.4— Time series of nitric oxide number densities (solid) and ionization rates (dashed) for the time period of October 2003 to April 2004, on pressure levels of $1.3{\cdot}10^{-5}$ hPa (about 120 km, top), $1.1{\cdot}10^{-4}$ hPa (about 105 km, center), and $1.2{\cdot}10^{-3}$ hPa (about 90 km, bottom). Black lines are associated with 80°N, red lines with 69°N, and blue lines with 39°N. Note that NO number densities are multiplied by 10^{-14}. Vertical lines indicate times of three main ionization maxima at $1.3{\cdot}10^{-5}$ hPa.

comparison is based on radar observations which are obtained at a few locations within the polar cap, auroral oval, and mid-latitudes of the northern hemisphere. Since the algorithms for determining ionization rates and ion chemistry are the same for both hemispheres the obtained findings can be adopted to the southern hemisphere. The comparison shows that at night-time, when PEPs are the dominant source of electron production, HAMMONIA tends to underestimate the electron densities in the auroral thermosphere. This indicates an underestimation of PEP-induced ionization rates which might explain, at least partially, that NO densities in the auroral region are smaller in HAMMONIA than in NOEM. No general trend of deviation is shown for electron densities in the polar cap region, even though, it seems that HAMMONIA tends to overestimate electron densities in the polar cap during periods of high geomagnetic activity. As can be seen in Figure 5.3, HAMMONIA-calculated NO densities in the northern polar cap in winter are well correlated with

the geomagnetic activity which is represented by the K_p-index (taken from the National Geophysical Data Center of NOAA (*www.ngdc.noaa.gov*)). Comparison with time-height cross sections of NO densities (see Figure 5.1) reveals that periods when HAMMONIA potentially overestimates NO densities in the northern polar cap coincide with periods of substantially increased geomagnetic activity. This might be an indication that occasionally overestimated NO densities in the NH polar cap are a result of overestimated ionization rates during geomagnetic active periods. An argument against this is provided by Figure 5.4. It shows NO densities and ionization rates at pressure levels corresponding to altitudes where HAMMONIA-calculated NO densities in the NH polar cap are occasionally higher than corresponding NO densities in NOEM. NO densities in both the auroral and the polar cap region are very similar, while the ionization rates in the polar cap at pressure levels where the highest NO densities appear are 5 to 10 times smaller than in the auroral region. Assuming that NO production in the polar winter lower thermosphere is mainly controlled by PEP influence, it is questionable that such low ionization rates in the polar cap are responsible for NO densities similar to values of the auroral region where ionization is significantly higher.
Nonetheless, a few mechanisms have to be discussed which might compensate a weaker PEP-induced NO production in the NH polar cap resulting in NO densities which are similar to auroral NO densities. This discussion focuses on the question if high NO densities in the polar cap region are caused by local PEP-induced NO production or by intrusion of NO which is produced out of the polar cap. The former might indicate a connection between high NO densities and overestimated ionization rates.

The role of temperature and transport

At first it is examined if any heating processes lead to a significant increase of the polar cap temperature resulting in enhanced NO densities due to production by the highly temperature-dependent reaction 5.2 and weakening of the NO destroying reaction 5.3. If the polar cap temperature would substantially exceed the temperature of the auroral region this might explain NO densities in the polar cap which are similar to those of the auroral region. Plotted temperature evolution at three different thermospheric pressure levels and different latitudes (see Figure 5.5) reveal that values in the polar cap region never exceed values in the auroral region significantly. Therefore the temperature theory can be refused.
Further, the role of photolytical NO destruction and transport has to be considered. The question has to be posed if, in contrast to the auroral region, in the polar cap a substantially lower local PEP-induced NO production is balanced by weaker photolytical NO destruction and thus NO densities are similar in both regions. In that case, high NO densities in the NH polar cap could be explained by overestimated ionization rates. Figures 5.6 and 5.7 show the daily averaged PEP-induced ionization rates and NO densities at pressure level 10^{-4} hPa for the

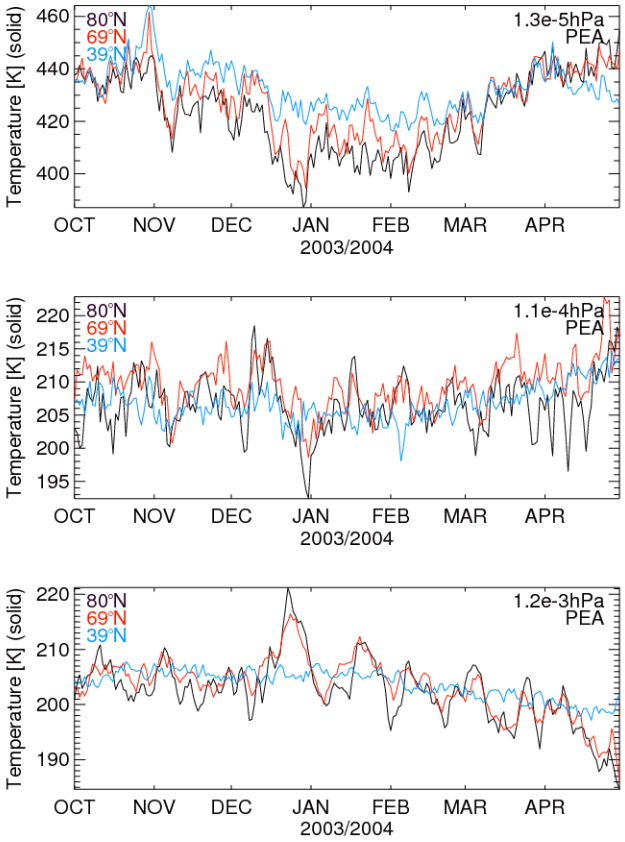

Figure 5.5— Time series of temperature at 80°N (black), 69°N (red), and 39°N (blue) on pressure levels $1.3{\cdot}10^{-5}$ hPa (about 120 km, top), $1.1{\cdot}10^{-4}$ hPa (about 105 km, center), and $1.2{\cdot}10^{-3}$ hPa (about 90 km, bottom) for a time period from October 2003 to April 2004.

time range from the 8-19 November 2003. That time period includes one of the pronounced NO peaks (see Figure 5.4). Ionization rates clearly highlight maxima in the auroral oval as already indicated by Figure 5.4. Figures 5.6 and 5.7 show that the polar night region where NO photolysis vanishes, is centered at the geographic north pole. Its boundary is located at about 79°N on 8 November extending to about 74°N until the end of the considered time period. A substantial NO increase starts on 11 November accompanied by increased ionization. Only for the initial phase the region of highest NO densities approximately coincides with the area of highest ionization rates explaining high NO densities at auroral latitudes. While the ionization pattern continuously reflects the auroral oval, with progressing time NO seems to accumulate within or close to the area where photolytical destruction of NO vanishes. The fact that the polar cap is mainly covered by that area can explain the high values of NO densities at polar cap latitudes as shown by Figure 5.4. Note, that during phases of decreasing PEP-induced ionization NO densities rapidly decrease within that part of the auroral oval which is affected

by photolytical NO destruction, while NO density within a wide range of the polar cap remains elevated. That time lag between the decreases of NO within the auroral oval and the polar cap can also be seen in the central part of Figure 5.4 where the solid black curve which represents the NO density in the polar cap drops later than the red solid curve which is associated with the NO density in the auroral oval. Figures 5.6 and 5.7 indicate that NO photolysis plays an important role for the horizontal distribution of NO. It still remains the question if high NO densities within the polar cap result from local NO production or from horizontal redistribution of NO which is originally created within the auroral oval. Calculated meridional winds for the same time period are presented in Figure 5.8. They reveal a strong variability, which indicates strong horizontal mixing. It can be guessed that in consequence auroral produced NO propagates into the polar cap where it is accumulated resulting in NO densities which are similarly as high as within the auroral region. In this case PEP-induced ionization in the polar cap would only play a secondary role.
However, the comparison between NOEM calculated NO densities and SNOE observed values shows that NOEM tends to underestimate short-time NO maxima in winter and therefore it is possible that events of high NO density which are simulated by HAMMONIA in particular at 80°N during late fall and winter should be not any unrealistic overestimations.

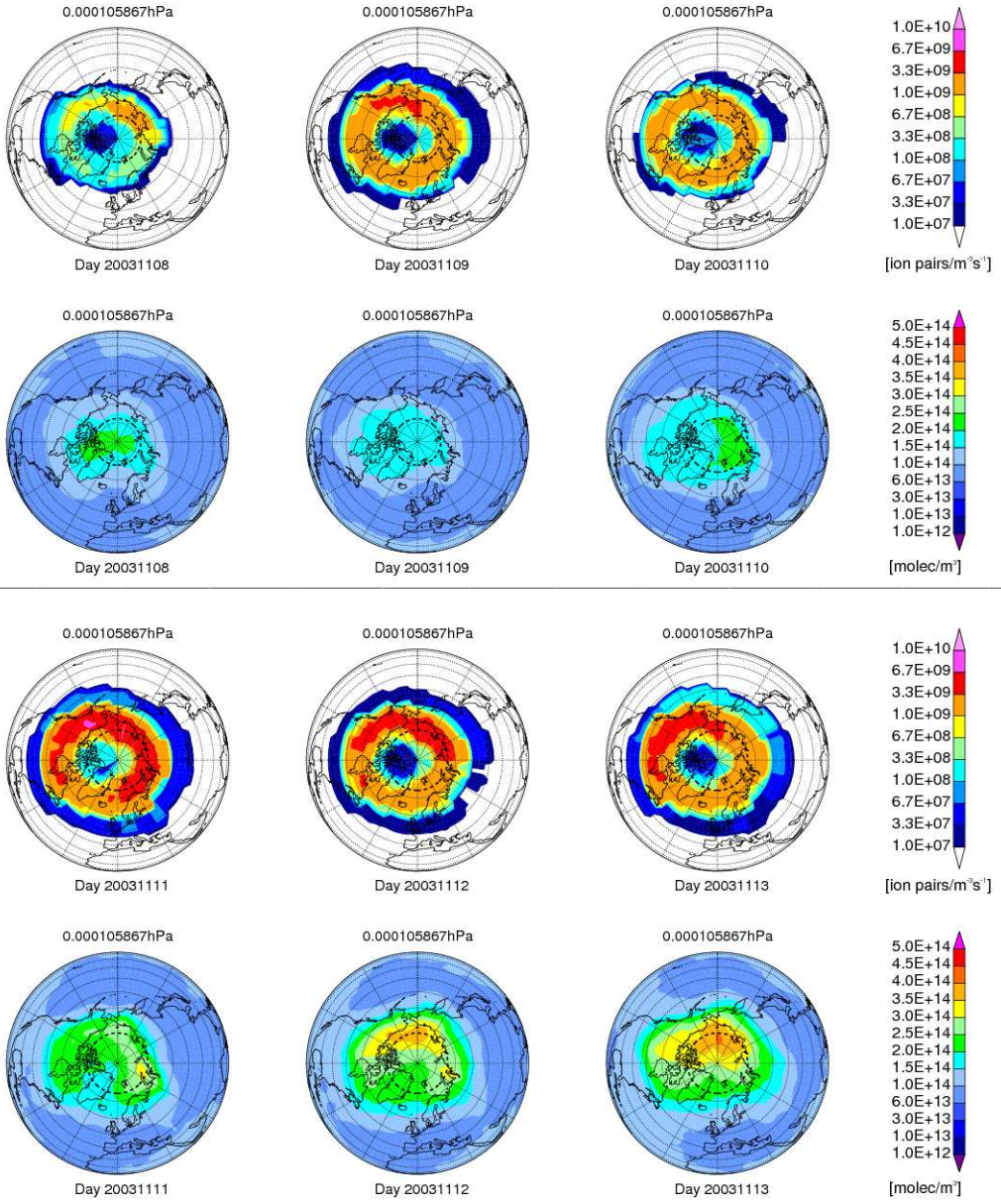

Figure 5.6— Daily averaged PEP-induced ionization rates (1st and 3rd row) and NO densities (2nd and 4th row) for 8th to 13th of November 2003 in the NH. The dashed circle around the geographic pole marks the boundary of the polar night.

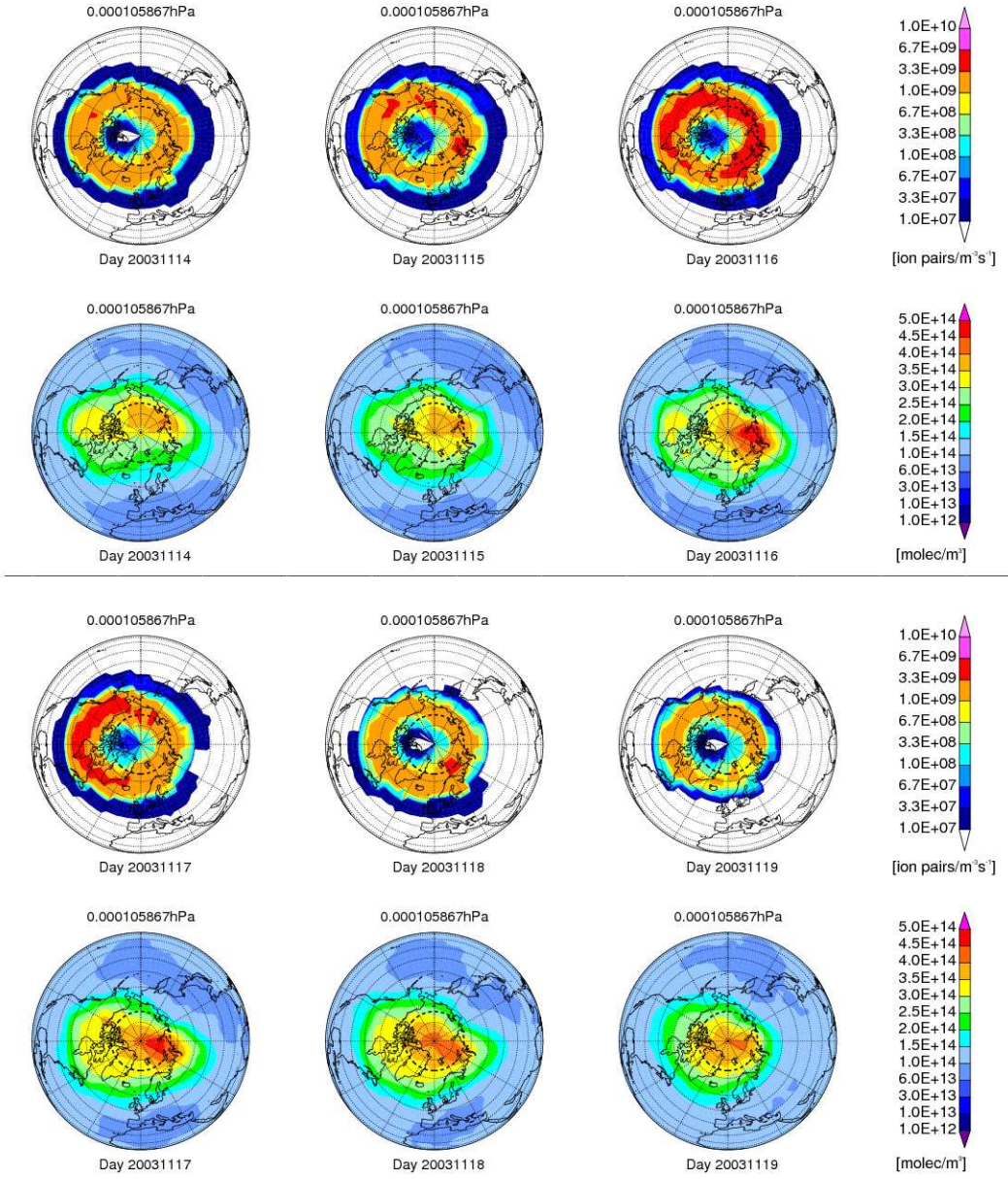

Figure 5.7— Same as Figure 5.6 but for the following six days (14th to 19th of November).

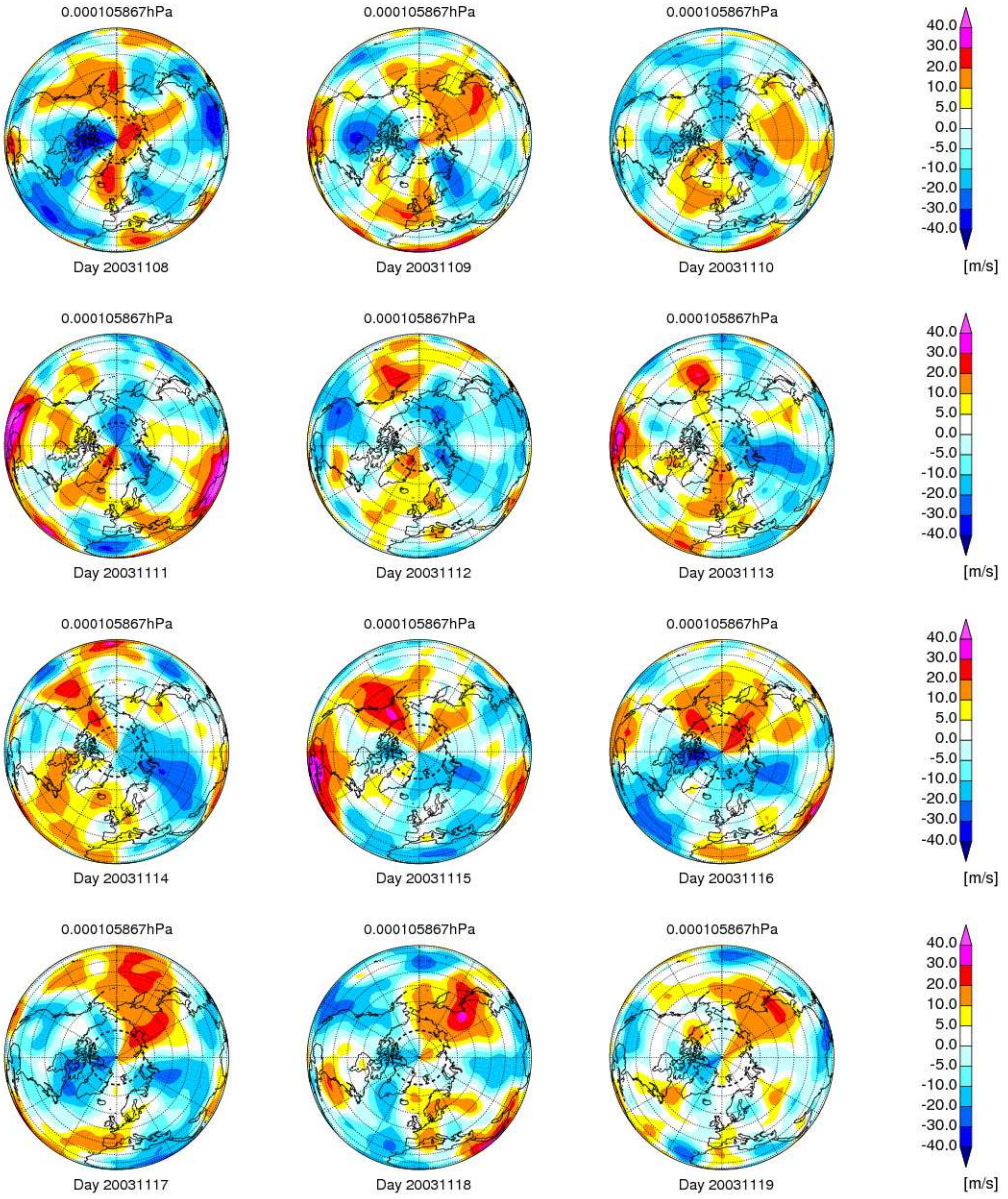

Figure 5.8— Daily averaged meridional wind component for 12 days of November 2003 (8th to 19th) in the NH. The dashed circle around the geographic pole marks the boundary of the polar night.

5.2.3 Potential systematic errors

The previous points are focused on the discussion of short-term overestimated NO densities within the lower thermosphere of the northern polar cap. However, the comparison between HAMMONIA and NOEM reveals mostly an underestimation of HAMMONIA-calculated NO densities. As concluded from the evaluation of the electron densities, too low PEP-induced ionization rates might be responsible for

underestimated NO densities. In the following, additional potential causes for these underestimations are discussed also explaining too low NO densities outside of the auroral zones.

$N(^2D)$:$N(^4S)$ branching ratio

While a large part of $N(^2D)$ which is created by PEP and EUV impact reacts with O_2 in order to produce NO, at ambient temperatures in the lower thermosphere $N(^4S)$ largely destroys NO. Therefore, the NO budget depends crucially on the ratio of $N(^2D)$:$N(^4S)$ production. The values of these branching ratios used in HAMMONIA are listed in Table 5.1. They are obtained from atmospheric measurements or laboratory studies with large uncertainties (*Siskind et al.*, 1989a). Since dissociating excitation of N_2 plays an important role for the PEP- and EUV-caused atomic nitrogen production, the corresponding $N(^2D)$ production yield is often discussed (e.g. *Brasseur and Solomon*, 2005). $N(^2D)$ production yields are suggested ranging from 50% (*Zipf et al.*, 1980) to 70-80% (*Frederick and Rusch*, 1977; *Rusch and Gerard*, 1980). HAMMONIA uses values of 50% for reaction 5.7 and 60% for reaction 5.6. These values are rather in the lower part of the suggested range and therefore it can not be excluded, that low NO densities are caused by a too low $N(^2D)$ production yield.

The role of temperature

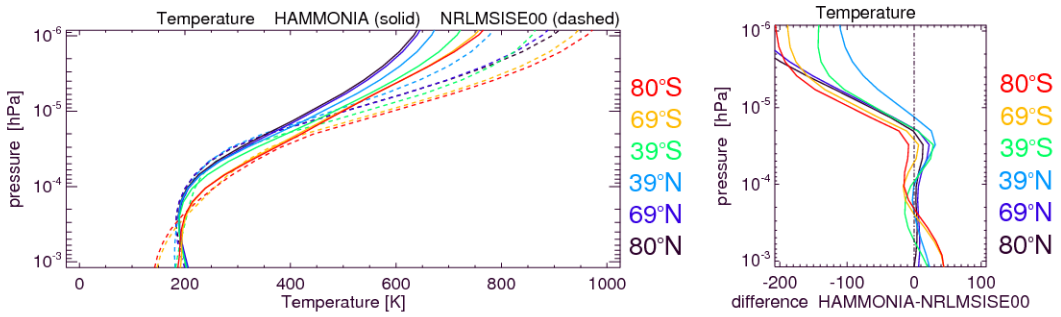

Figure 5.9— Left: Monthly averaged temperature profiles obtained from HAMMONIA simulation PEA (solid) and from NRLMSISE-00 (dashed) for the same geomagnetic latitudes as in Figures 5.1 and 5.2 for January 2004. Right: Difference HAMMONIA-NRLMSISE-00 of the profiles from the left. Units are K.

As mentioned above, $N(^4S)$ is largely a sink of NO. That is in particular the case in the lower thermosphere where temperatures are low so that reaction 5.2 does not contribute significantly to NO production. But in the thermosphere the temperature increases with increasing altitude, as can be seen in Figure 5.9, resulting in enhanced NO production through reaction 5.2. Figure 5.9 also shows a comparison

between temperatures calculated by HAMMONIA and the NRLMSISE-00 empirical model of the atmosphere (*Picone et al.*, 2002). The NRLMSIS database includes ground-, rocket-, and satellite based measurements. The empirical model takes into account location, time, geomagnetic activity, and F10.7 solar radio flux as a solar EUV proxy. The comparison indicates that HAMMONIA underestimates the temperature above $2{\cdot}10^{-5}$ hPa. Consequently, NO production by reaction 5.2 is underestimated and more N(^{4}S) remains which can destroy NO. This might explain the underestimation of NO densities, at least in higher altitudes, in HAMMONIA. *Siskind et al.* (1989a) describe that NO can propagate downward due to diffusion increasing the NO density in the lower thermosphere. Thus, underestimated NO production in higher altitudes can also reduce NO densities below. The effect should be small at auroral latitudes where the main production of NO occurs in the lower thermosphere and therefore the effect of downward diffusion is less effective.

N(^{2}D) quenching by atomic oxygen

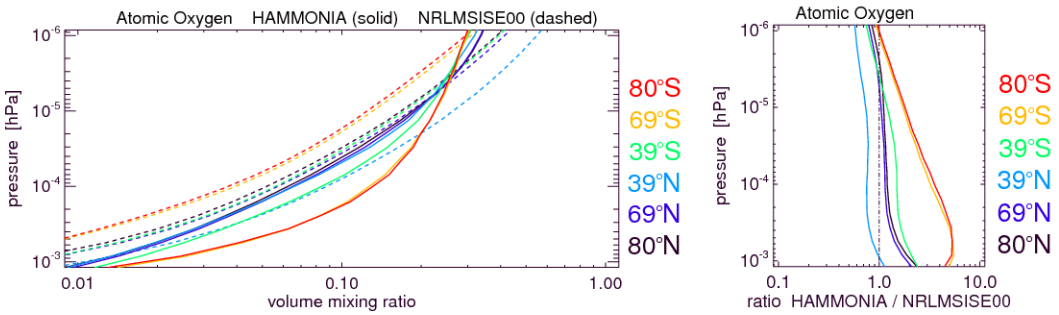

Figure 5.10— Left: Monthly averaged atomic oxygen volume mixing ratio profiles obtained from HAMMONIA simulation PEA (solid) and from NRLMSISE-00 (dashed) for the same geomagnetic latitudes as in Figures 5.1 and 5.2 for January 2004. Right: Ratio HAMMONIA/NRLMSISE-00 of the profiles from the left panel.

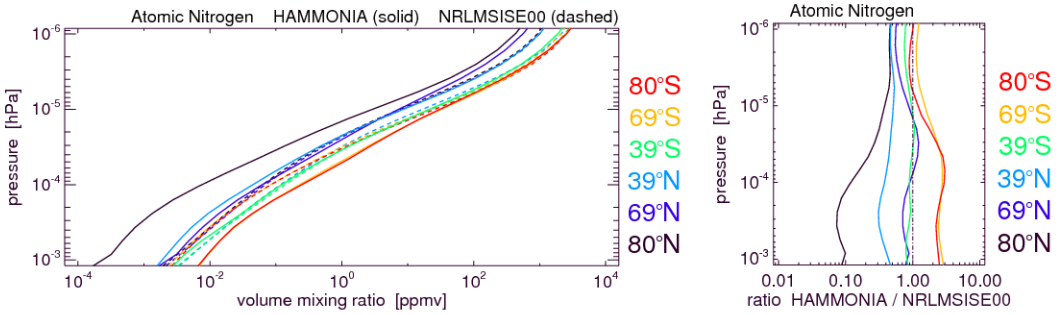

Figure 5.11— Same as in Figure 5.10 but for N(^4S) volume mixing ratio.

An additional cause of uncertainty of the modeled NO concentration is the strength of $N(^2D)$ quenching by atomic oxygen (see reaction 5.15) (*Siskind et al.*, 1989a,b). The quenching rate is determined by the reaction rate coefficient and by the O concentration. While slowing down reaction 5.15 leaves more $N(^2D)$ which can react with O_2 producing NO, speed up of $N(^2D)$ quenching leads on the one hand to a decrease of $N(^2D)$ which results in a weakening of NO producing reaction 5.1 and on the other hand to an increase of $N(^4S)$ which can rapidly destroy NO by reaction 5.3. In the literature rate coefficients are given ranging from $<10^{-12}$ $cm^{-3}s^{-1}$ (*Frederick and Rusch*, 1977) to $>10^{-11}$ $cm^{-3}s^{-1}$ (*Jusinski et al.*, 1988). HAMMONIA uses a relatively small value of $6.9{\cdot}10^{-13}$ $cm^{-3}s^{-1}$ (*Fell et al.*, 1990) thus it is unlikely that the rate coefficient causes an overestimation of $N(^2D)$ quenching. More likely is an overestimation of the atomic oxygen concentration which causes too much $N(^2D)$ quenching. Figure 5.10 shows a comparison of O volume mixing ratio altitude profiles for January 2004 and different geomagnetic latitudes calculated by HAMMONIA and NRLMSISE-00 empirical model. The comparison with the empirical model indicates an overestimation of atomic oxygen in HAMMONIA in the SH auroral and polar regions. For $N(^4S)$ the comparison is illustrated in Figure 5.11. It can be seen that in the lower SH auroral and polar thermosphere where O concentrations are larger in HAMMONIA than in NRLMSISE-00 also the $N(^4S)$ concentrations exceeds the value from the empirical model. This may be caused by a too strong quenching of $N(^2D)$ that produces $N(^4S)$. Additionally, less $N(^2D)$ is available to produce NO, resulting in less NO which can destroy $N(^4S)$.

5.3 Conclusions

Nitric oxide densities calculated by HAMMONIA are compared with NO densities obtained from the nitric oxide empirical model for six geomagnetic latitudes within the lower thermosphere. Qualitatively HAMMONIA reproduces thermospheric NO very well. In general, NO densities are somewhat too small in HAMMONIA, with the relative differences enhancing with increasing altitude. It is very likely that several processes acting alone or together are responsible for that behavior.
A comparison of HAMMONIA modeled and ISR measured electron densities indicates that HAMMONIA tends to underestimate PEP-induced ionization rates in the auroral thermosphere resulting in underestimated NO production in HAMMONIA. In comparison to temperatures calculated by NRLMSISE-00 above pressure level of $2{\cdot}10^{-5}$ hPa HAMMONIA temperatures are increasingly underestimated with increasing altitude. That results in reduced NO production by reaction of $N(^4S)$ with molecular nitrogen (reaction 5.2) which is important at higher altitudes. Downward transport can bring this signal to lower altitudes resulting in underestimated NO densities.
The comparison of HAMMONIA- and NRLMSISE-00-calculated atomic oxygen indicates an overestimation of atomic oxygen, particularly in the SH auroral and polar thermosphere. Since this leads to enhanced quenching of $N(^2D)$ by atomic oxygen,

on the one hand less N(^{2}D) is available to produce NO and on the other hand more N(^{4}S) is formed which destroys NO. While for the most time and regions HAMMONIA seems to underestimate NO densities in the lower thermosphere of the NH polar cap HAMMONIA seems to overestimate NO densities occasionally. Since the empirical model suffers from substantial uncertainties in this region, it is not clear if HAMMONIA really overestimates NO there. However, a possible reason might be overestimated PEP ionization rates. It also seems possible that NO is shifting poleward from the auroral region and therefore, it escapes from photolytical destruction.

Chapter 6

Investigation of Particle Effects on the Atmosphere

This chapter considers several aspects of the influence of particle precipitation on the atmosphere. At first, the combined effect of precipitating protons, electrons, and α-particles on chemical key components and temperature are discussed including a discussion of the mechanisms responsible for PEP-caused temperature changes. A substantial aspect of this work is the assessment of the contributions of precipitating electrons and α-particles with respect to the influence of the complete PEP spectrum. Finally, a downward transport event is considered which represents an important mechanism of interaction between the upper and the middle atmosphere. In that context the role of precipitating electrons is also discussed.

6.1 The combined influence of precipitating protons, electrons, and alpha-particles

The investigation of the combined influence of the complete PEP spectrum focuses on an altitude range covering the stratosphere, mesosphere, and parts of the thermosphere, although the underlying model simulations also cover the troposphere. The period from October 2003 to April 2004 is considered which includes the pronounced Halloween particle precipitation event as well as smaller particle precipitation events.
It must be mentioned that a series of previous model studies have discussed the influence of the Halloween event or other particle precipitation events on atmospheric parameters (e.g. *Siskind et al.*, 1989a; *Verronen et al.*, 2002; *Jackman et al.*, 2005; *Rohen et al.*, 2005; *Semeniuk et al.*, 2005; *Wissing et al.*, 2010). While these model studies take only discrete parts of the PEP spectrum into account or consider particle precipitation only in discrete altitude and latitude regions, respectively, the present work considers precipitation of nearly the complete energetic particle spectrum into the entire atmosphere up to an altitude of about

250 km. This allows, on the one hand, an improved representation of the actual particle precipitation and, on the other hand, simulation of potential interactions of PEP effects between different atmospheric layers and regions. Therefore, the examination of the influence of the complete particle spectrum on chemical species and temperature not only serves as reference for the assessment of the contribution of individual particle classes. It also provides the possibility to investigate PEP effects which could not be reflected by conventional modeling approaches. This involves a consideration of energetics focusing on effects not displayed by previous model studies. In order to show the influence of the entire particle spectrum on chemical composition, temperature and related quantities values calculated from model experiment involving precipitating protons, electrons, and α-particles (experiment PEA) are compared with values from the experiment without any particle forcing (experiment REF). Note that usually ensemble mean values are considered in the following. Also in this chapter the terms of the atmospheric layers are used. In all figures the altitude is represented by the corresponding pressure level. Therefore, it is again referred to Figure 1.1 which gives an overview of atmospheric layers and their associated pressure and altitude levels.

6.1.1 NO_x and HO_x

The time evolution of the NO_x number density under the influence of the complete precipitating particle spectrum is shown in the left panels of Figures 6.1 and 6.2. It is presented for geomagnetic latitudes of 83°, 69°, and 39° north and south representing the polar caps, auroral regions, and mid-latitudes, respectively. Therefor, the model output is interpolated from geographic coordinates to the geomagnetic coordinate system whose north pole is assumed to be at 79.7°N geographic latitude and 71.7°W geographic longitude. This position corresponds to the location of the geomagnetic pole in late 2003 as identified by the National Geophysical Data Center of NOAA (*www.ngdc.noaa.gov*). Note that appreciable short-term displacements of the geomagnetic poles during geomagnetic storms are not taken into account for the interpolation to geomagnetic coordinates.
For all the regions considered in Figures 6.1 and 6.2 the atmosphere exhibits a remarkable NO_x layer in the altitude region of the mesopause and lower thermosphere with the highest NO_x densities in winter. Above and in the mesopause region the NO_x number densities are quite similar to the NO number densities presented in Figures 5.1 and 5.2. As mentioned in section 5.1 in that altitude region NO_x is mainly represented by NO produced by the influence of hard solar irradiance and by PEPs.
Another layer of large NO_x number densities can be found in the stratosphere (the dotted line marks the stratopause). But it has to be mentioned that, even though the number density of NO_x in the stratosphere substantially exceeds thermospheric values, in consequence of increasing absolute density with increasing pressure, the mixing ratio is by several orders of magnitudes smaller in the stratosphere. A

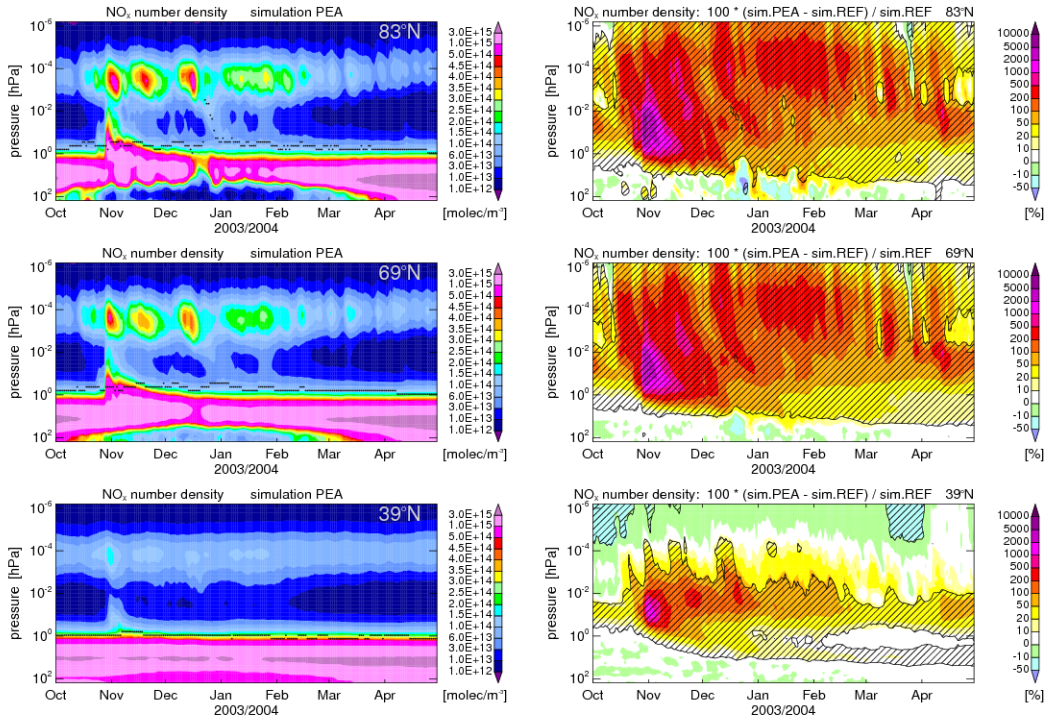

Figure 6.1— Ensemble mean of NO_x number density from simulation PEA (left) and relative differences between ensemble means of simulation PEA and simulation REF (right) for the time period of October 2003-April 2004 at northern hemispheric geomagnetic latitudes of 83° (top), 69° (center), and 39° (bottom). Units are molecules per m^3 and percent, respectively. Shaded areas on the right indicate statistical significance larger than 95%. Dotted lines on the left indicate the stratopause.

strong NO_x increase which is associated with the Halloween event occurs at the end of October covering an altitude range from the upper stratosphere up to the lower thermosphere. The NO_x increase is most substantial in the NH auroral and polar region and relatively weak equatorward of the auroral region. Another NO_x increase can be found in the NH polar and auroral mesosphere in late December and early January accompanied by a remarkable displacement of the stratopause up to higher altitudes. Here, the time evolution indicates a descent of NO_x which stems from the mesopause and lower thermosphere. Such a severe downward transport event is an impressive example of an interaction between different atmospheric layers and was not reflected by conventional modeling approaches. Although it is thought that the downward transport event itself is not driven by particle precipitation, PEP-induced NO_x production in the upper atmosphere is necessary that downward transport events lead to significant increases of NO_x in the middle atmosphere. This indicates that a realistic modeling of upper atmospheric chemistry, in particular NO_x production by PEPs in the lower thermosphere, is important for an accurate description of middle atmospheric chemistry. A detailed discussion of this downward transport event is given in section 6.3.

In order to demonstrate the effective influence of PEPs on NO_x, relative changes

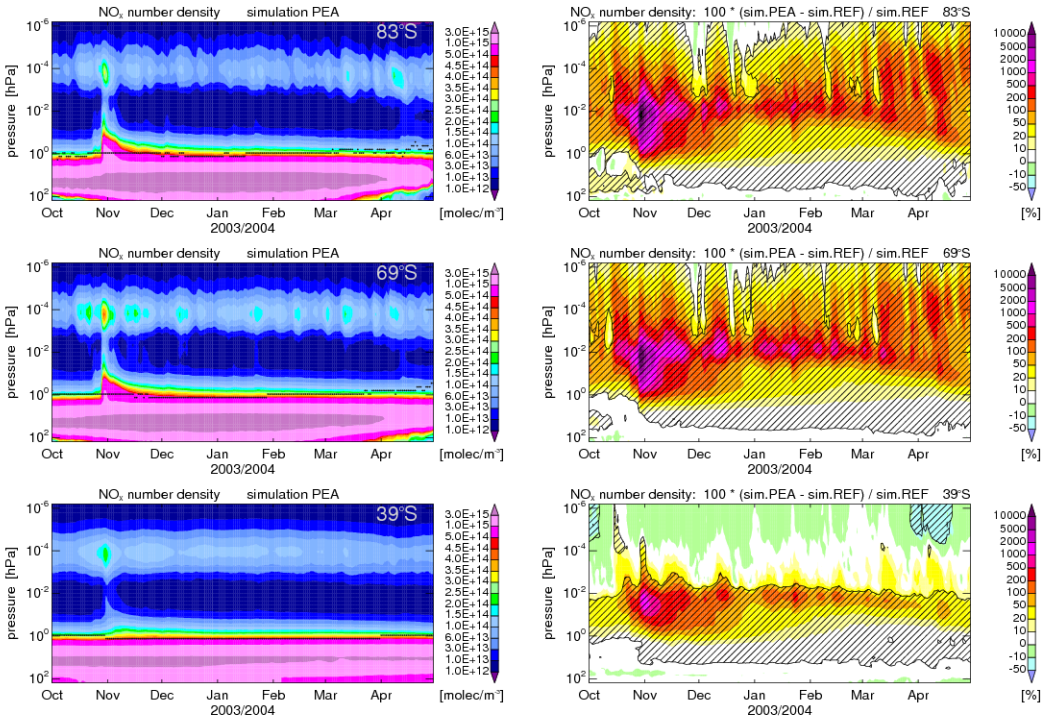

Figure 6.2— The same as Figure 6.1 but for the southern hemisphere.

between simulation PEA and simulation REF are presented by the right panels of Figures 6.1 and 6.2. The strongest PEP-induced NO_x enhancements occur in the mesosphere and upper stratosphere in both hemispheres during the Halloween event in late October and during the following days. In the auroral and polar regions these enhancements significantly exceed 1000%. Significant PEP effects are also shown for nearly the entire remaining altitude and time range at polar and auroral latitudes. Here, PEPs obviously contribute substantially to the NO_x production or even dominate the NO_x production.

Note the dominating influence of PEPs on the NO_x content in the lower thermosphere and upper mesosphere in winter. Here, PEPs lead to NO_x enhancements of more than 200% resulting in considerable NO_x densities. In the summer hemisphere the strongest relative PEP effects occur in the mesosphere, where PEPs cause increases of up to 1000%. However, the resulting absolute NO_x-content is relatively small. Outside of the major precipitation regions a substantial influence of PEPs on NO_x is mostly constrained to lower mesospheric heights. Here, the NO_x increases usually amount to 20-200% and more than 1000% during the Halloween event. However, significant PEP-induced NO_x decreases occur temporarily in October, March, and April in the thermosphere at mid-latitudes. This behavior contradicts the findings of previous studies (e.g. *Siskind et al.*, 1989a; *Dobbin et al.*, 2006) showing substantial increases of NO concentrations in the middle latitude lower thermosphere in consequence of auroral particle precipitation. In the middle

atmosphere PEP-induced NO_x changes in HAMMONIA show qualitatively good agreements with that of previous studies of *Jackman et al.* (2005); *Krivolutsky et al.* (2005); *Jackman et al.* (2008, 2009), although a comparison with the results of *Jackman et al.* (2005, 2009) indicates that on a time scale of longer than a few weeks the PEP-induced NO_x increase is significantly stronger in HAMMONIA. That seems plausible since only HAMMONIA considers a series of electron dominated PEP events which follow the proton dominated Halloween event which is considered by all model studies. Even though uncertainties concerning the modeled NO_x concentrations exist (as shown in chapter 5) the present study shows for the first time the combined NO_x response to an extreme solar energetic particle precipitation event and subsequent solar and magnetospheric particle precipitation in such a comprehensive altitude range.

It must be mentioned that the influence of the Halloween storms on NO_x is recently examined by a comprehensive comparison study between observational data and simulations by a couple of models (*Funke et al.*, 2011). That study, which also involves HAMMONIA, is focused on short-term PEP effects in the middle atmosphere. All involved models use the same ionization rates of precipitating protons and electrons. These rates are identical to those used in the present work. But in contrast to this work the inter-comparison study does not consider precipitating α-particles. The main difference between the inter-comparison study and the present work is that the former explicitly excludes consideration of any effects of particle precipitation into the upper atmosphere. The inter-comparison study is useful to improve the knowledge of short-term effects of a severe PEP event on chemical processes in the middle atmosphere. But it is not convenient to describe the actual influence of PEPs on the atmosphere involving interactions between the upper and middle atmosphere. Nevertheless, within the inter-comparison study, which is discussed more in detail in section 6.1.3, the HAMMONIA modeled NO_x response to the Halloween event agrees well with the majority of model results and observations.

In contrast to the inter-comparison study, which considers effects of the Halloween storms on the middle atmosphere, a model study of *Dobbin et al.* (2006) discusses the time evolution of NO during a few days of the Halloween storm period focusing on thermospheric heights and auroral particle precipitation. The results of that study indicate, in consistence with the HAMMONIA simulation, a substantial increase of NO during the Halloween storm period in the lower thermosphere. In contrast to the HAMMONIA simulation, model results of *Dobbin et al.* (2006) indicate that the region of the highest NO densities in the southern hemisphere is considerably shifted to near-equatorial latitudes where NO densities exceed by far those at any region of the northern hemisphere. Observations of NO densities in the lower thermosphere, as shown by *Barth et al.* (2003), do not confirm the behavior which is described by *Dobbin et al.* (2006).

Similar as for the previous consideration of NO_x, Figures 6.3 and 6.4 show the time evolution of the HO_x number density calculated in experiment PEA and the relative differences between simulations PEA and REF. Continuously high HO_x densities

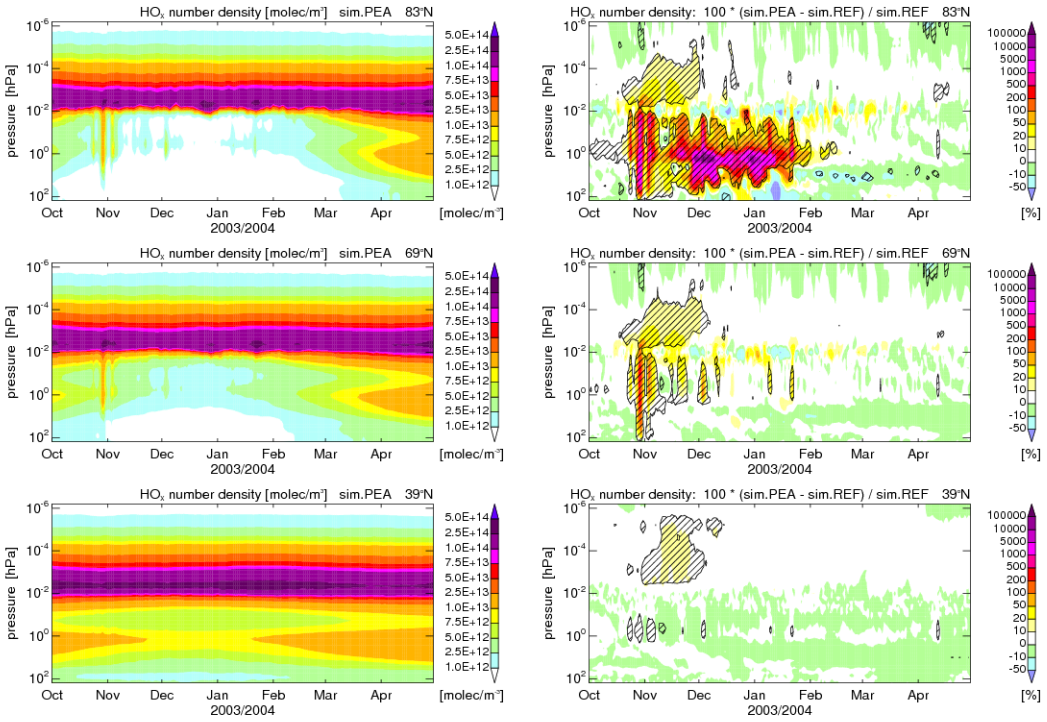

Figure 6.3— Ensemble mean of HO_x number density from simulation PEA (left) and relative differences between ensemble means of simulation PEA and REF (right) for the time period of October 2003-April 2004 at northern hemispheric geomagnetic latitudes of 83° (top), 69° (center), and 39° (bottom). Units are molecules per m^3 and percent, respectively. Shaded areas on the right indicate statistical significance larger than 95%.

can be found in the upper mesosphere above about 10^{-2} hPa with the highest values in the summer hemisphere. In addition, a local HO_x maximum can be found in summer in the vicinity of the stratopause. The higher HO_x concentrations in summer are thought to result from a stronger photolysis of H_2O (*Solomon et al.*, 1983). Remarkable enhancements of HO_x in the NH mesosphere and stratosphere in late October and early November show the influence of the Halloween storms. In contrast to NO_x, substantial PEP-induced HO_x enhancements are mostly short-term and constrained to the days of the strongest particle activity. During the particle storms in late October and early November, PEPs lead to short-term HO_x increases of 200-1000% in the lower mesosphere and stratosphere of the NH polar and auroral regions. In all other regions during the Halloween storms PEP effects are significantly weaker. A supposedly significant longer-term PEP-effect in the NH polar mesosphere and stratosphere can be found in December and January. But it should be noted that in this region and time the absolute HO_x concentrations are by orders of magnitude smaller than anywhere else in the considered altitude and time range. Therefore, the effective PEP influence should not be over-interpreted. Probably, a series of very weak PEP events are responsible for the PEP-induced HO_x enhancements in the middle atmosphere in winter. In the summer hemisphere

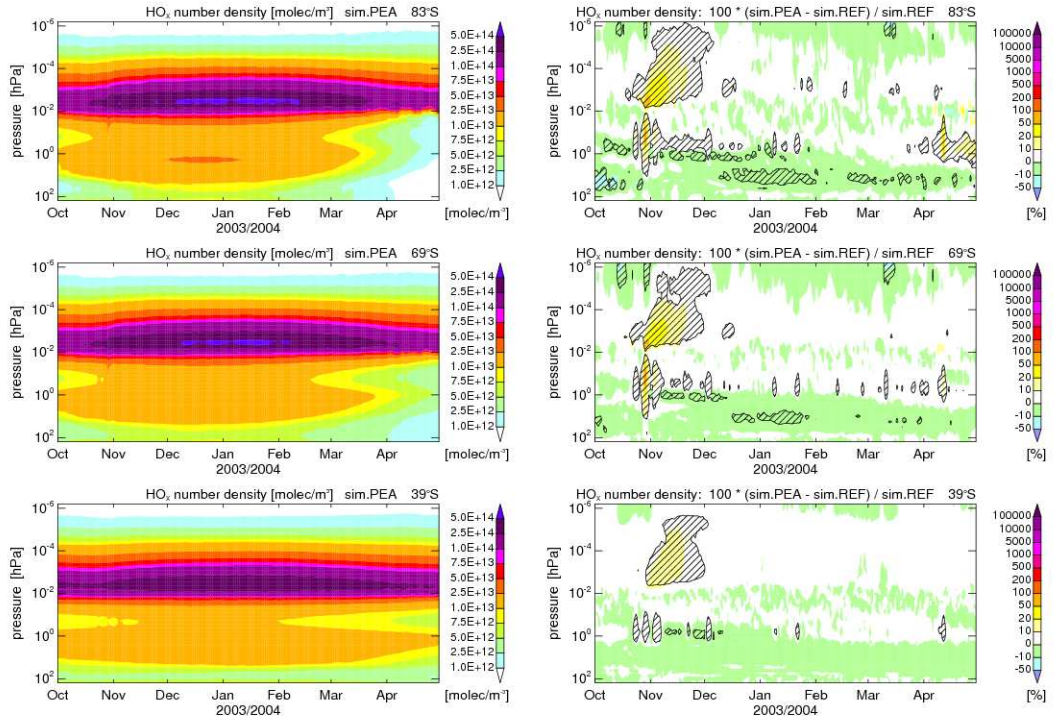

Figure 6.4— Same as figure 6.3 but for the southern hemisphere.

where HO_x is mainly produced by photolysis of H_2O the relative PEP effect on HO_x is rather weak.

6.1.2 Ozone

The previous section highlights PEP-induced changes of NO_x and HO_x. The present section focuses on the influence of PEPs on ozone. Ozone is affected by PEPs since components of NO_x and HO_x are involved in ozone destroying catalytic cycles which are given by the following reactions:

$$NO + O_3 \rightarrow NO_2 + O_2 \tag{6.1}$$

$$NO_2 + O \rightarrow NO + O_2 \tag{6.2}$$

$$H + O_3 \rightarrow OH + O_2 \tag{6.3}$$

$$OH + O \rightarrow H + O_2 \tag{6.4}$$

$$OH + O_3 \rightarrow HO_2 + O_2 \tag{6.5}$$

$$HO_2 + O \rightarrow OH + O_2. \tag{6.6}$$

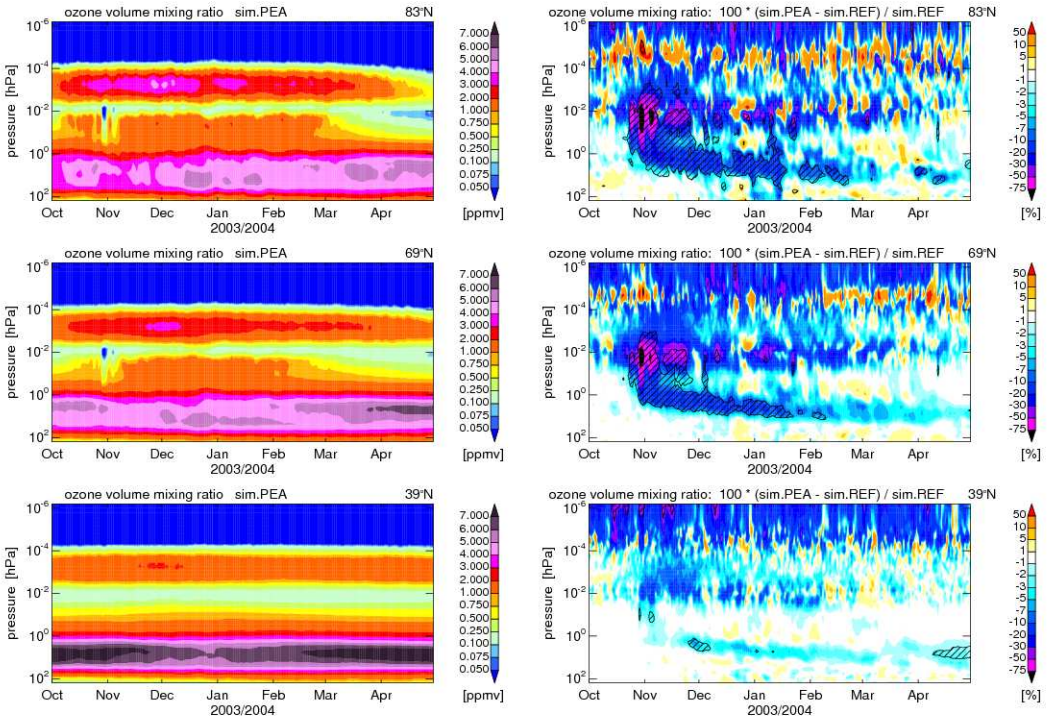

Figure 6.5— Ensemble mean of ozone volume mixing ratio from simulation PEA (left) and relative differences between ensemble means of simulation PEA and REF (right) for the time period of October 2003-April 2004 at northern hemisphere geomagnetic latitudes of 83° (top), 69° (center), and 39° (bottom). Units are ppmv and percent, respectively. Shaded areas on the right indicate statistical significance larger than 95%.

These cycles result in a PEP-induced ozone depletion which is indicated in Figures 6.5 and 6.6 at particular geomagnetic latitudes of both hemispheres. A strong PEP-induced ozone depletion occurs in the mesosphere during the time period of the Halloween storms. Here the ozone reduction is stronger in the winter hemisphere where nearly all ozone is destroyed at certain altitudes. These inter-hemispheric differences are in good agreement with observations (*López-Puertas et al.*, 2005) and theoretical studies (*Solomon et al.*, 1983; *Rohen et al.*, 2005). These studies pointed out that PEP-induced destruction of odd oxygen (O, O_3) is more effective during night-time when HO_x production by H_2O photolysis is weak. However, it should be noted that this mechanism rivals with the effect of reduced intensity of the ozone destroying cycles in absence of solar radiation that is shown by model simulations of *Krivolutsky et al.* (2006). Figures 6.5 and 6.6 also show that in the mesosphere the original ozone concentration recovers soon after the PEP events due to the relatively short life time of HO_x. As can be seen by a comparison with Figures 4.1-4.3 the ozone decline and recovery within the mesosphere reflects the distinctive pattern of the ionization events during the major Halloween storm and two smaller events appearing a few days before and after the major event. The relatively strongest PEP-induced ozone decrease can be found in winter at pressure

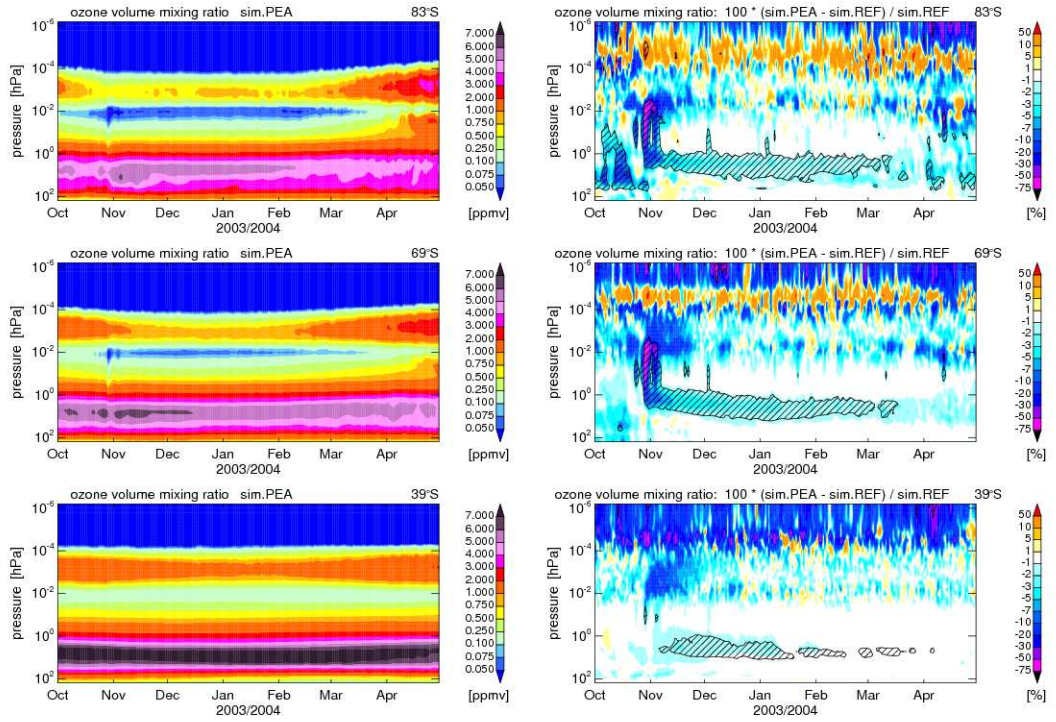

Figure 6.6— Same as figure 6.5 but for the southern hemisphere.

level of about 10^{-2} hPa. However, in that altitude range the absolute ozone volume mixing ratio is relatively small. A long-term ozone depletion can be found in the lower mesosphere and upper stratosphere after the Halloween event. Here, the decrease, which lasts for several months, amounts to 10-30% at high northern latitudes and less than 10% at middle latitudes and in the southern hemisphere. A comparison with the PEP-induced enhancements of NO_x and HO_x indicates that short-term ozone decrease in the mesosphere is mainly a result of PEP-induced HO_x enhancements, while long-term effects are caused by particle induced NO_x increase which has a longer life time than HO_x in the considered altitude region.

6.1.3 HAMMONIA in a inter-comparison between models and observational data

The previous sections discuss the influence of the complete PEP spectrum on NO_x, HO_x and ozone. These chemical species are not arbitrarily chosen. As described in section 6.1.4 ozone plays an important role for the energy budget in a wide range of the atmosphere. Section 6.1.2 emphasizes the importance of NO_x and HO_x for the ozone budget. It must be mentioned that PEPs significantly affect a series of other species which indirectly influence the ozone budget. For example, a series of chemi-

cal processes can produce the NO_y reservoir species N_2O_5, HNO_3, and $ClONO_2$ and thereby deactivate NO_x. Otherwise, PEP influence can activate chlorine species, which in turn can participate in ozone destruction.
A comprehensive study of the influence of the Halloween PEP event on diverse chemical species which are relevant for the ozone budget is given by *Funke et al.* (2011). That study compares MIPAS observations with results of 10 general circulation and chemical transport models (GCMs, CTMs) including HAMMONIA. The comparison focuses on short-term effects of the Halloween particle precipitation event on the middle atmosphere at northern middle and high latitudes. This analysis is carried out in the framework of the HEPPA model versus data inter-comparison initiative which has brought together scientists involved in atmospheric modeling and scientists involved in generation and analysis of observational data. This activity was originated during the first HEPPA (High-Energy Particle Precipitation in the Atmosphere) workshop in May 2008 in Helsinki. For the inter-comparison study all the involved models use the ionization rates provided by AIMOS involving precipitating protons and electrons.
The intention of the comparison is an evaluation of the overall ability of atmospheric models to reproduce observed atmospheric changes due to a particle precipitation event. The analysis focuses on local effects of particle precipitation into the middle atmosphere and explicitly excludes regions of significant downwelling. Consequently, descending NO_x from the upper atmosphere and its effects on other chemical species is not included in the study.
The analysis of the ozone response to the particle precipitation event shows quantitatively and spatially good agreements between HAMMONIA simulation and MIPAS observation. The modeled PEP-induced ozone losses agree on average within 5% with the observations. It is also shown that PEP-induced NO_y changes are well reproduced by HAMMONIA. Although, HO_x components are not explicitly considered in the comparison study the agreements of the modeled short-term PEP-induced ozone response with observations indicates that the parameterization of the PEP-induced HO_x production (*Solomon et al.*, 1981) which is used in HAMMONIA in combination with the PEP-induced ionization rates works well.
The comparison also considers dynamical aspects. It indicates that horizontal mixing of air between polar and middle latitudes in winter is overestimated in HAMMONIA simulations. This must be taken into account, particularly, when longer-term PEP effects are considered.

6.1.4 Temperature

Section 6.1.2 was concerned with the influence of PEPs on ozone. Although, ozone is a minor chemical component in the entire atmosphere it is of particular importance for the energy balance over wide altitude ranges. The reason is that ozone is an important absorber of solar radiation at several short wave spectral bands (*Hartley*, 1880; *Chappuis*, 1882; *Huggins and Huggins*, 1890). Besides the effect of ozone, PEPs can affect a series of other processes which are relevant for

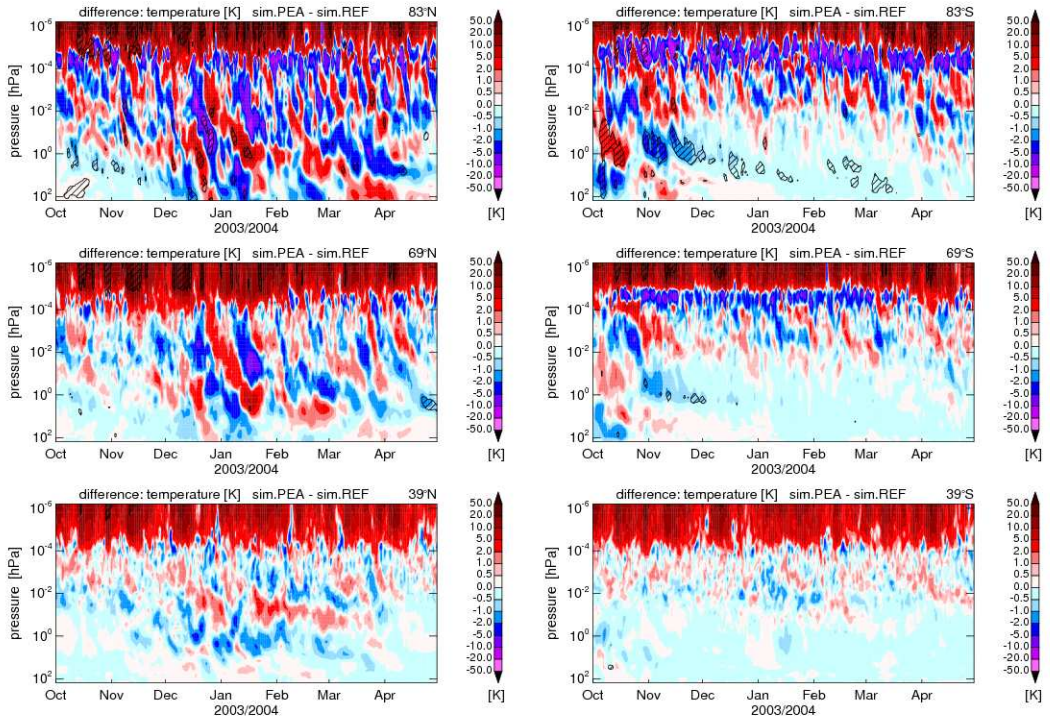

Figure 6.7— Differences of ensemble mean temperatures between simulation PEA and REF for the time period of October 2003-April 2004 at geomagnetic latitudes of 83° (top), 69° (center), and 39° (bottom) in the northern hemisphere (left) and in the southern hemisphere (right). Shaded areas indicate statistical significance larger than 95%.

temperature. The spectrum of those processes comprises the effects of heating by exothermic chemical reactions, heating by dissipation due to interactions between neutral and charged species, radiative cooling by nitric oxide which is produced by PEP impact, and temperature advection and related adiabatic processes in consequence of PEP-caused changes of the circulation pattern. In the following the resulting temperature changes are studied.

Figure 6.7 shows the temperature effects of the complete precipitating particle spectrum for the same range of time, altitude, and geomagnetic latitudes as considered in the previous sections for chemical components. The differences between temperatures of simulation PEA and REF show a pronounced variability. Particularly below the thermosphere the sign of temperature effects varies strongly. Here, the most signals are associated with noise. Statistically significant PEP-induced temperature effects are indicated by the small shaded areas. They can be found, on the one hand, in October and November in the lower mesosphere and stratosphere at southern high latitudes. It can be guessed that these temperature changes result, at least partly, from the ozone effect, which is discussed in the next section. On the other hand, significant short-term temperature effects appear in December and January in the mesosphere and stratosphere at northern high latitudes. They seem to be associated with a sudden stratospheric warming event

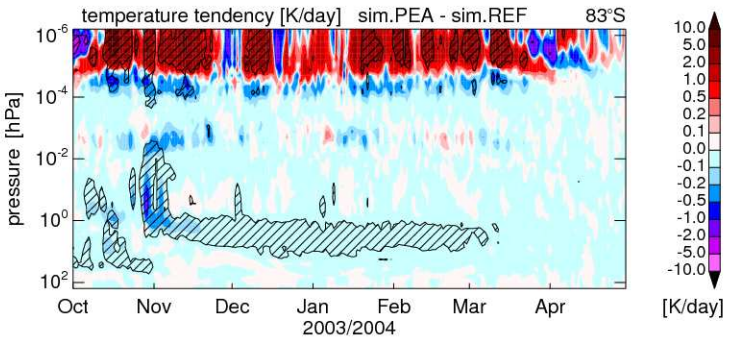

Figure 6.8— Differences of short wave heating rates between simulations PEA and REF indicating the PEP effect on heating by absorption of solar radiation with wave lengths greater than Lyman-α. Shaded areas indicate statistical significance larger than 95%.

that is discussed in section 6.2.1. Further significant temperature effects can be found in the thermosphere where PEPs induce temperature increases of more than 20 K and in certain regions decreases of more than 20 K. These effects are considered in the section after the next.

Temperature response to ozone depletion

Temperature effects of PEP-induced ozone depletion have been pointed out by previous studies (e.g. *Zadorozhny et al.*, 1994; *Krivolutsky et al.*, 2006; *Jackman et al.*, 2007; *Becker and von Savigny*, 2010). Simulations of the Halloween event by *Jackman et al.* (2007) indicate a maximum temperature decrease of 2.6 K in the mesosphere for the 30 October 2003 at 90°S. Figure 6.7 shows a similar PEP-induced temperature decrease in that altitude region of the SH polar cap for the respective time period in late October and early November 2003. At this time period the simulated temperature decrease coincides with the PEP-induced ozone depletion shown by Figure 6.6. In order to verify the hypothesis that a PEP-induced ozone depletion is responsible for the temperature decrease Figure 6.8 shows the PEP-induced temperature effect by heating of absorption of short wave radiation in the southern polar region. Here, radiation of wavelengths greater than Lyman-α is considered. A significant reduction of heating by about 2 K per day in the lower mesosphere during the period of the Halloween storms can be seen. Assuming that ozone is a primary absorber in the considered spectral range in that altitude region, and recognizing the similar pattern of ozone depletion and reductions of short wave heating, it indicates that the temperature decrease is caused by the PEP-induced ozone destruction. Figure 6.7 also indicates significant PEP-induced temperature effects in the southern polar middle atmosphere during the weeks before the Halloween storms. Here, the altitude structure of the temperature effects is very different to that corresponding to the Halloween event. In the mesosphere, the temperature response is positive. A comparison with Figure 6.6 shows that

these temperature changes also correspond to a PEP-induced ozone reduction. Since particle precipitation in that altitude region is weak during the weeks before the Halloween event it is not clear which PEP-induced processes are responsible for the relatively low ozone concentrations. It seems likely that the reduced ozone concentration results from enhanced PEP activity during the preceding winter season, which was simulated but is not shown. A reduction of short wave heating is also apparent in the stratosphere and lower mesosphere during almost the full month of October. But the signal is substantially weaker than that of the Halloween event and therefore, it explains only in part the corresponding temperature effect showing similar temperature changes as those of the Halloween event.
A remarkable warming can be found in the first half of October directly above the region which is assumed to be cooled by PEP-induced ozone depletions. In late October and early November a warming occurs in the upper mesosphere above the pronounced cooling, even though this warming seems to be lesser significant. As indicated by Figure 6.8, these temperature increases are not caused by local PEP-induced changes of the short wave radiative heating. *Jackman et al.* (2007); *Krivolutsky et al.* (2006), and *Becker and von Savigny* (2010) suggest that such temperature increases above the cooling region result from dynamical effects.
As shown in section 6.1.2, the ozone depletion due to particle precipitation in the northern hemisphere is even stronger than in the southern hemisphere. Figure 6.7 does not show any significant temperature effects associated with the Halloween event in the NH middle atmosphere, because solar illumination in the NH polar region is weak or absent during late October and the following months. Therefore, temperature changes due to ozone depletion and the corresponding decrease of absorption of ultraviolet radiation are marginal.
The short wave heating rates (Figure 6.8) reveal significant changes in the thermosphere caused by PEPs. Although in that altitude region short wave solar radiation is the primary energy source, direct radiative heating is thought to provide only a secondary heating source. The main part of photon energy is used to break molecular bonds and hence it is converted to chemically potential energy. The latter is released as thermal energy when dissociation products recombine. The importance of that and other heating and cooling mechanisms in the thermosphere is shown in the following section.

Inter-hemispheric comparison of temperature effects in the thermosphere

The study of temperature effects in the thermosphere considers the time average over November 2003. Therefor, Figure 6.9 shows the effect of particle forcing on temperature as zonal average in geomagnetic coordinates. As indicated by Figure 6.7 a significant temperature increase caused by particle precipitation can be found nearly in the entire thermosphere. This temperature effect strengthens with increasing altitude. Values of more than 20 K are shown for pressure level of about 10^{-6} hPa at high latitudes. Figure 6.9 also confirms the impression of Figure 6.7

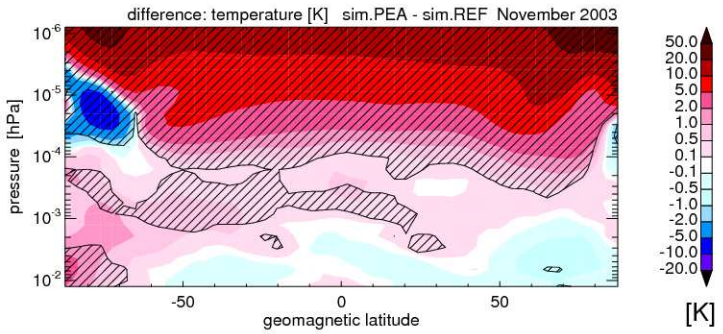

Figure 6.9— Zonal average of the difference between temperatures simulated by PEA and REF averaged over November 2003. Shaded areas indicate statistical significance larger than 95%.

that particle precipitation causes a remarkable temperature decrease in the SH lower polar thermosphere. Causes of this effect are discussed in the following section, while the present section is concerned with an inter-hemispheric comparison of the influence of PEPs on a series of processes affecting the temperatures within the thermosphere. Note that Figure 6.9 shows that nearly in the entire thermosphere PEP-induced temperature effects are of high statistical significance.

Figure 6.10 shows temperature tendencies due to diverse upper atmospheric processes and the influence of PEPs on these quantities for the northern and southern polar upper mesosphere and lower thermosphere. The dominant heating sources in a wide altitude range of the SH polar thermosphere are heating by exothermal chemical reactions (in the following denoted as chemical heating) and Joule heating. In the NH polar thermosphere the heating effect of these mechanisms is also important but substantially smaller than in the SH. The reason for these inter-hemispheric differences is that during the considered time period photolysis is stronger in the sunlit SH atmosphere than in the dark NH polar region. As can be seen in Tables A.16 and A.17, a large part of chemical heating is accomplished by reactions of photolysis products, e.g. O, O(^{1}D), N(^{2}D), and ions. A weaker production of these photolysis products results in less effective chemical heating in the NH polar thermosphere. Stronger Joule heating in the SH can also be explained by higher ion/electron densities in consequence of stronger photo-ionization in the southern polar region which is sunlit during the considered time period (November). A comparison of electron densities between north and south polar region is given in the left panel of Figure 6.11. It should be mentioned that the magnitude of Joule heating is not only determined by the ion/electron density. Since Joule heating is a result of differences of plasma motion relative to the neutral wind, different neutral wind features can also cause inter-hemispheric differences of Joule heating. However, as can be seen in differences of temperature tendencies (see lower panels of Figure 6.10) the PEP effect on Joule heating is much stronger in the NH. This seems surprising since a comparison of PEP-induced ionization rates, which is presented in the right panel of Figure 6.11, indicates that particle precipitation

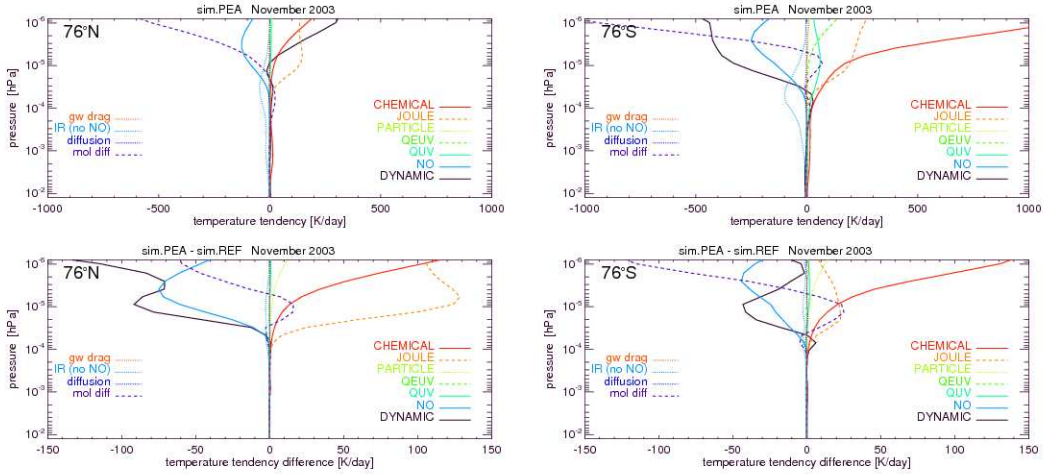

Figure 6.10— Top: PEA simulated temperature tendencies at 76°N (left) and 76°S (right) of geomagnetic latitude averaged over November 2003 in the upper mesosphere and thermosphere for processes providing major contributions to the energy balance. Bottom: Differences of temperature tendencies between simulations PEA and REF. CHEMICAL=chemical heating, JOULE=Joule heating, PARTICLE=direct heating by PEP impact, QEUV=direct heating by EUV photon impact, QUV=heating by UV radiation of wave lengths greater than Lyman-α, NO=nitric oxide cooling, DYNAMIC=dynamical heating, gw drag=heating by gravity wave drag, IR (no NO)=long wave cooling excluding NO cooling, diffusion=temperature effect by turbulent diffusion, mol diff=temperature effect by molecular diffusion.

at 76° is similar in both hemispheres. In comparison with the NH only slightly higher ionization rates appear in the SH. The stronger PEP-induced Joule heating effect in the NH can be explained by the stronger PEP-induced increase of the electron density, which is shown in the central panel of Figure 6.11. Since the PEP-induced ionization rates are comparable in both hemispheres recombination must proceed more rapidly in the summer hemisphere. In contrast to Joule heating the PEP-induced increase of chemical heating is similar in both hemispheres. Assuming that the chemical life time of the involved species is relatively short, this is clear because the chemical potential energy which is converted to thermal energy is originally supplied by the initial PEP impact.

In the thermosphere at 76°N dynamical heating is an important heat source. Here, horizontal and vertical temperature advection and related adiabatic temperature changes are taken into account. The temperature tendency due to dynamical processes is calculated under the assumption that it balances the integral temperature tendency of all other processes. This assumption can be applied since the temperature tendency corresponding to the absolute temperature change over November 2003 is by orders of magnitude smaller than the temperature tendency of dynamical processes.

Heating by absorption of solar UV and EUV radiation plays a secondary role in the polar summer thermosphere, while its effect is negligible in polar winter and hence no influence of PEPs on short wave radiative heating (UV and EUV heating) can

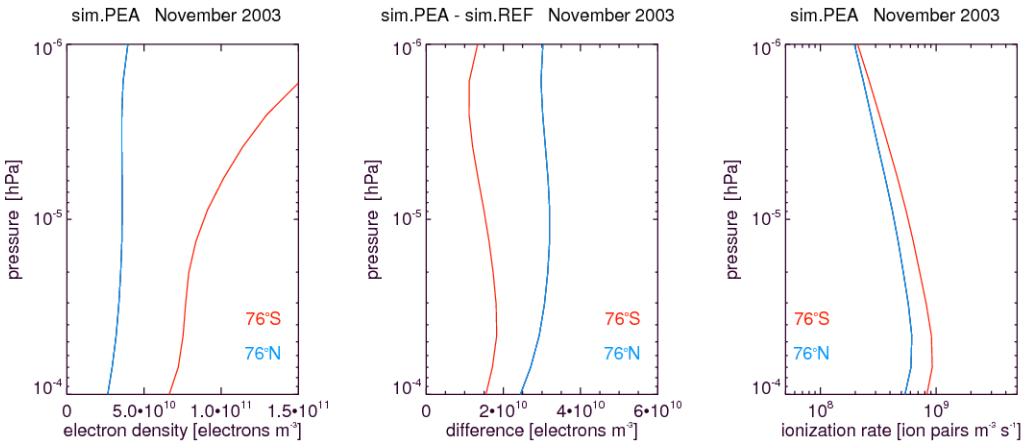

Figure 6.11— Altitude profiles of: (left) electron densities from simulation PEA, (center) electron density differences between simulation PEA and REF, and (right) ionization rates of the complete PEP spectrum. Red curves are associated with at 76°S and blue curves with 76°N.

be seen here. In the summer thermosphere, PEPs cause a slight increase of UV heating. As already mentioned, the contribution of direct solar heating is relatively small. That seems contrary to the results of a HAMMONIA study of *Schmidt et al.* (2006) which indicates that solar heating is the main heating source in the middle and upper atmosphere. The reason for this difference is that in the study of *Schmidt et al.* (2006) the combined temperature effect of direct solar heating and chemical heating is presented, while both effects are separately considered in the present study. Note that chemical heating results from breaking of molecular bonds, ionization, and excitation of diverse atmospheric components by solar photons. Consequently, a large part of incoming solar energy is converted into chemically potential energy which can be released as thermal energy far away from the place of the initial photon impact. The corresponding heating effect is denoted as chemical heating, even though the energy is originally provided by solar photons.
An additional minor warming source is direct heating by transfer of kinetic energy from PEPs to atmospheric atoms and molecules through collisions. This mechanism is denoted as particle heating and explained in section 3.2.2.
The warming is mostly balanced by nitric oxide cooling and molecular diffusion. As shown in section 6.1.1 the NO concentration is strongly influenced by particle precipitation whereby the NO increase in the thermosphere is more effective in winter than in summer. This results in a PEP-induced increase of NO cooling which is substantially stronger in the winter thermosphere. At 76°S dynamical cooling is an important cooling mechanism, which is strengthened by PEP influence. This is discussed in the next paragraph. In the lower thermosphere, long wave emission by NO and other chemical components is an important mechanism balancing the warming effects. It seems usually less affected by PEPs.

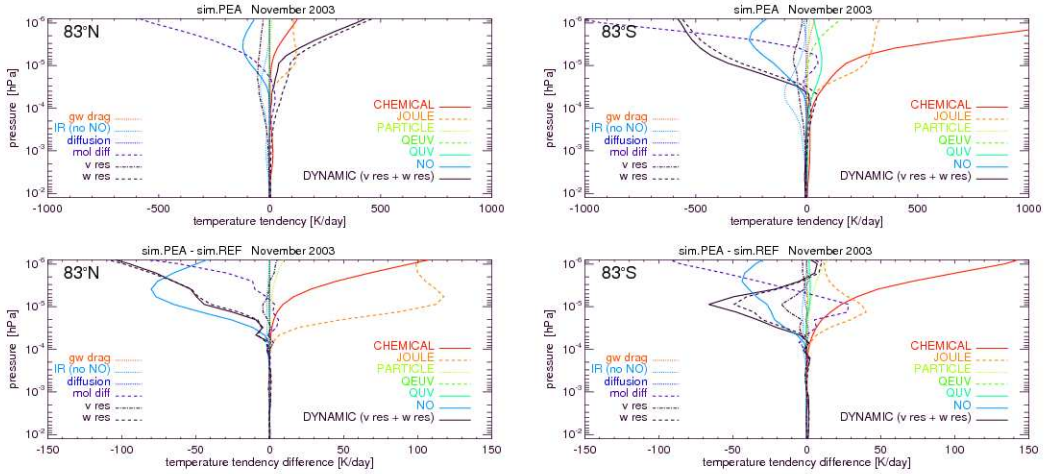

Figure 6.12— The same as Figure 6.10 but at geographic latitudes of 83°N (left) and 83°S (right).

The cooling effect of PEPs in the polar lower thermosphere in summer

As shown in the previous section, in most regions of the thermosphere the integral effect of PEPs is that of a warming. But, as indicated by Figure 6.9, in the lower polar summer thermosphere a region can be found where the atmosphere is cooled by particle influence. Similarly, model simulations by *Krivolutsky et al.* (2006) indicate a temperature decrease in the lower polar summer thermosphere during a solar proton event. The mechanisms responsible for this temperature effect are, however, not discussed by *Krivolutsky et al.* (2006). In the following an attempt for an explanation of this temperature effect is made.

As indicated by Figure 6.10, dynamical processes contribute considerably to that cooling. In order to study the causes heating rates are considered again but in geographic coordinates. The geographic coordinate system seems more convenient to analyze dynamical processes since it allows an easier interpretation of the momentum equations which are usually formulated in geographical coordinates.

Figure 6.12 presents the heating or cooling tendencies of diverse processes and the influence of PEPs on these processes. In contrast to Figure 6.10, which considers quantities at geomagnetic latitudes of 76°N and 76°S, geographic latitudes of 83°N and 83°S are considered here. The curves of the individual processes show similar behavior as at geomagnetic latitudes of 76°N and 76°S, respectively. Additionally, Figure 6.12 shows the individual contributions of the dynamical component. Here, the temperature tendency of dynamical processes and their components are determined using a formulation of the Transformed Eulerian Mean (TEM) analysis given by *Andrews et al.* (1987). It indicates that PEP-induced upwelling, represented by the vertical component of the residual circulation $\overline{w}^*$, is responsible for the prominent temperature decrease in the SH polar lower thermosphere. It must be mentioned that the TEM formulation is applied under the assumption of quasi-geostrophy. It

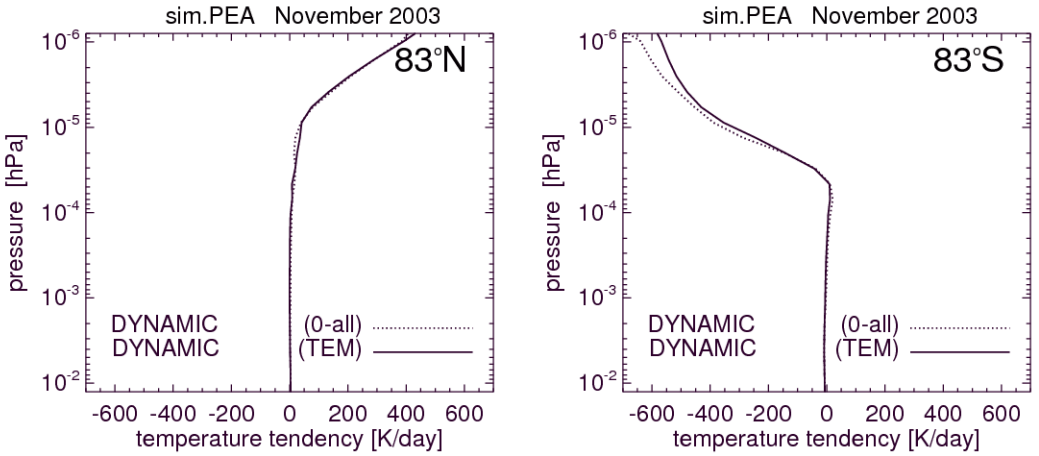

Figure 6.13— Comparison of dynamically induced temperature tendencies in simulation PEA at geographic latitudes of 83°N (left) and 83°S (right). Solid lines are associated with temperature tendency determined by TEM analysis and dotted lines are associated with the dynamical temperature tendency derived under the assumption of balance with temperature tendencies from all other processes. A time mean over November 2003 is considered.

can be expected that this assumption is almost satisfied in a wide range of the atmosphere, but it is thought that it is increasingly not satisfied with increasing altitude in the thermosphere where neutral winds are significantly influenced by dissipative processes. In order to assess the TEM results which are presented in Figure 6.12 the dynamically induced temperature tendency is also derived under the assumption that it balances the sum of all other heating and cooling terms. Figure 6.13 shows a comparison of the dynamically induced temperature tendencies which are on the one hand derived from TEM analysis and on the other hand derived from the assumption of temperature tendency balance. As mentioned in the previous section, this assumption is approximately satisfied. The comparison in Figure 6.13 shows that over wide altitude ranges the total TEM analyzed dynamical temperature effect reflects well the directly modeled effect. Only in the SH thermosphere substantial differences appear, but the qualitative behavior of the dynamically induced temperature effect seems to be well reflected by the TEM analysis.
In order to show that ion drag might be, at least partly, responsible for wind changes resulting in PEP-caused dynamical cooling in the lower polar summer thermosphere, the momentum budget and the so-called "downward control" principle are considered. The latter is formulated by *Haynes et al.* (1991). It means that in the extratropics the mean vertical velocity

$$\overline{w}^*(z_0) = \frac{-1}{\rho(z_0)cos\phi}\frac{\partial}{\partial y}[\frac{cos\phi}{f}\int_z^\infty \rho(z)F(z)dz] \tag{6.7}$$

at any given height (z_0) and consequently the vertical transport is governed by dissipative forcing F above that height. Here, ρ is the air density, f is the Coriolis parameter, and ϕ is the latitude. In the thermosphere dissipative forcing involves ion

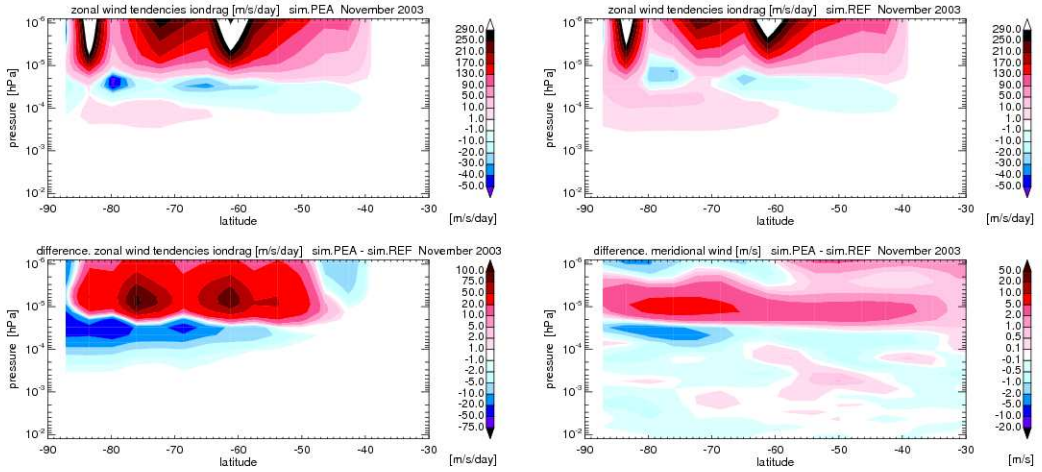

Figure 6.14— The upper panels show the November 2003 monthly zonal mean of the zonal component of the wind tendency due to ion drag from simulation PEA (left) and REF (right). The lower left panel shows the difference between simulation PEA and REF of quantities presented in the upper panels. The lower right panel shows the difference of the meridional wind.

drag. The horizontal wind tendencies are described by the corresponding momentum equations:

$$\frac{\partial u}{\partial t} + u\frac{\partial u}{\partial x} + v\frac{\partial u}{\partial y} + w\frac{\partial u}{\partial z} = \frac{-1}{\rho}\frac{\partial p}{\partial x} + fv + G_x + F_x \tag{6.8}$$

$$\frac{\partial v}{\partial t} + u\frac{\partial v}{\partial x} + v\frac{\partial v}{\partial y} + w\frac{\partial v}{\partial z} = \frac{-1}{\rho}\frac{\partial p}{\partial y} - fu + G_y + F_y, \tag{6.9}$$

where u, v, w are the zonal, meridional, and vertical wind, and G represents the gravitational force. It can be seen that, under the assumption of an equilibrium, a force (e.g. ion drag force) on the zonal wind in combination with the Coriolis force results in a change of the meridional wind. Taking the downward control principle into account, at high southern latitudes an ion drag force acting in eastward direction would lead to an upward motion at polar latitudes below the altitude level where the ion drag is acting. Figure 6.14 shows the PEP-caused influence of ion drag on the zonal wind component and the resulting change of the meridional wind in the middle and high latitude SH thermosphere. A remarkable PEP-induced increase of the eastward ion drag force can be seen above about 10^{-5} hPa in middle and polar southern latitudes. Below that altitude, decreasing eastward or increasing westward ion drag, respectively, is shown. It is also shown that an equatorward tendency of motion results from PEP influence above 10^{-5} hPa. This can be explained by the PEP-induced effect on ion drag and explains an upward motion leading to the found PEP-induced temperature decrease in the lower southern polar thermosphere.

6.2 Contribution of individual particle components

The previous section is concerned with the combined influence of all particle classes on chemical composition and energetics. It is the first study which considers such a comprehensive spectrum of PEPs. A further interesting aspect is concerned with the contributions of individual particle classes. Until today, this aspect is less investigated. The purpose of this section and a main goal of this work is an assessment of the contribution of individual particle classes. At first, the influence of precipitating electrons or α-particles, respectively, is considered in relation to simulations excluding these particle components. Afterwards, the influence of separate particle species on the total amount of NO_x and HO_x is examined.

6.2.1 Contributions of electrons and alpha-particles related to the influence of other PEP components

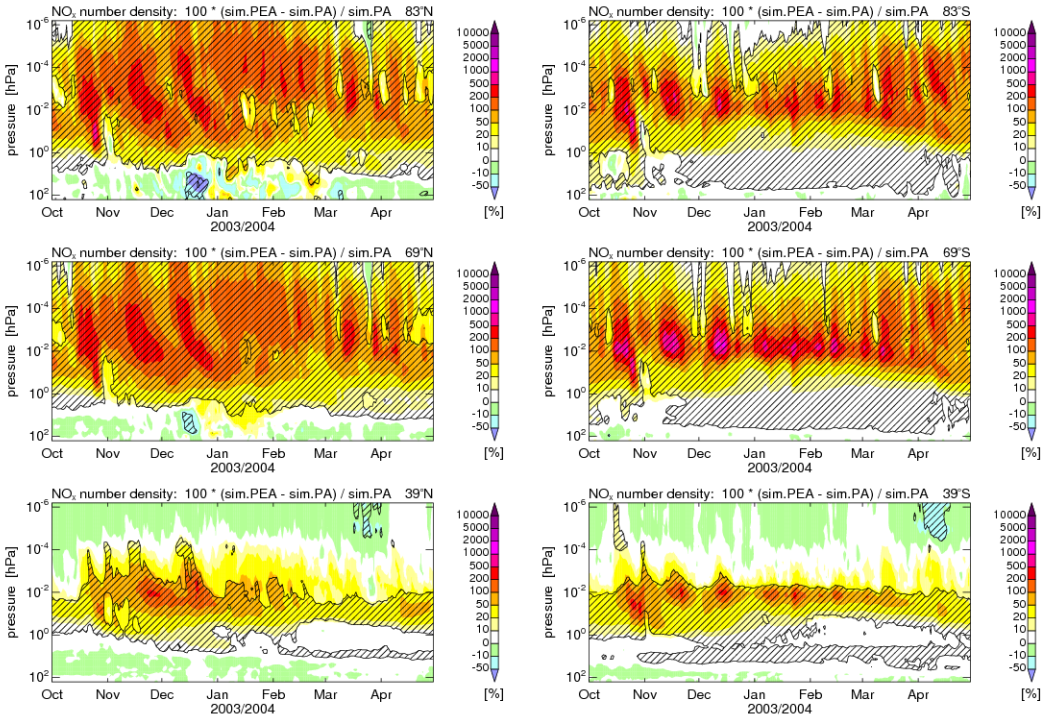

Figure 6.15— Relative differences between NO_x number densities from simulation PEA and simulation PA, indicating errors in simulations which exclude the influence of precipitating electrons. A time period of October 2003-April 2004 and geomagnetic latitudes of 83° (top), 69° (center), and 39° (bottom) for the northern hemisphere (left) and southern hemisphere (right) are considered. Units are percent. Shaded areas indicate statistical significance larger than 95%.

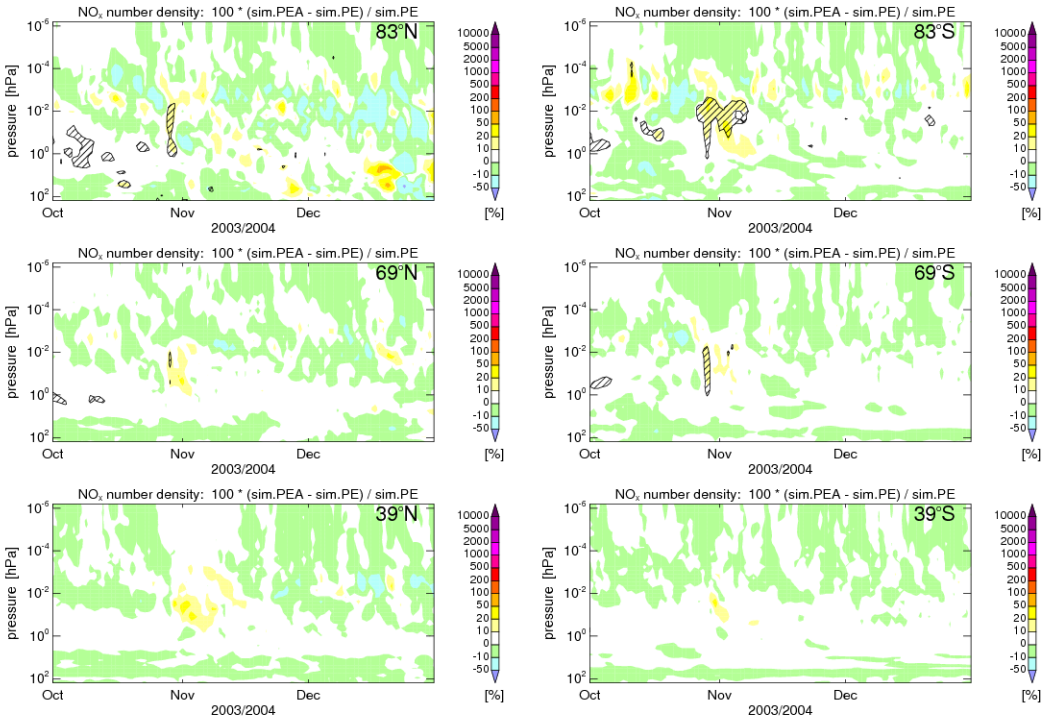

Figure 6.16— Relative differences between NO_x number densities from simulation PEA and simulation PE, indicating errors in simulations which exclude the influence of precipitating α-particles. A time period of October to December 2003 and geomagnetic latitudes of 83° (top), 69° (center), and 39° (bottom) for the northern hemisphere (left) and southern hemisphere (right) are considered. Units are percent. Shaded areas indicate statistical significance larger than 95%.

NO_x and HO_x

In order to study the NO_x change due to electron precipitation, the relative difference between simulations PEA (including the full particle spectrum) and PA (including protons and α-particles) is determined (Figure 6.15). Electrons significantly influence NO_x in a wide altitude range of the auroral and polar regions. Values often exceed 100%, indicating that electrons dominate the NO_x production. Obviously, the relative contribution of electrons is small in the stratosphere and lower mesosphere during the Halloween event in late October and early November. Here, electrons play only a secondary role. The contribution of α-particles (see Figure 6.16) is weak and less significant, in general. Even though considerable precipitation of α-particles occurs during the Halloween event (see Figure 4.3), their effect on NO_x is lower than 20% and strongly limited in duration and space. The reason for the weak influence of α-particles is that their precipitation coincides in time and space with the large proton precipitation event. Note that the calculated values indicate errors in model simulations which exclude the influence of precipitating electrons or α-particles, respectively.

As shown in Figure 6.17, the influence of precipitating electrons on HO_x is weak

in the most regions. This is caused by the fact that PEPs primarily form HO_x in the middle atmosphere, while electron precipitation mainly occurs above this altitude range. However, a substantial influence of electrons on the HO_x density can be found in the lower mesosphere and upper stratosphere of the northern polar cap region. Noteworthy are electron-induced HO_x increases during two pronounced particle events surrounding the proton-dominated major event of the Halloween storms. Here, precipitating electrons are responsible for prominent PEP-induced enhancements of the HO_x concentration. In the subsequent time period the relatively large electron activity leads to relatively strong HO_x enhancements, but the absolute effect is rather small as revealed by comparison with Figure 6.3. In the summer polar stratopause region HO_x is mainly produced by the influence of solar radiation. Here, the absolute HO_x concentrations are significantly higher than in the winter polar region, but as shown by Figure 6.4 the relative PEP influence on HO_x is small. Hence, the relative electron influence is also small.

Only marginal effects of α-particles on HO_x are indicated by Figure 6.18, even

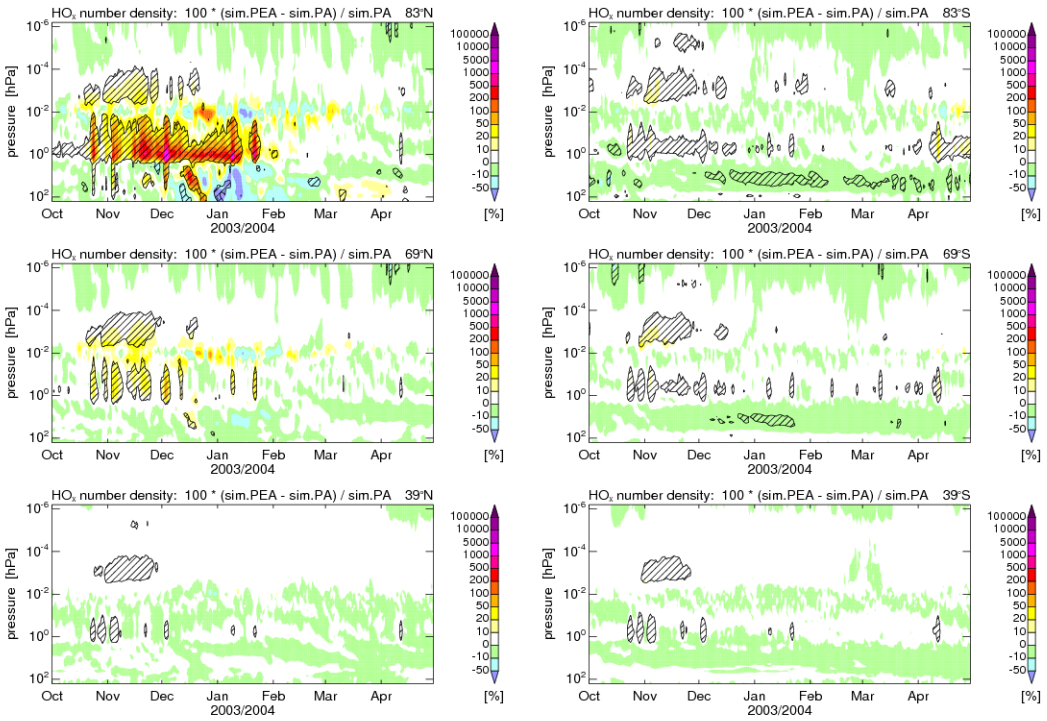

Figure 6.17— Relative differences between HO_x number densities from simulation PEA and simulation PA, indicating errors in simulations which exclude the influence of precipitating electrons. A time period of October 2003-April 2004 and geomagnetic latitudes of 83° (top), 69° (center), and 39° (bottom) for the northern hemisphere (left) and southern hemisphere (right) are considered. Units are percent. Shaded areas indicate statistical significance larger than 95%.

though, a statistically significant HO_x increase during the major Halloween event is caused by α-particles. But the relative contribution is lower than 10%. A stronger α-particle-induced HO_x increase is indicated in November and December in a small

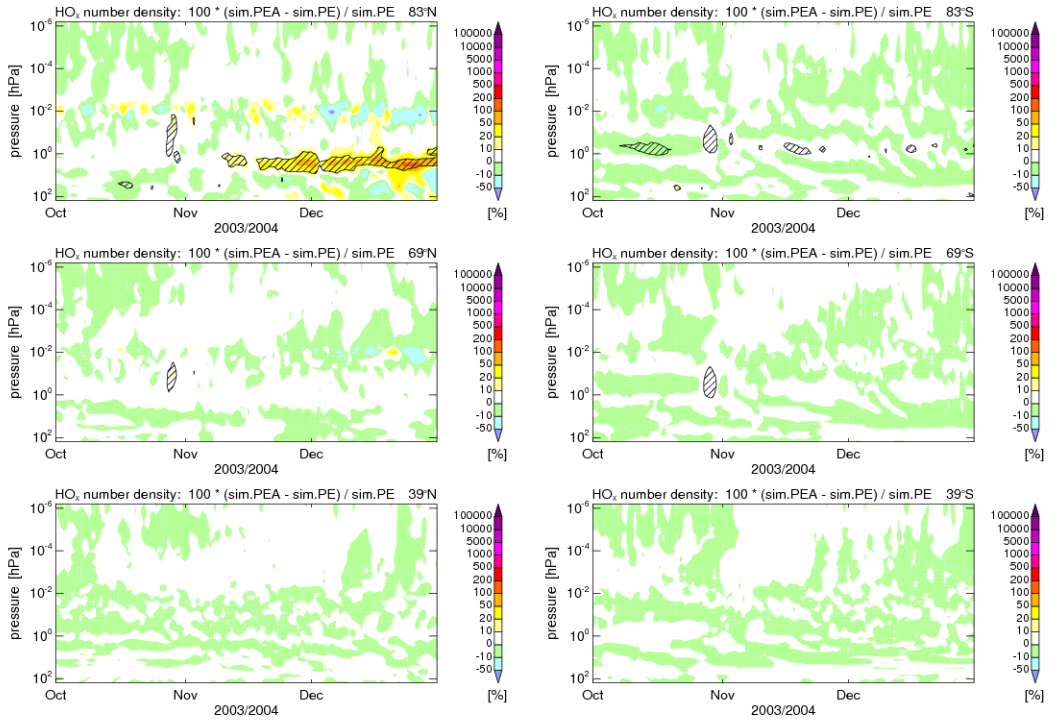

Figure 6.18— Relative differences between HO_x number densities from simulation PEA and simulation PE, indicating errors in simulations which exclude the influence of precipitating α-particles. A time period of October to December 2003 and geomagnetic latitudes of 83° (top), 69° (center), and 39° (bottom) for the northern hemisphere (left) and southern hemisphere (right) are considered. Units are percent. Shaded areas indicate statistical significance larger than 95%.

altitude range within the northern polar stratosphere. However, the absolute effect is weak since HO_x concentrations are low in the stratosphere during that season.

Ozone

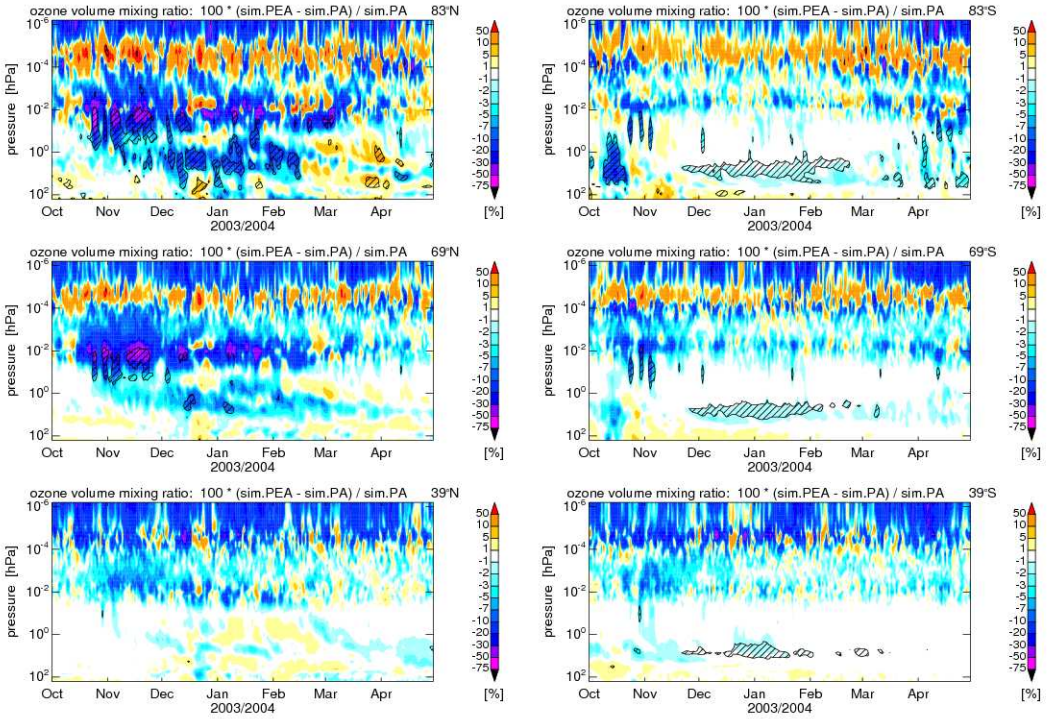

Figure 6.19— Relative differences between ozone volume mixing ratios from simulation PEA and simulation PA, indicating errors in simulations which exclude the influence of precipitating electrons. A time period of October 2003-April 2004 and geomagnetic latitudes of 83° (top), 69° (center), and 39° (bottom) for the northern hemisphere (left) and southern hemisphere (right) are considered. Units are percent. Shaded areas indicate statistical significance larger than 95%.

The electron-induced NO_x and HO_x increase leads to a change of the ozone concentration. The change relative to the concentration in simulation PA is shown in Figure 6.19. While at middle latitudes the influence of electrons on ozone is marginal, at auroral and polar latitudes precipitation of electrons causes substantial changes of the ozone content. In both hemispheres significant electron-induced short term ozone depletions occur during the Halloween event and two additional events occurring a few days before and past the major event. In the lower mesosphere electrons are responsible for short-term ozone depletions accounting 10 to 30% and in the NH temporarily more than 50%. During the following months in the southern stratosphere electrons cause a statistically significant ozone depletion but its contribution is lower than 5%. In the northern polar stratosphere the relative contribution of electrons on long-term ozone depletion is substantially stronger. The influence of α-particles on ozone is usually marginal (see Figure 6.20), although an exception can be found in the SH polar stratosphere in October. Here, α-particles provide a significant contribution to PEP-induced ozone reduction. This ozone reduction is not accompanied by a significant α-particle-induced NO_x or HO_x

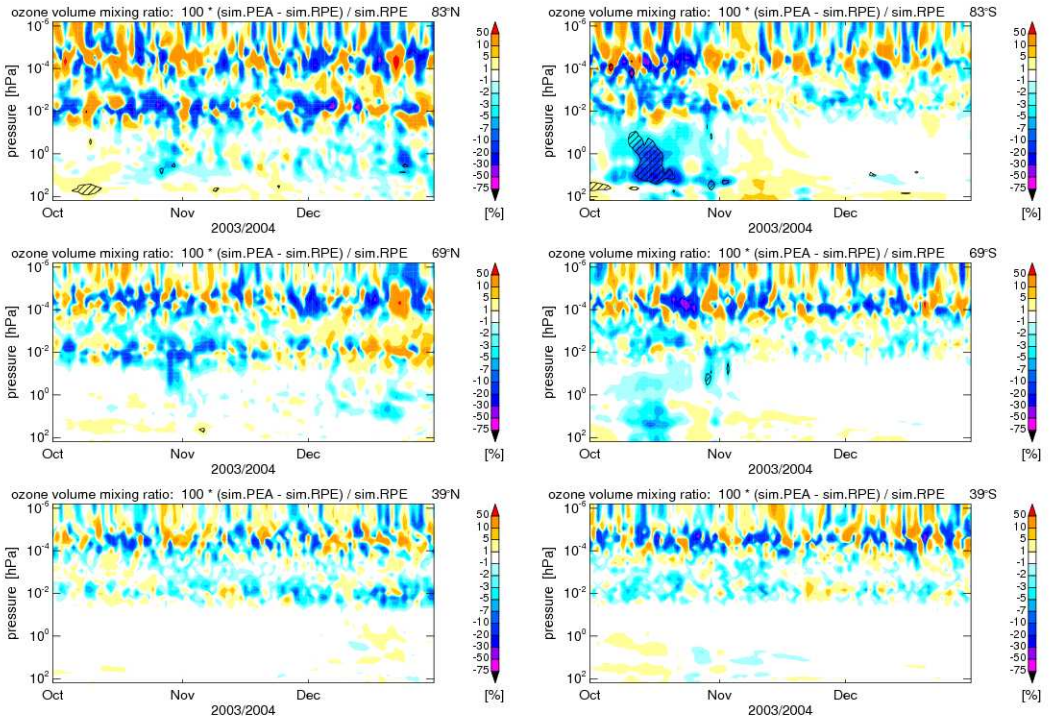

Figure 6.20— Relative differences between ozone volume mixing ratios from simulation PEA and simulation PE, indicating errors in simulations which exclude the influence of precipitating α-particles. A time period of October to December 2003 and geomagnetic latitudes of 83° (top), 69° (center), and 39° (bottom) for the northern hemisphere (left) and southern hemisphere (right) are considered. Units are percent. Shaded areas indicate statistical significance larger than 95%.

increase. Probably, the reduced ozone concentration might be caused by α-particle precipitation during the preceding winter season.

Temperature

In order to study temperature effects which are caused by precipitating electrons, temperature differences between simulation PEA and simulation PA are determined (see Figure 6.21). As indicated by a comparison with Figure 6.7 in the thermosphere the temperature effect of precipitating electrons is similar to that of the complete PEP inventory. This similarity between the effects of electrons and the complete PEP spectrum in the thermosphere is expected since electrons are thought to be usually the dominating PEP species at these altitudes. But electrons cause significant temperature changes in the middle atmosphere as well. On the one hand, temperature effects can be found at high latitudes of the SH in October and November 2003. Here, electrons contribute significantly to the temperature changes due to PEP-induced ozone reduction discussed in section 6.1.4. In late October and November 2003 in the lower mesosphere and upper stratosphere electrons cause a

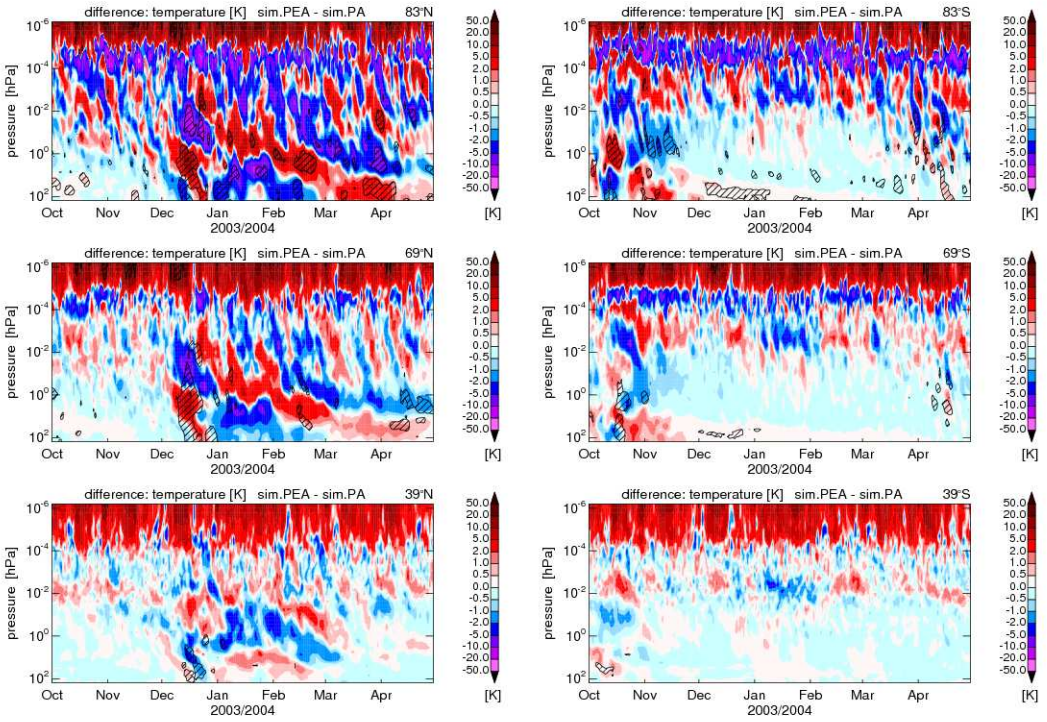

Figure 6.21— Differences between temperatures from simulation PEA and simulation PA, indicating the influence of precipitating electrons. The time period of October 2003 to April 2004 and geographic latitudes of 83° (top), 69° (center), and 39° (bottom) for the northern hemisphere (left) and southern hemisphere (right) are considered. Units are Kelvin. Shaded areas indicate statistical significance larger than 95%.

temperature decrease of more than 1 K. On the other hand, significant temperature effects caused by electrons are found in the NH polar middle atmosphere starting in December.

In order to examine the temperature effects in the northern polar region, the time evolution of the temperature of all ensemble members of simulations PEA and PA at 83°N and four pressure levels representing stratospheric, mesospheric, and thermospheric altitudes are considered (see Figure 6.22). Additionally, Figure 6.22 shows the time evolution of temperatures of simulation REF. Considering the middle atmosphere, noticeable features are the rapid temperature increase in the stratosphere and a decrease in the mesosphere, suddenly occurring in December. These features are more or less reflected by each ensemble member of all simulations. The temperature increase at 10 hPa indicates a sudden stratospheric warming (SSW) event. Such an event is characterized by a downward displacement of the stratopause. For further details on SSW events see *Charlton and Polvani* (2007) and references therein. While, before this abrupt temperature change the spread of the ensemble members is relatively small, afterwards a wide spread between the individual ensemble members can be found accompanied by remarkable variability in temperature. Nevertheless, directly after the initial temperature increase in

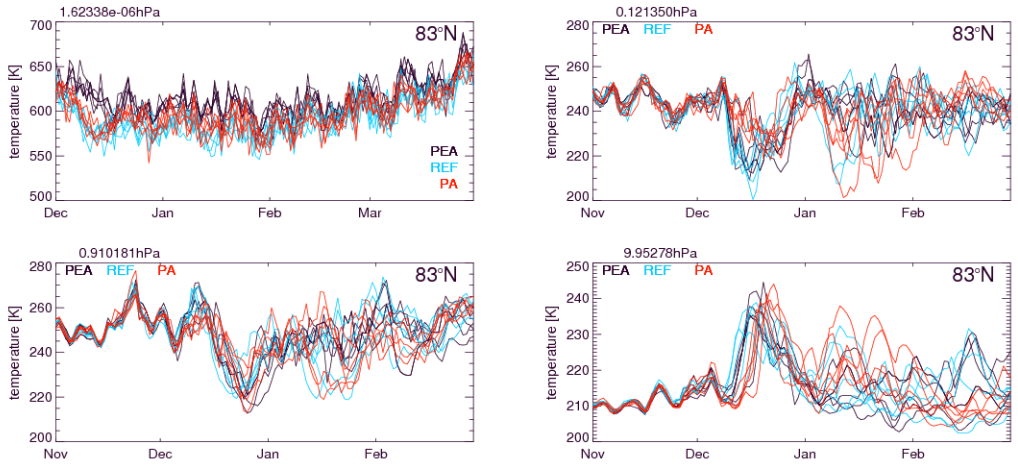

Figure 6.22— Time evolution of modeled temperatures for all ensemble members of simulations PEA (black), REF (cyan), and PA (red) at 83°N. Temperatures are presented for four altitude regions: thermosphere at $\approx 1.6 \cdot 10^{-6}$ hPa (top, left), lower mesosphere at $\approx 1.2 \cdot 10^{-1}$ hPa (top, right), stratopause region at ≈0.9 hPa (top, right), and stratosphere at ≈10 hPa (bottom). The time range is from November 2003 to February 2004.

the stratosphere and drop in the mesosphere all simulations show a temperature decrease in the stratosphere and an increase in the mesosphere. An interesting feature is that, in contrast to the thermosphere, in the middle atmosphere the curves representing simulations PEA and REF show similar behavior, while the ensemble members of simulation PA tends to distinguish from the former. This can be seen in the mesosphere in the middle of December where the temperature drop in simulation PA is significantly weaker and slower than in the other simulations. Simultaneously, the temperature increase at 10 hPa in simulation PA appears with a time lag of several days in comparison with the other simulations. This behavior of the simulation excluding electron precipitation seems surprising. Assuming, as done in previous studies, that the precipitation of electrons and their effects on the middle atmosphere are small one would expect temperatures of simulation PA to be similar to temperatures of simulation PEA. Assuming that the influence of precipitating protons and α-particles is weak some weeks after the solar PEP event, the temperature evolution should be similar in simulation PA and REF. Surprisingly, Figure 6.22 indicates similar behavior of temperatures in simulations PEA and REF, while the temperature in simulation PA tends, at least temporarily, to differ significantly from temperatures in other simulations. The causes of such a behavior are unclear but it indicates that non-linearities appear when individual particle components act together. It shows impressively the importance of considering precipitating electrons in addition to protons and α-particles in regard to middle atmospheric processes. It must be noted that each simulation consists of only five ensemble members. Thus, although the curves in Figure 6.22 show a clear trend, uncertainties remain concerning the statistical relevance of the results.

6.2.2 Contribution of single PEP species relative to total amounts of NO_x and HO_x

In section 6.2.1 the influence of precipitating electrons and α-particles relative to the influence of other particle components is discussed. In the present section the study is focused on the question of the contribution of single particle components on the total amount of NO_x and HO_x. The individual contributions of single PEP components to the total number density of NO_x at different geomagnetic latitudes is shown by Figures 6.23 to 6.28. Note that the contributions of electrons and α-particles are determined as follows: percentage contribution of electrons=100·(PEA-PA)/PEA, percentage contribution of α-particles=100·(PEA-PE)/PEA. Since no simulation exists which only considers precipitating electrons and α-particles, the contribution of protons is calculated as follows: contribution of protons=100·([PEA-REF]/PEA-([PEA-PA]+[PEA-PE])/PEA).
At first, the contribution of precipitating electrons to the NO_x concentration is considered. Particularly in the mesosphere of auroral and polar latitudes this particle species contributes substantially to the NO_x concentration (see Figures 6.23, 6.24, 6.25, and 6.26). Here, the contribution of electrons often exceeds 50%. At times values of up to 90% can be found. Noteworthy is the substantial contribution of 40 to 70% in the mesosphere at mid-latitudes (see Figures 6.27 and 6.28) where usually particle precipitation is relatively weak. In the winter thermosphere at polar and auroral latitudes precipitating electrons dominate the influence on NO_x, while in the mid-latitude thermosphere and in the entire thermosphere in summer the contribution of electrons exceeds values of 50% only occasionally. In the stratosphere the contribution of precipitating electrons on NO_x is mostly lower than 20% with the exception of the upper stratosphere during the weeks after the Halloween storms when the contribution of electrons is greater than 20% at places. While the contribution of precipitating protons on NO_x concentration is usually below 20%, during a few weeks after the Halloween event their contribution temporarily exceeds 50% in the upper stratosphere and 90% in the mesosphere. Moreover, it seems that electron precipitation leads to a substantial NO_x decrease in the auroral and polar NH stratosphere in December 2003, while protons counteract the electron effect. The mechanism which causes this effect is not understood but it indicates non-linearities in the combined influence of several particle components. In general, the contribution of α-particles is lower than 10%. Only during the Halloween event it is elevated up to 20% in some regions.
The consideration of the single contributions of PEP species on NO_x shows impressively the importance of precipitating electrons. In contrast to the proton contribution, which dominates only during a few weeks after the Halloween particle event in a relatively small latitude and altitude range, the influence of precipitating electrons considerably contributes to NO_x concentration over wide ranges of altitude, latitude, and time.

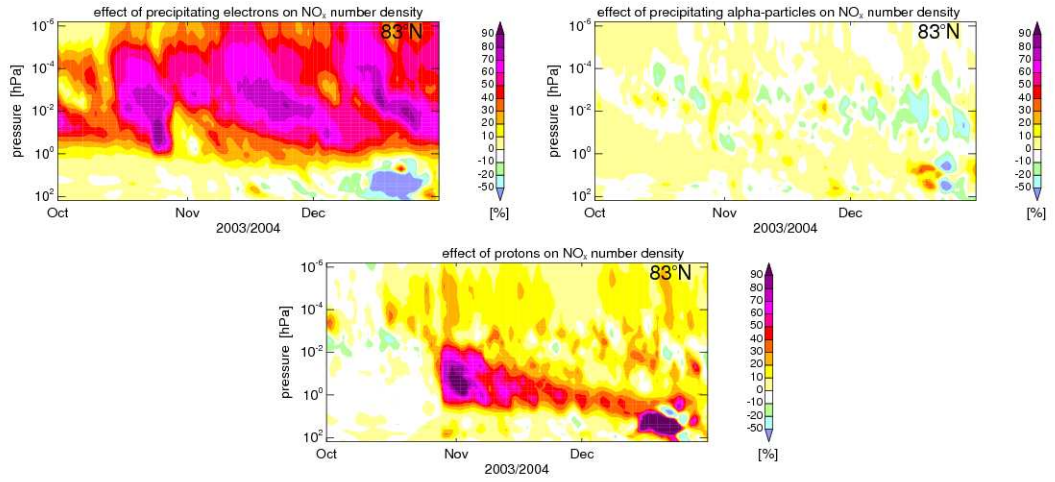

Figure 6.23— Relative contribution of precipitating electrons (upper left panel), α-particles (upper right panel), and protons (lower panel) to the total NO_x number density. The period of October 2003-December 2003 and geomagnetic latitudes of 83°N are considered. Units are percent.

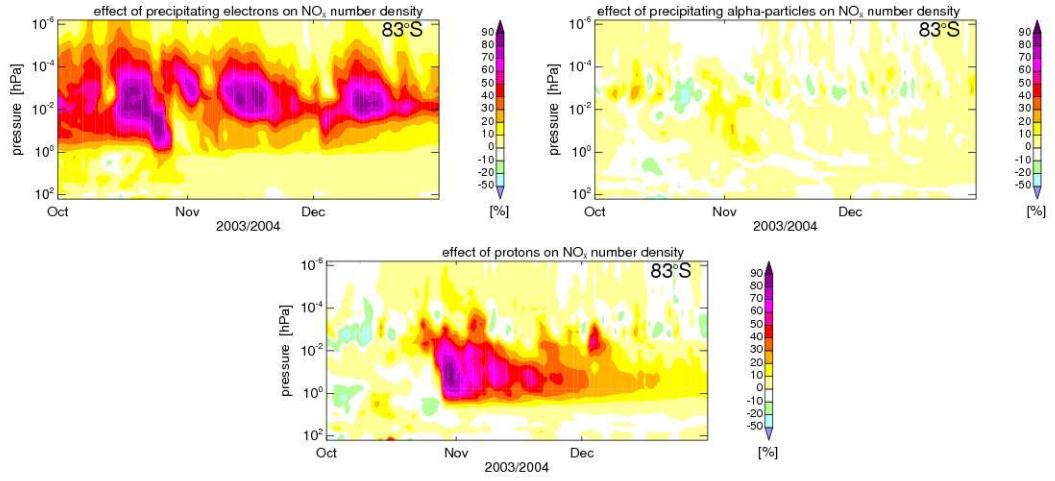

Figure 6.24— The same as in Figure 6.23 but at geomagnetic latitudes of 83°S.

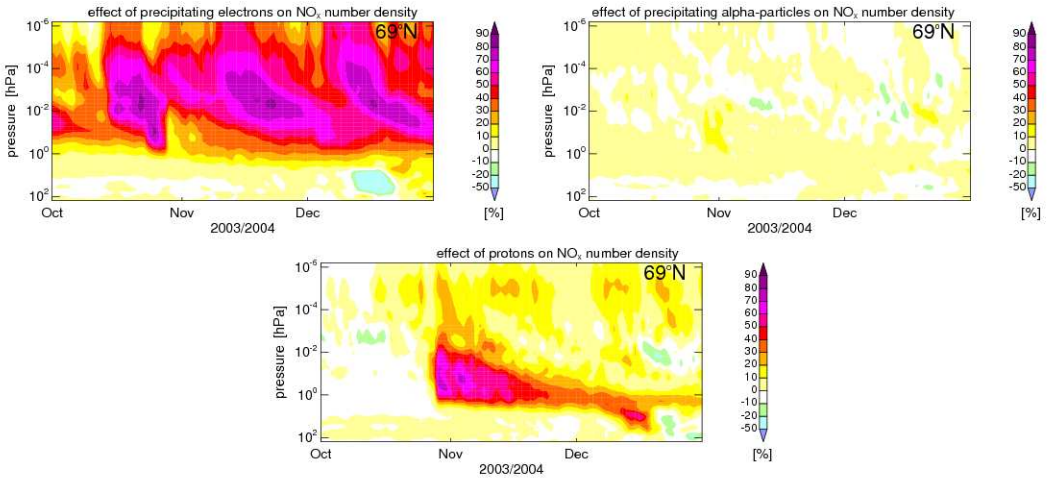

Figure 6.25— The same as in Figure 6.23 but at geomagnetic latitudes of 69°N.

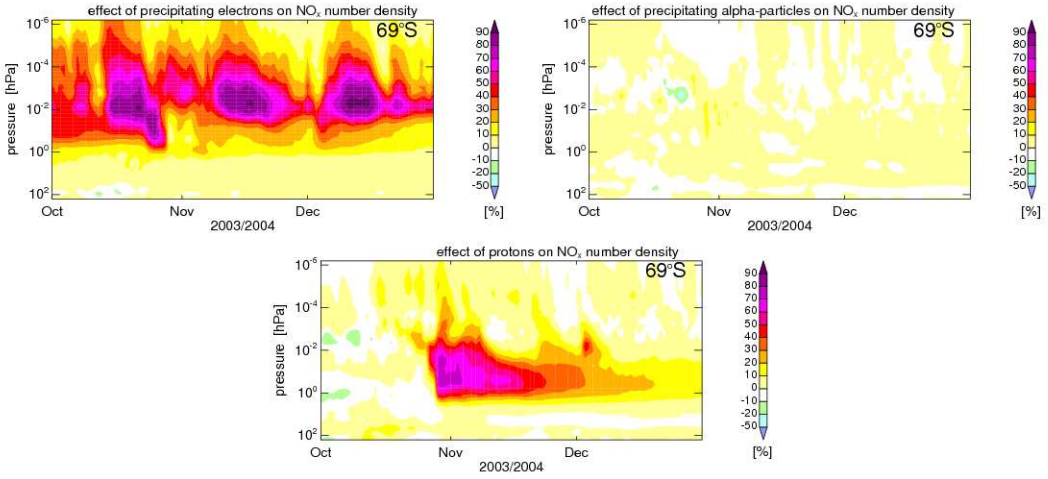

Figure 6.26— The same as in Figure 6.23 but at geomagnetic latitudes of 69°S.

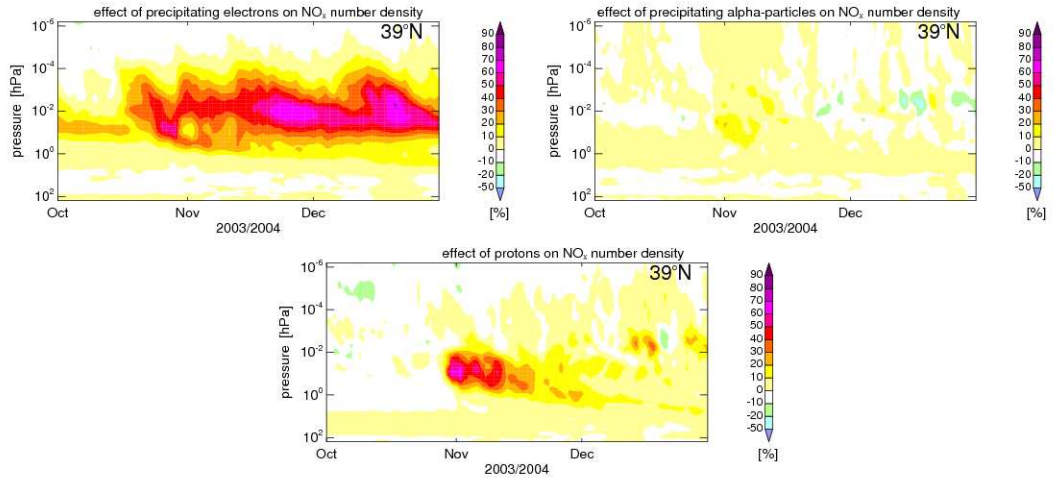

Figure 6.27— The same as in Figure 6.23 but at geomagnetic latitudes of 39°N.

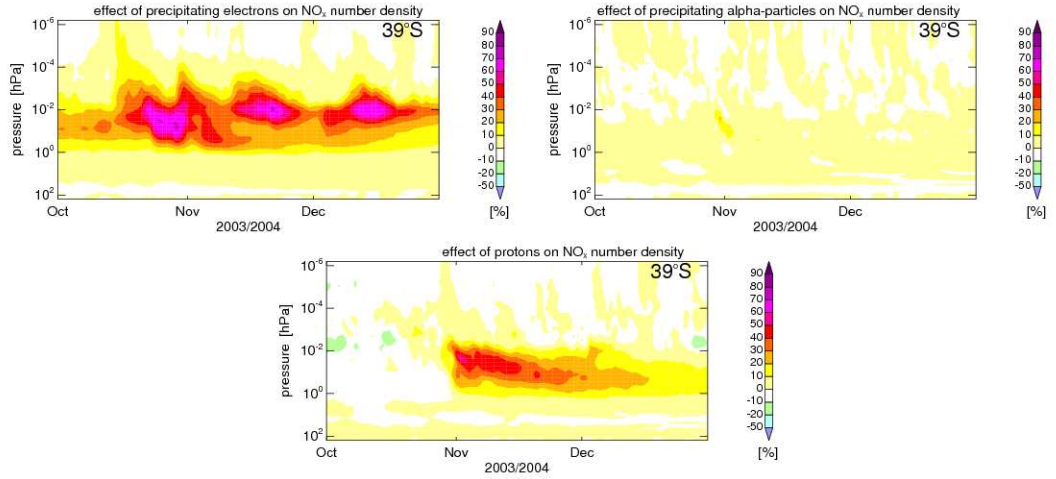

Figure 6.28— The same as in Figure 6.23 but at geomagnetic latitudes of 39°S. Units are percent.

The individual contributions of single PEP components to the total number density of HO_x are presented by Figures 6.29 to 6.34. As mentioned in section 6.1.1 the HO_x production in the sunlit atmosphere is controlled by solar irradiance. Therefore, the contributions of individual particle classes remarkably distinguish from those of NO_x. In the sunlit atmosphere the PEP contributions to HO_x concentration are generally small. Only during the prominent particle precipitation event a short-term contribution of protons amounts up to 40% of the total HO_x number density in the mesosphere at high latitudes. Particle contribution on HO_x is also small at middle latitudes in the northern hemisphere. In the stratopause region at NH polar latitudes the HO_x concentration is strongly controlled by precipitating electrons. Significant contributions of protons are confined to a few events in late

October and early November 2003 and to the stratosphere in the following weeks. Statistical significances of the results can be taken from relative difference plots in section 6.2.1. It must be mentioned that the contributions of individual particle species are derived from differences between simulations considering combinations of different particle components. Previous examinations in this work indicate that between the effects of individual particle components non-linearities appear. That might limit the significance of the results presented in this section.

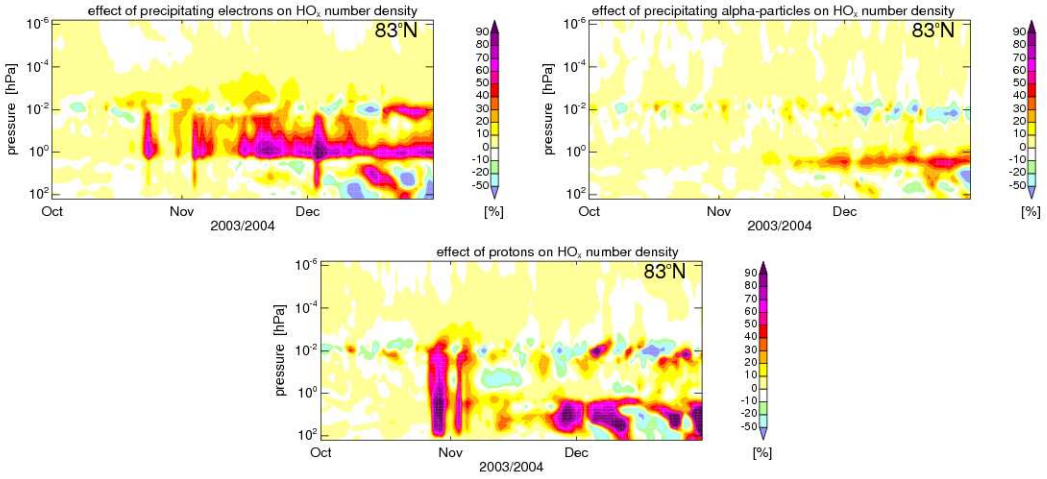

Figure 6.29— Relative contribution of precipitating electrons (upper left panel), α-particles (upper right panel), and protons (lower panel) to the total HO_x number density. The period of October 2003-December 2003 and geomagnetic latitudes of 83°N are considered. Units are percent.

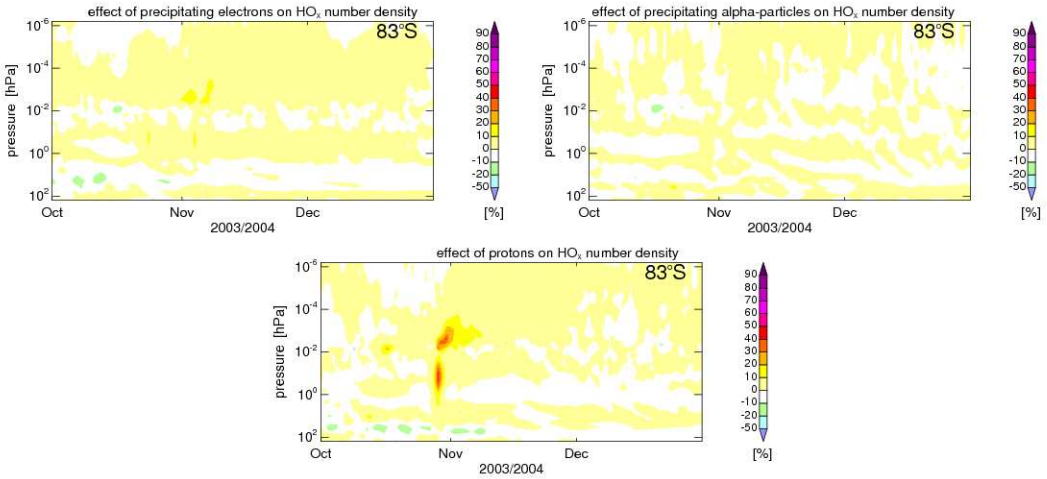

Figure 6.30— The same as in Figure 6.29 but at geomagnetic latitudes of 83°S.

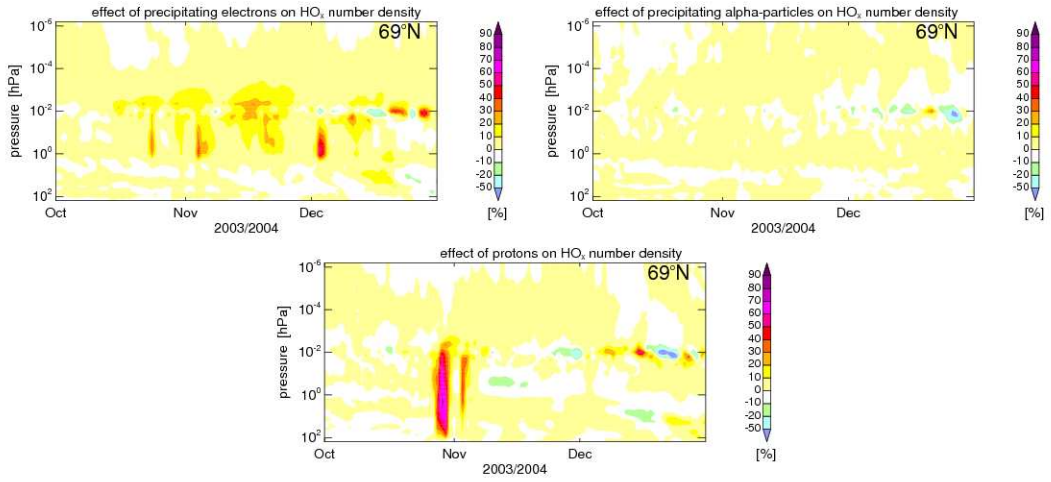

Figure 6.31— The same as in Figure 6.29 but at geomagnetic latitudes of 69°N.

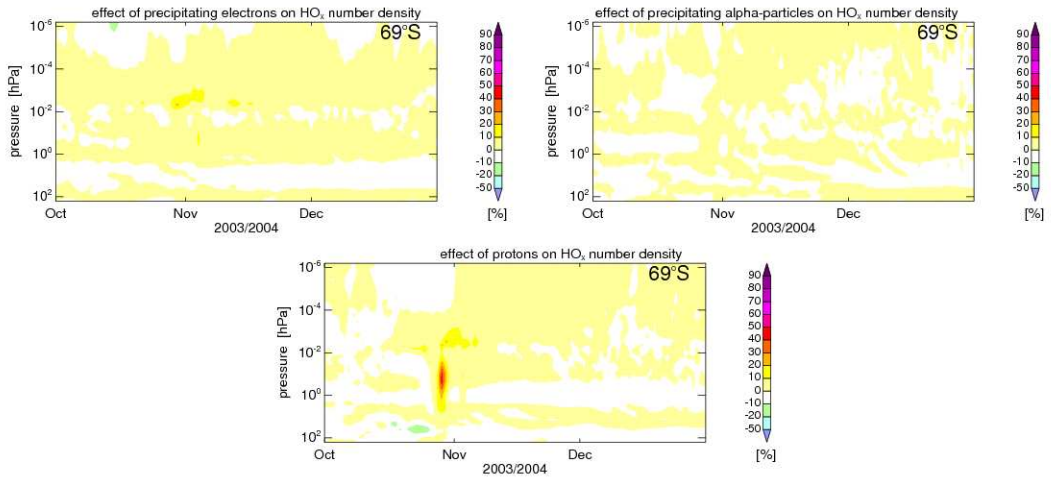

Figure 6.32— The same as in Figure 6.29 but at geomagnetic latitudes of 69°S.

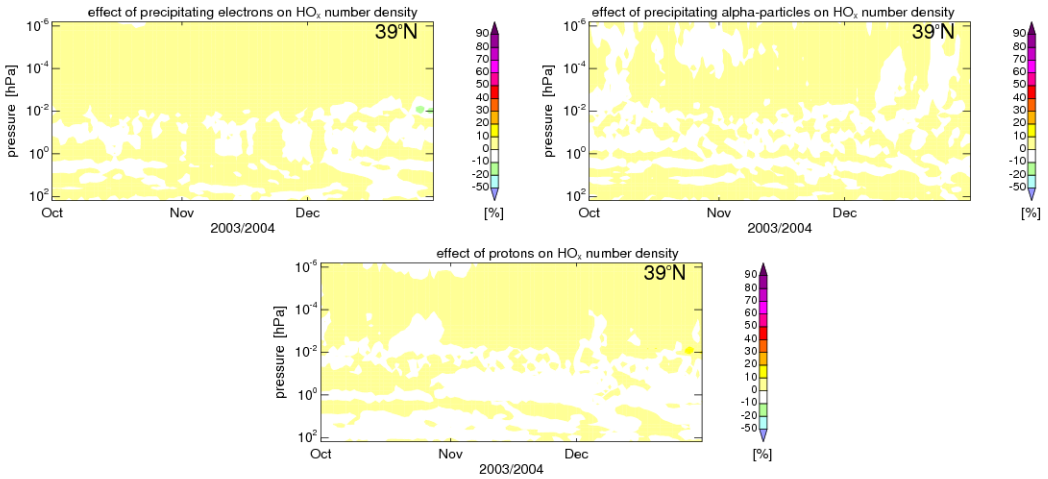

Figure 6.33— The same as in Figure 6.29 but at geomagnetic latitudes of 39°N.

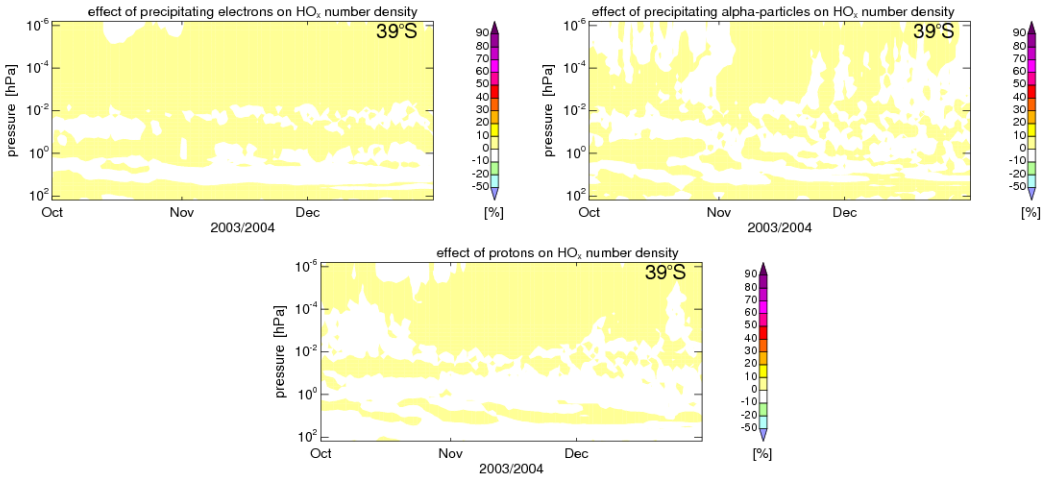

Figure 6.34— The same as in Figure 6.29 but at geomagnetic latitudes of 39°S.

6.3 Downward transport of NO_x

In section 6.1.1 a remarkable NO_x increase in the northern auroral and particularly in the polar mesosphere in December and January was shown (see Figure 6.1). It is also indicated that PEPs are responsible for that NO_x increase, which is accompanied by a remarkably displaced stratopause level in the polar cap. However, a comparison with Figures 4.1 to 4.3 indicates that this NO_x increase is not accompanied by enhanced PEP-induced ionization rates. Causes of this NO_x increase are discussed in the present section. In order to study the mechanisms responsible for the strange NO_x increase, only one ensemble member of simulations PEA is consid-

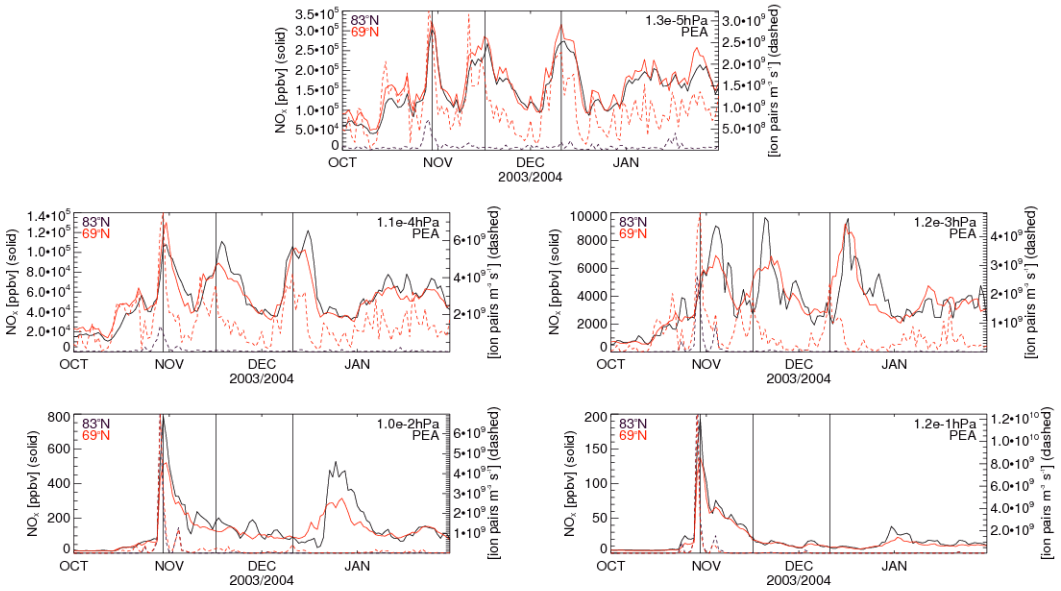

Figure 6.35— NO_x volume mixing ratio (solid) and ionization rates (dashed) at geomagnetic latitudes of 83°N (black curves) and 69°N (red curves) taken from a single ensemble member of simulation PEA. Values are presented for the following five pressure levels of the lower thermosphere and mesosphere: $1.3{\cdot}10^{-5}$ hPa, $1.1{\cdot}10^{-4}$ hPa, $1.2{\cdot}10^{-3}$ hPa, $1.0{\cdot}10^{-2}$ hPa, and $1.2{\cdot}10^{-1}$ hPa.

ered. This is done since the NO_x increase is assumed to be caused by dynamical effects which might be blurred if the mean of five ensemble members is considered. Figure 6.35 shows the NO_x volume mixing ratio and PEP-induced ionization rate for the corresponding time period at northern polar and auroral latitudes and for given altitudes of the thermosphere and mesosphere. Three pronounced NO_x peaks within the thermosphere in the time period from October to December 2003 are revealed. They are already examined in section 5.1. At $1.3{\cdot}10^{-5}$ hPa high NO_x values are accompanied by strong ionization events. The corresponding dates are marked by vertical lines. While the ionization rate maxima occur nearly simultaneously at all thermospheric altitudes, peaks of the NO_x time series indicate a time

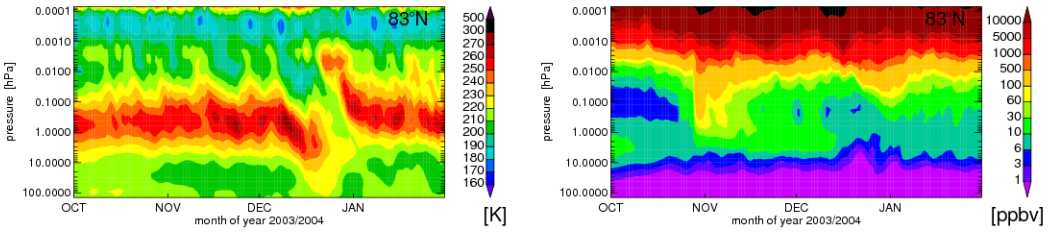

Figure 6.36— Pressure versus time cross section of the temperature (left) and NO_x volume mixing ratio (right) for a four months time period including a SSW event. Values are taken from a single ensemble member of simulation PEA.

lag which increases with decreasing altitude. At $1.2{\cdot}10^{-3}$ hPa the time lag amounts already to several days. At 10^{-2} hPa, located within the mesosphere, ionization rates as well as NO_x mixing ratio show a basically different behavior than in the thermosphere. Instead of the three ionization rate events of the thermosphere only one extreme event can be found in the mesosphere, the main Halloween event. As revealed by detailed examination of the ionization rates (see section 4.2), in the mesosphere ionization during that event is dominated by protons. Here the strong NO_x increase occurs instantly after the ionization peak. At 10^{-2} hPa an additional NO_x maximum occurs without a corresponding increase of PEP-induced ionization. With a time lag of several days the NO_x maximum can be seen at $1.2{\cdot}10^{-1}$ hPa, though it has a less sharp peak. The absence of a corresponding ionization event and the remarkable time lag which increases with decreasing altitude indicate that a significant amount of NO_x is transported downward. During this time period a considerable anomaly of the stratopause occurs (see Figure 6.1). Figure 6.36 shows the temperature evolution at 83°N for the early winter season. It can clearly be seen that the height of the stratopause, defined as the first temperature maximum above the troposphere, substantially decreases in December followed by a displacement to substantially higher altitudes. Subsequently, the stratopause propagates downward arriving at the original altitude level after several days. The initial descent of the stratopause is associated with a substantial temperature drop in the mesosphere. This temperature anomaly is related to a simulated SSW event. As shown by recent observations, strong NO_x descent inside of the polar vortex can occur in conjunction with a SSW event resulting in a substantial increase of the mesospheric and upper stratospheric NO_x concentration (e.g. *Randall et al.*, 2009). The time evolution of the NO_x volume mixing ratio exhibits an NO_x increase in the mesosphere (see Figure 6.36). As revealed by observations, a strong temperature anomaly was observed in the mesosphere and stratosphere in the NH winter 2003/2004 accompanied by remarkable NO_x descent (e.g. *Randall et al.*, 2006, 2009; *Reddmann et al.*, 2010). MIPAS observations show a sudden stratospheric warming in late December 2003 followed by a two month period of extremely low mesospheric temperatures (*Reddmann et al.*, 2010). While the SSW event is well reflected in the simulation, observations show a much slower recovery of the stratopause.

Even though HAMMONIA simulations indicate a significant NO_x enhancement due to downward transport in the northern polar mesosphere, in comparison with measurements the resulting NO_x concentration is significantly underestimated in HAMMONIA. A possible reason is the rapid recovery of the middle atmosphere towards normal conditions associated with a weakening of the polar vortex in early January. This might reduce the effectivity of the modeled downward transport of NO_x. As pointed out by *Siskind et al.* (2007) an unusually warm and disturbed lower stratosphere, as can be found during an SSW, filters out gravity waves that normally break at the stratopause or above it. Consequently, the mesosphere cools down and the polar vortex strengthens. HAMMONIA uses a gravity wave drag parameterization of *Hines* (1997a,b). Possibly, this parameterization does not correctly reflect the effects of the SSW and therefore cause the immediate recovery of the stratopause.

Additionally, underestimated NO_x downward transport might be a result of overestimated horizontal redistribution due to numerical diffusion or overestimated planetary wave activity in the model. Horizontal mixing can bring NO_x-rich air from the polar night to sunlit latitudes where NO_x is photolytically destroyed. The HEPPA study of *Funke et al.* (2011), which is described in section 6.1.3, indicates an overestimation of horizontal mixing in HAMMONIA. These results are also confirmed by studies of *Possner* (2011) which investigate horizontal transport in ECHAM6 (a model which uses similar dynamical core like HAMMONIA) using different horizontal resolutions. This study indicates that horizontal transport is increasingly overestimated with decreasing horizontal resolution of the model.
Although it is thought that HAMMONIA underestimates the strength of NO_x descent, simulations show a significant increase of NO_x in the middle atmosphere in consequence of downward transport of NO_x from the upper atmosphere. At least in the mesosphere, the resulting NO_x concentration substantially exceeds that remaining from the Halloween event. The findings of section 6.2 show that the NO_x concentration in the upper atmosphere, at least in winter, is controlled by the influence of precipitating electrons which primarily originate from the magnetosphere. This arises the importance of inclusion of magnetospheric electron precipitation in studies of mid- and long-term effects of PEP-events on chemical composition of the middle atmosphere.

Chapter 7

Summary, Conclusions, and Outlook

7.1 Summary and Conclusions

Simulations with the general circulation and chemistry model HAMMONIA have been accomplished in order to study the effects of the extreme solar particle precipitation events in late October and early November 2003 and subsequent particle precipitation on the atmosphere. The model treats radiation, neutral and ion chemistry, energetics, and dynamics interactively for an altitude range from the surface up to the thermosphere (about 250 km). Ionization rates provided by AIMOS (*Wissing and Kallenrode*, 2009) are used to describe precipitation of solar and magnetospheric protons, electrons, and α-particles into the entire atmosphere.
A possible influence of energetic particle precipitation on the terrestrial climate is indicated by previous studies (e.g. *Rozanov et al.*, 2005; *Seppälä et al.*, 2009) suggesting that the magnitude of the influence of precipitating energetic charged particles can potentially exceed the effects from variability in solar UV fluxes. With the background of an assessment of possible climate effects of energetic particle precipitation the present work is concerned with the following question:
• What is the influence of an extreme solar particle precipitation event and subsequent solar and magnetospheric particle precipitation on NO_x (odd nitrogen), HO_x (odd hydrogen), ozone, and temperature?
The importance of NO_x and HO_x results from a couple of reasons. These chemical components are known to be strongly affected by particle precipitation. They include highly reactive chemical species which are able to destroy ozone in catalytic reaction cycles. Ozone itself is an important absorber of UV radiation (*Hartley*, 1880; *Chappuis*, 1882; *Huggins and Huggins*, 1890) and therefore, it plays an important role for the energy budget in a wide atmospheric range. NO_x also directly affects the energy budget in the upper atmosphere through radiative cooling.
Along with the clarification of the general question, the following interesting aspects are discussed:

• What are the individual contributions of precipitating electrons, protons, and α-particles? It can help to reveal possible errors of previous studies considering the effects of particle precipitation events excluding substantial parts of the particle spectrum.
• Which role plays the NO_x production by precipitating magnetospheric particles, in particular electrons, and downward transport for the NO_x concentration in the middle atmosphere?
• Which mechanisms are responsible for PEP-induced temperature changes.
• Moreover, the explicit consideration of the temporal and spatial pattern of nearly the complete spectrum of precipitating particles and the consideration of ion chemistry allows a detailed assessment of possible error sources of the representation of NO_x in the model.

Causes for uncertainties of the representation of NO_x in the lower thermosphere in HAMMONIA are studied. Assuming that in the lower thermosphere NO_x is mainly represented by NO, the study starts with a comparison of NO densities predicted by HAMMONIA and calculated by the NO empirical model (NOEM) (*Marsh et al.*, 2004). The comparison shows qualitatively good agreements between HAMMONIA and NOEM, even though NO densities in NOEM tend to be higher than those in HAMMONIA by a factor of up to two. At least partially, this underestimation of the NO densities in HAMMONIA can be explained by the underestimated PEP-induced ionization rates. Underestimations of ionization rates in the auroral regions are indicated by a comparison of predicted electron densities with ISR measurements. Significantly underestimated temperatures in the thermosphere above a pressure level of about $2{\cdot}10^{-5}$ hPa in HAMMONIA are indicated by a comparison with temperatures calculated by the empirical model NRLMSISE-00 (*Picone et al.*, 2002). Since the strongly temperature dependent production of NO by the reaction of $N(^4S)$ with molecular oxygen weakens in the case of reduced temperatures, underestimated temperatures might be a further cause for an underestimation of NO densities in HAMMONIA. The comparison with NRLMSISE-00 indicates significantly overestimated concentrations of atomic oxygen in the southern hemispheric lower thermosphere. Consequently, more $N(^2D)$ can be quenched by atomic oxygen resulting in a weaker NO production by the reaction of $N(^2D)$ with molecular oxygen. Moreover, the comparison with NOEM indicates possible short-term overestimations of NO in the thermosphere of the northern hemispheric polar cap in HAMMONIA. Only in part, this can be explained by overestimated ionization rates which are found for short periods in this region. Consideration of the predicted meridional wind component indicates that overestimated horizontal transport in HAMMONIA can result in intrusion of NO-rich air from the auroral region into the polar cap regions where photolytical destruction vanishes and hence the NO density is significantly enhanced.

After the discussion of uncertainties in the representation of NO_x in HAMMONIA the combined effect of the complete particle spectrum on NO_x, HO_x, ozone, and temperature is studied. Therefore, differences between a simulation including the complete particle spectrum and a simulation without particle forcing are considered.

The examination of contributions of individual particle species considers differences between the simulation including the entire particle spectrum and simulations excluding single particle components.
It is shown that the combined effect of precipitating protons, electrons, and α-particles leads to significant enhancements of NO_x in the auroral and polar thermosphere, mesosphere and the upper stratosphere. During the pronounced event and the following weeks particle precipitation is responsible for NO_x enhancements of more than 1000% in the mesosphere and upper stratosphere. Substantial seasonal differences exist for the remaining time. In winter PEP-induced NO_x increases of more than 200% in the thermosphere and upper mesosphere lead to considerable NO_x densities, while the PEP influence in the thermosphere in summer is relatively weak. NO_x increases of up to 1000% are predicted in the mesosphere during the entire summer. However, the absolute NO_x densities are relatively low here. At mid-latitudes PEP-induced NO_x enhancements of 20 to 200% appear but they are mostly confined to the mesosphere.
The consideration of contributions of individual particle species shows, that NO_x in the auroral and polar thermosphere in winter is mainly produced by precipitating electrons. Here, in relation to the simulation which excludes electrons, these particles often lead to NO_x enhancements of more than 100%. It is also shown that the influence of precipitating electrons is responsible for 50-80% of the NO_x density in the polar and auroral thermosphere and mesosphere in winter. In summer, significant influence of precipitating electrons is confined to the mesosphere, albeit the resulting NO_x densities are relatively low.
In general, α-particles are responsible for less than 10% of the NO_x density. In the polar and auroral lower mesosphere and upper stratosphere during the pronounced particle events in late October and early November 2003, the altitude and time range where the strongest particle-induced NO_x increase is found, the influence of precipitating protons is responsible for 50 to 90% of the NO_x amount. During the following weeks, the influence of protons gradually decreases. In the mesosphere, already after one month, the effect of electrons exceeds the proton effect significantly.
Model simulations show remarkable downward transport of NO_x from the upper to the middle atmosphere at high latitudes in a short period in winter. This downward transport causes a significant increase of the NO_x concentration in the mesosphere. Since descending NO_x primarily originates from the effect of precipitating electrons, downward transport leads to an increased indirect influence of electrons in the middle atmosphere. A comparison with observations (*Randall et al.*, 2006; *Reddmann et al.*, 2010) indicates that duration and strength of the downward transport event are underestimated in HAMMONIA simulations. Nevertheless, it is impressively shown that consideration of precipitating electrons (primarily of magnetospheric origin) into the thermosphere can be important for the determination of NO_x concentration in the middle atmosphere.
The combined effect of the complete PEP spectrum also leads to HO_x increases of up to 1000% in the northern polar middle atmosphere in late October and

early November 2003. These increases are short-term and associated with particle precipitation events arriving the middle atmosphere. Additional HO_x increases occur in the lower mesosphere and upper stratosphere in the following months. In the sunlit region PEP effects on HO_x are weak.
While protons cause nearly the complete PEP-induced HO_x increase during two severe PEP events in late October and early November, electrons are responsible for HO_x increases in the northern polar mesosphere and stratosphere during additional PEP events. In general, the effect of α-particles on HO_x is marginal.
The study also shows significant ozone depletions due to the influence of PEPs. Ozone depletions of more than 50% are found in the polar and auroral mesosphere during the Halloween storms. A long-term PEP-induced ozone depletion is shown in the stratosphere, where the ozone concentration decreases up to 30% at high latitudes in winter and up to 10% at high latitudes in summer. Contributions of precipitating electrons are found for short- and long-term ozone depletions, although, for long-term depletions the electron contribution is relatively small. Note, that the downward transport of NO_x, which is produced primarily by the influence of precipitating electrons, is thought to be underestimated in the simulations. Therefore, it can be guessed that ozone reduction by electron-induced NO_x is underestimated and thus, the electron effect on ozone is temporarily underestimated. The relative contribution of α-particles to ozone depletion is mostly marginal.
Furthermore, the present work shows PEP-induced temperature effects. In the summer hemisphere at high latitudes a remarkable temperature decrease can be found in parts of the stratosphere and mesosphere soon after the Halloween event. This temperature decrease is caused by a PEP-induced ozone destruction and an associated reduced heating by absorption of solar irradiance. The temperature decrease is similarly as shown in a previous study (*Jackman et al.*, 2007).
In the high latitude middle atmosphere in winter significant temperature differences are found between simulations with and without electron precipitation. The responsible mechanisms are not examined, but it indicates non-linear effects resulting from interactions between the effects of different PEP species.
The study also focuses on PEP-induced temperature effects in the thermosphere. A consideration of PEP-effects provides useful information about mechanisms affecting energetics and dynamics of the thermosphere which is an altitude region where energetics and dynamics are less understood until today. Remarkable temperature effects in the thermosphere are revealed for periods of high particle precipitation activity. It is shown that PEP-induced strengthening of chemical heating and Joule heating is responsible for a simulated temperature increase of more than 20 K at high latitudes. An exception is found in the lower polar summer thermosphere where the simulation shows a PEP-induced temperature decrease of up to 10 K in time average. This temperature decrease is thought to be caused by changes of the winds due to ion drag resulting from interactions between neutral gas and plasma.

The results of this work point out the importance of precipitating electrons

which are thought to be primarily provided by magnetospheric particle precipitation. It is shown that the effects of electron precipitation significantly increases or exceed mid- and long-term effects of a severe proton dominated solar particle precipitation event. It is concluded that precipitation of magnetospheric particles or electrons, respectively, must be taken into account in studies which consider mid- and long-term or climate effects of strong particle precipitation events.

7.2 Outlook

Although the results of this work show impressively the considerable influence of particle precipitation on the atmosphere and, in particular, the importance of precipitating electrons, many challenges remain. Uncertainties remain regarding NO_x which is transported from upper atmospheric levels downward to the middle atmosphere. Therefore, also uncertainties exist in regard to processes resulting from the influence of descending NO_x as ozone depletion and consequent temperature effects. Since it is guessed that improvements of the representation of NO_x downward transport in the model are achieved in the case of higher spatial model resolution, for the future it is suggested to carry out model simulations with higher spatial resolution. Then the results should be compared with the current results in order to study the effect of different model resolutions on NO_x downward transport. In the case of an improvement, future HAMMONIA studies concerning the PEP impact on the atmosphere should use higher spatial resolution.
Temperature effects in the middle atmosphere due to electron precipitation are shown by the study but the responsible mechanisms are not understood. Before causes of these effects are studied, the significance of the effect has to be confirmed. Therefore, it is suggested that model simulations should be repeated for at least five additional ensemble members per experiment.
For an assessment of possible climate effects of energetic charged particle precipitation, being the background of this work, long-term effects of particle precipitation events should be studied in a next step. Such a study should be based on simulations over several decades considering precipitation of the full particle spectrum and simulations without particle forcing.

Appendix A

Chemical Reactions

Table A.1— Reactions involving PEPs included in the model

reaction					ref.
O	+	p^*	$\rightarrow$	$O^+ + e^-$	r
O_2	+	p^*	$\rightarrow$	$O_2^+ + e^-$	r
O_2	+	p^*	$\rightarrow$	$O^+ + O + e^-$	r
N_2	+	p^*	$\rightarrow$	$N_2^+ + e^-$	r
N_2	+	p^*	$\rightarrow$	$N^+ + 0.5 \cdot N(^2D) + 0.5 \cdot N + e^-$	r
N_2	+	p^*	$\rightarrow$	$0.8 \cdot N + 1.2 \cdot N(^2D)$	v

taken from: r) *Roble and Ridley* (1987); v) *Verronen* (2006)

Table A.2— EUV photolysis and UV ionization reactions included in the model

reaction					ref.
O	+	$h\nu_{EUV}$	$\rightarrow$	$O^+ + e^-$	s
O	+	$h\nu_{EUV}$	$\rightarrow$	$O^+ + e^-$	s
O_2	+	$h\nu_{EUV}$	$\rightarrow$	$O_2^+ + e^-$	s
O_2	+	$h\nu_{EUV}$	$\rightarrow$	$O(^1D) + O$	s, l
O_2	+	$h\nu_{EUV}$	$\rightarrow$	$O^+ + O + e^-$	s
N_2	+	$h\nu_{EUV}$	$\rightarrow$	$N_2^+ + e^-$	s
N_2	+	$h\nu_{EUV}$	$\rightarrow$	$N^+ + 0.5 \cdot N + 0.5 \cdot N(^2D) + e^-$	s
N_2	+	$h\nu_{EUV}$	$\rightarrow$	$0.8 \cdot N + 1.2 \cdot N(^2D)$	s
NO	+	$h\nu_{UV}$	$\rightarrow$	$NO^+ + e^-$	m

taken from: s) *Solomon and Qian* (2005); m) *Minschwaner and Siskind* (1993)
l) branching ratio taken from:
Atomic and Molecular Database http://amop.space.swri.edu

Table A.3— Photolysis reactions included in the model

O_2	+	$h\nu$	→	$O + O(^1D)$
O_2	+	$h\nu$	→	$2 \cdot O$
O_3	+	$h\nu$	→	$O(^1D) + O_2$
O_3	+	$h\nu$	→	$O + O_2$
N_2O	+	$h\nu$	→	$O(^1D) + N_2$
NO	+	$h\nu$	→	$N + O$
NO_2	+	$h\nu$	→	$NO + O$
N_2O_5	+	$h\nu$	→	$NO_2 + NO_3$
N_2O_5	+	$h\nu$	→	$NO + O + NO_3$
HNO_3	+	$h\nu$	→	$NO_2 + OH$
NO_3	+	$h\nu$	→	$NO_2 + O$
NO_3	+	$h\nu$	→	$NO + O_2$
HO_2NO_2	+	$h\nu$	→	$OH + NO_3$
HO_2NO_2	+	$h\nu$	→	$NO_2 + HO_2$
CH_3OOH	+	$h\nu$	→	$CH_2O + H + OH$
CH_2O	+	$h\nu$	→	$CO + 2 \cdot H$
CH_2O	+	$h\nu$	→	$CO + H_2$
H_2O	+	$h\nu$	→	$OH + H$
H_2O	+	$h\nu$	→	$H_2 + O(^1D)$
H_2O	+	$h\nu$	→	$2 \cdot H + O$
H_2O_2	+	$h\nu$	→	$2 \cdot OH$
Cl_2	+	$h\nu$	→	$2 \cdot Cl$
$OClO$	+	$h\nu$	→	$O + ClO$
Cl_2O_2	+	$h\nu$	→	$2 \cdot Cl$
$HOCl$	+	$h\nu$	→	$OH + Cl$
HCl	+	$h\nu$	→	$H + Cl$
$ClONO_2$	+	$h\nu$	→	$Cl + NO_3$
$ClONO_2$	+	$h\nu$	→	$ClO + NO_2$
$BrCl$	+	$h\nu$	→	$Br + Cl$
BrO	+	$h\nu$	→	$Br + O$
$HOBr$	+	$h\nu$	→	$Br + OH$
$BrONO_2$	+	$h\nu$	→	$Br + NO_3$
$BrONO_2$	+	$h\nu$	→	$BrO + NO_2$
CH_3Cl	+	$h\nu$	→	$Cl + CH_3O_2$
CCl_4	+	$h\nu$	→	$4 \cdot Cl$
CH_3CCl_3	+	$h\nu$	→	$3 \cdot Cl$
$CFCl_3$	+	$h\nu$	→	$3 \cdot Cl$
CF_2Cl_2	+	$h\nu$	→	$2 \cdot Cl$
$CFC113$	+	$h\nu$	→	$3 \cdot Cl$
$HCFC22$	+	$h\nu$	→	Cl
CH_3Br	+	$h\nu$	→	$Br + CH_3O_2$
CF_3Br	+	$h\nu$	→	Br
CF_2ClBr	+	$h\nu$	→	$Br + Cl$
CO_2	+	$h\nu$	→	$CO + O$
CH_4	+	$h\nu$	→	$H + CH_3O_2$
CH_4	+	$h\nu$	→	$1.44 \cdot H_2 + 0.18 \cdot CH_2O + 0.18 \cdot O + 0.66 \cdot OH$
				$+ 0.44 \cdot CO_2 + 0.38 \cdot CO + 0.05 \cdot H_2O$

reactions adopted from HAMMONIA-1 (*Schmidt et al.*, 2006)

Table A.4— Odd oxygen reactions included in the model

reaction			rate	ref.
$O + O_2 + \mathrm{M}$	$\rightarrow$	$O_3 + \mathrm{M}$	$6 \cdot 10^{-34} \cdot (300/T)^{2.4}$	
$O + O_3$	$\rightarrow$	$2 \cdot O_2 +$	$8 \cdot 10^{-12} \cdot e^{-2060/T}$	
$O + O + \mathrm{M}$	$\rightarrow$	$O_2 + \mathrm{M}$	$4.23 \cdot 10^{-28} \cdot T^{-2}$	
$O + H_2$	$\rightarrow$	$OH + H$	$7 \cdot 10^{-11} \cdot e^{-5130/T}$	
$O(^1D) + N_2$	$\rightarrow$	$O + N_2$	$2.15 \cdot 10^{-11} \cdot e^{110/T}$	
$O(^1D) + O_2$	$\rightarrow$	$O + O_2$	$3.3 \cdot 10^{-11} \cdot e^{55/T}$	
$O(^1D) + H_2O$	$\rightarrow$	$2 \cdot OH$	$1.63 \cdot 10^{-10} \cdot e^{60/T}$	
$O(^1D) + N_2O$	$\rightarrow$	$2 \cdot NO$	$6.7 \cdot 10^{-11} \cdot e^{20/T}$	
$O(^1D) + N_2O$	$\rightarrow$	$N_2 + O_2$	$4.7 \cdot 10^{-11} \cdot e^{20/T}$	
$O(^1D) + O_3$	$\rightarrow$	$2 \cdot O_2$	$1.20 \cdot 10^{-10}$	
$O(^1D) + CFCl3$	$\rightarrow$	$3 \cdot Cl$	$1.70 \cdot 10^{-10}$	
$O(^1D) + CF2Cl2$	$\rightarrow$	$2 \cdot Cl$	$1.20 \cdot 10^{-10}$	
$O(^1D) + CFC113$	$\rightarrow$	$3 \cdot Cl$	$1.50 \cdot 10^{-10}$	
$O(^1D) + HCFC22$	$\rightarrow$	Cl	$7.20 \cdot 10^{-11}$	
$O(^1D) + CH_4$	$\rightarrow$	$CH_3O_2 + OH$	$1.125 \cdot 10^{-10}$	
$O(^1D) + CH_4$	$\rightarrow$	$CH_2O + H + HO_2$	$3.0 \cdot 10^{-11}$	
$O(^1D) + CH_4$	$\rightarrow$	$CH_2O + H_2$	$7.5 \cdot 10^{-12}$	
$O(^1D) + H_2$	$\rightarrow$	$H + OH$	$1.1 \cdot 10^{-10}$	
$O(^1D) + HCl$	$\rightarrow$	$Cl + OH$	$1.005 \cdot 10^{-10}$	
reactions adopted from HAMMONIA-1 (*Schmidt et al.*, 2006) rate coefficients updated to *Sander et al.* (2006)				
$O(^1D) + N_2 + \mathrm{M}$	$\rightarrow$	$N_2O + \mathrm{M}$	$3.5 \cdot 10^{-37} \cdot (300/T)^{0.6}$	v
$O(^1D) + O$	$\rightarrow$	$O + O$	$8 \cdot 10^{-12}$	s
$O(^1D) + O_3$	$\rightarrow$	$O_2 + 2 \cdot O$	$1.20 \cdot 10^{-10}$	s
$O(^1D) + HCl$	$\rightarrow$	$ClO + H$	$3.6 \cdot 10^{-11}$	s
$O(^1D) + HCl$	$\rightarrow$	$HCl + O$	$1.35 \cdot 10^{-11}$	s
newly implemented in HAMMONIA-2, taken from: v) *Verronen* (2006); s) *Sander et al.* (2006)				

Table A.5— Odd Nitrogen reactions included in the model

reaction			rate	ref.
$N(^2D) + O_2 +$	$\rightarrow$	$NO + O$	$2.95 \cdot 10^{-12}$	
$N(^2D) + O$	$\rightarrow$	$N + O$	$6.9 \cdot 10^{-13}$	
$N + O_2$	$\rightarrow$	$NO + O$	$1.5 \cdot 10^{-11} \cdot e^{-3600/T}$	
$N + NO$	$\rightarrow$	$N_2 + O$	$2.1 \cdot 10^{-11} \cdot e^{100/T}$	
$NO + O + \mathrm{M}$	$\rightarrow$	$NO_2 + \mathrm{M}$	troe: $k_0 = 9.0 \cdot 10^{-32} \cdot (300/T)^{1.5}$ $k_i = 3.0e-11$	
$NO + HO_2$	$\rightarrow$	$NO_2 + OH$	$3.5 \cdot 10^{-12} \cdot e^{250/T}$	
$NO + O_3$	$\rightarrow$	$NO_2 + O_2$	$3 \cdot 10^{-12} \cdot e^{-1500/T}$	
$NO_2 + O$	$\rightarrow$	$NO + O_2$	$5.1 \cdot 10^{-12} \cdot e^{210/T}$	
$NO_2 + O + \mathrm{M}$	$\rightarrow$	$NO_3 + \mathrm{M}$	troe: $k_0 = 2.5 \cdot 10^{-31} \cdot (300/T)^{1.8}$ $k_i = 2.2 \cdot 10^{-11} \cdot (300/T)^{0.7}$	
$NO_2 + O_3$	$\rightarrow$	$NO_3 + O_2$	$1.2 \cdot 10^{-13} \cdot e^{-2450/T}$	
$NO_2 + NO_3 + \mathrm{M}$	$\rightarrow$	$N_2O_5 + \mathrm{M}$	troe: $k_0 = 2 \cdot 10^{-30} \cdot (300/T)^{4.4}$ $k_i = 1.4 \cdot 10^{-12} \cdot (300/T)^{0.7}$	
$N_2O_5 + \mathrm{M}$	$\rightarrow$	$NO_2 + NO_3 + \mathrm{M}$	(prev. reaction) $\cdot 3.333 \cdot 10^{26} \cdot e^{-10991/T}$	
$NO_2 + OH + \mathrm{M}$	$\rightarrow$	$HNO_3 + \mathrm{M}$	troe: $k_0 = 1.8 \cdot 10^{-30} \cdot (300/T)^{3.0}$ $k_i = 2.8e-11$	
$HNO_3 + OH$	$\rightarrow$	$NO_3 + H_2O$	$aux2 + 2.4 \cdot 10^{-14} \cdot e^{460/T}$ $aux1 = 6.5 \cdot 10^{34} \cdot e^{1335/T} \cdot am$ $aux2 = aux1/(1+aux1 \cdot (2.7 \cdot 10^{-17} \cdot e^{2199/T})^{-1}$	
$NO_3 + NO$	$\rightarrow$	$2 \cdot NO_2$	$1.5 \cdot 10^{-11} \cdot e^{170/T}$	
$NO_3 + O$	$\rightarrow$	$NO_2 + O_2$	$1 \cdot 10^{-11}$	
$NO_3 + OH$	$\rightarrow$	$HO_2 + NO_2$	$2.2 \cdot 10^{-11}$	
$NO_3 + HO_2$	$\rightarrow$	$OH + NO_2 + O_2$	$3.5 \cdot 10^{-12}$	
$NO_2 + HO_2 + \mathrm{M}$	$\rightarrow$	$HO_2NO_2 + \mathrm{M}$	troe: $k_0 = 2.0 \cdot 10^{-31} \cdot (300/T)^{3.4}$ $k_i = 2.9e-12 \cdot (300/T)^{1.1}$	
$HO_2NO_2 + OH$	$\rightarrow$	$H_2O + NO_2 + O_2$	$1.3 \cdot 10^{-12} \cdot e^{380/T}$	
$HO_2NO_2 + \mathrm{M}$	$\rightarrow$	$HO_2 + NO_2 + \mathrm{M}$	$k_{37} \cdot e^{-10900/T}/2.1 \cdot 10^{-27}$	

reactions adopted from HAMMONIA-1 (*Schmidt et al.*, 2006)
rate coefficients updated to *Sander et al.* (2006)
rate coefficients for troe-reaction are given as
$k = \frac{k_0}{1+(k_0 \cdot am)/k_i} \cdot 0.6^{(1+(log(k_0 \cdot am/k_i))^2)^{-1}}$; am: air density (number per cm^{-3})

$N(^2D) + O_2$	$\rightarrow$	$NO + O(^1D)$	$2.95 \cdot 10^{-12}$	s
$N(^2D) + NO$	$\rightarrow$	$N_2 + O$	$7 \cdot 10^{-11}$	s
$NO_2 + N$	$\rightarrow$	$N_2O + O$	$5.8 \cdot 10^{-12} \cdot e^{220/T}$	v
$NO_2 + H$	$\rightarrow$	$OH + NO$	$4 \cdot 10^{-10} \cdot e^{-340/T}$	v
$NO_3 + NO_3$	$\rightarrow$	$NO_2 + NO_2 + O_2$	$8.5 \cdot 10^{-13} \cdot e^{-2450/T}$	v
$N + OH$	$\rightarrow$	$NO + H$	$5.3 \cdot 10^{-11}$	s

newly implemented in HAMMONIA-2, taken from:
v) *Verronen* (2006); s) *Sander et al.* (2006)

Table A.6— Methane, CO, CH_2O and derivatives reactions included in the model

reaction			rate
$CH_4 + OH$	$\rightarrow$	$CH_3O_2 + H_2O$	$2.45 \cdot 10^{-12} \cdot e^{-1775/T}$
$CH_3O_2 + NO$	$\rightarrow$	$CH_2O + NO_2 + HO_2$	$2.8 \cdot 10^{-12} \cdot e^{300/T}$
$CH_3O_2 + HO_2$	$\rightarrow$	$CH_3OOH + O_2$	$4.1 \cdot 10^{-13} \cdot e^{750/T}$
$CH_3OOH + OH$	$\rightarrow$	$CH_3O_2 + H_2O$	$3.8 \cdot 10^{-12} \cdot e^{200/T}$
$CH_2O + NO_3$	$\rightarrow$	$CO + HO_2 + HNO_3$	$6.0 \cdot 10^{-13} \cdot e^{-2058/T}$
$CH_2O + OH$	$\rightarrow$	$CO + H_2O + H$	$9.0 \cdot 10^{-12}$
$CH_2O + O$	$\rightarrow$	$HO_2 + OH + CO$	$3.4 \cdot 10^{-11} \cdot e^{-1600/T}$
$CO + OH$	$\rightarrow$	$CO_2 + H$	$1.5 \cdot 10^{-13} \cdot (1 + 6 \cdot 10^{-7} \cdot k_B \cdot m \cdot T)$
reactions adopted from HAMMONIA-1 (*Schmidt et al.*, 2006) rate coefficients updated to *Sander et al.* (2006)			
$CO + O + \mathrm{M}$	$\rightarrow$	$CO_2 + M$	$6.6 \cdot 10^{-33} \cdot e^{-1103/T}$
newly implemented in HAMMONIA-2, taken from *Roble* (1995)			

Table A.7— Odd hydrogen reactions included in the model

reaction			rate
$H + O_2 + \mathrm{M}$	$\rightarrow$	$HO_2 + M$	troe: $4.4 \cdot 10^{-32} \cdot (300/T)^{1.3}$ $k_i = 4.7 \cdot 10^{-11} \cdot (300/T)^{0.2}$
$H + O_3$	$\rightarrow$	$OH + O_2$	$1.40 \cdot 10^{-10} \cdot e^{-470.0/T}$
$H + HO_2$	$\rightarrow$	$2 \cdot OH$	$7.2 \cdot 10^{-11}$
$H + HO_2$	$\rightarrow$	$H_2 + O_2$	$6.9 \cdot 10^{-12}$
$H + HO_2$	$\rightarrow$	$H_2O + O$	$1.6 \cdot 10^{-12}$
$OH + O$	$\rightarrow$	$H + O_2$	$2.2 \cdot 10^{-11} \cdot e^{120/T}$
$OH + O_3$	$\rightarrow$	$HO_2 + O_2$	$1.7 \cdot 10^{-12} \cdot e^{-940/T}$
$OH + HO_2$	$\rightarrow$	$H_2O + O_2$	$4.8 \cdot 10^{-11} \cdot e^{250/T}$
$OH + OH$	$\rightarrow$	$H_2O + O$	$1.8 \cdot 10^{-12}$
$OH + OH + \mathrm{M}$	$\rightarrow$	$H_2O_2 + M$	troe: $k_0 = 6.9 \cdot 10^{-31} \cdot (300/T)^{1.0}$ $k_i = 2.6 \cdot 10^{-11}$
$OH + H_2$	$\rightarrow$	$H_2O + H$	$2.8 \cdot 10^{-12} \cdot e^{-1800/T}$
$OH + H_2O_2$	$\rightarrow$	$H_2O + HO_2$	$2.9 \cdot 10^{-12} \cdot e^{-160/T}$
$HO_2 + O$	$\rightarrow$	$OH + O_2$	$3.0 \cdot 10^{-11} \cdot e^{200/T}$
$HO_2 + O_3$	$\rightarrow$	$OH + 2 \cdot O_2$	$1.0 \cdot 10^{-14} \cdot e^{-490/T}$
$HO_2 + HO_2$	$\rightarrow$	$H_2O_2 + O_2$	$(2.3 \cdot 10^{-13} \cdot e^{600/T} + aux1) \cdot aux2$ $aux1 = 1.7 \cdot 10^{-33} \cdot am \cdot e^{1000/T}$ $aux2 = 1 + 1.4 \cdot 10^{-21} \cdot am \cdot H_2O \cdot e^{2200/T}$
$H_2O_2 + O$	$\rightarrow$	$OH + HO_2$	$1.4 \cdot 10^{-12} \cdot e^{-2000/T}$

reactions adopted from HAMMONIA-1 (*Schmidt et al.*, 2006)
rate coefficients updated to *Sander et al.* (2006)
rate coefficients for troe-reaction are given as
$k = \frac{k_0}{1+(k_0 \cdot am)/k_i} \cdot 0.6^{(1+(log(k_0 \cdot am/k_i))^2)^{-1}}$; am: air density (number per cm^{-3})

$H + H + \mathrm{M}$	$\rightarrow$	$H_2 + M$	$5.7 \cdot 10^{-32} \cdot (300/T)^{1.6}$

newly implemented in HAMMONIA-2, taken from *Roble* (1995)

Table A.8— Odd chlorine reactions included in the model

reaction			rate
$Cl + O_3$	$\rightarrow$	$ClO + O_2$	$2.3 \cdot 10^{-11} \cdot e^{-200/T}$
$Cl + H_2$	$\rightarrow$	$HCl + H$	$3.05 \cdot 10^{-11} \cdot e^{-2270/T}$
$Cl + H_2O_2$	$\rightarrow$	$HCl + HO_2$	$1.1 \cdot 10^{-11} \cdot e^{-980/T}$
$Cl + HO_2$	$\rightarrow$	$HCl + O_2$	$1.8 \cdot 10^{-11} \cdot e^{170/T}$
$Cl + HO_2$	$\rightarrow$	$OH + ClO$	$4.1 \cdot 10^{-11} \cdot e^{-450/T}$
$Cl + CH_2O$	$\rightarrow$	$HCl + HO_2 + CO$	$8.1 \cdot 10^{-11} \cdot e^{-30/T}$
$Cl + CH_4$	$\rightarrow$	$CH_3O_2 + HCl$	$9.6 \cdot 10^{-12} \cdot e^{-1360/T}$
$ClO + O$	$\rightarrow$	$Cl + O_2$	$3.0 \cdot 10^{-11} \cdot e^{70/T}$
$ClO + OH$	$\rightarrow$	$Cl + HO_2$	$7.4 \cdot 10^{-12} \cdot e^{270/T}$
$ClO + OH$	$\rightarrow$	$HCl + O_2$	$6.0 \cdot 10^{-13} \cdot e^{230/T}$
$ClO + HO_2$	$\rightarrow$	$O_2 + HOCl$	$2.7 \cdot 10^{-12} \cdot e^{220/T}$
$ClO + NO$	$\rightarrow$	$NO_2 + Cl$	$6.4 \cdot 10^{-12} \cdot e^{290/T}$
$ClO + NO_2$+M	$\rightarrow$	$ClONO_2 + M$	troe: $k_0 = 1.8 \cdot 10^{-31} \cdot (300/T)^{3.4}$ $k_i = 1.5 \cdot 10{-}11 \cdot (300/T)^{1.9}$
$ClO + ClO$	$\rightarrow$	$2 \cdot Cl + O_2$	$3.0 \cdot 10^{-11} \cdot e^{-2450/T}$
$ClO + ClO$	$\rightarrow$	$Cl_2 + O_2$	$1.0 \cdot 10^{-12} \cdot e^{-1590/T}$
$ClO + ClO$	$\rightarrow$	$Cl + OClO$	$3.5 \cdot 10^{-13} \cdot e^{-1370/T}$
$ClO + ClO$ +M	$\rightarrow$	$Cl_2O_2 + M$	troe: $k_0 = 1.6 \cdot 10^{-32} \cdot (300/T)^{4.5}$ $k_i = 2.0 \cdot 10{-}12 \cdot (300/T)^{2.4}$
Cl_2O_2+ M	$\rightarrow$	$2 \cdot ClO + M$	prev. reaction / $1.3 \cdot 10^{-27} \cdot e^{8744/T}$
$HCl + OH$	$\rightarrow$	$H_2O + Cl$	$2.6 \cdot 10^{-12} \cdot e^{-350/T}$
$HCl + O$	$\rightarrow$	$Cl + OH$	$1.0 \cdot 10^{-11} \cdot e^{-3300/T}$
$HOCl + O$	$\rightarrow$	$ClO + OH$	$1.7 \cdot 10^{-13}$
$HOCl + Cl$	$\rightarrow$	$HCl + ClO$	$2.5 \cdot 10^{-12} \cdot e^{-130/T}$
$HOCl + OH$	$\rightarrow$	$H_2O + ClO$	$3.0 \cdot 10^{-12} \cdot e^{-500/T}$
$ClONO_2$+ O	$\rightarrow$	$ClO + NO_3$	$2.9 \cdot 10^{-12} \cdot e^{-800/T}$
$ClONO_2$+ OH	$\rightarrow$	$HOCl + NO_3$	$1.2 \cdot 10^{-12} \cdot e^{-330/T}$
$ClONO_2$+ Cl	$\rightarrow$	$Cl_2 + NO_3$	$6.5 \cdot 10^{-12} \cdot e^{135/T}$

reactions adopted from HAMMONIA-1 (*Schmidt et al.*, 2006)
rate coefficients updated to *Sander et al.* (2006)
rate coefficients for troe-reaction are given as
$k = \frac{k_0}{1+(k_0 \cdot am)/k_i} \cdot 0.6^{(1+(log(k_0 \cdot am/k_i))^2)^{-1}}$; am: air density (number per cm^{-3})

Table A.9— Odd bromine reactions included in the model

reaction			rate
$Br + O_3$	$\rightarrow$	$BrO + O_2$	$1.7 \cdot 10^{-11} \cdot e^{-800/T}$
$Br + HO_2$	$\rightarrow$	$HBr + O_2$	$1.5 \cdot 10^{-11} \cdot e^{-600/T}$
$Br + CH_2O$	$\rightarrow$	$HBr + HO_2{+}CO$	$1.7 \cdot 10^{-11} \cdot e^{-800/T}$
$BrO + O$	$\rightarrow$	$Br + O_2$	$1.9 \cdot 10^{-11} \cdot e^{230/T}$
$BrO + OH$	$\rightarrow$	$Br + HO_2$	$7.5 \cdot 10^{-11}$
$BrO + HO_2$	$\rightarrow$	$HOBr + O_2$	$3.4 \cdot 10^{-12} \cdot e^{540/T}$
$BrO + NO$	$\rightarrow$	$Br + NO_2$	$8.8 \cdot 10^{-12} \cdot e^{260/T}$
$BrO + NO_2{+}$ M	$\rightarrow$	$BrONO_2 + M$	troe: $k_0 = 5.2 \cdot 10^{-31} \cdot (300/T)^{3.2}$ $k_i = 6.9 \cdot 10{-}12 \cdot (300/T)^{2.9}$
$BrO + ClO$	$\rightarrow$	$Br + OClO$	$9.5 \cdot 10^{-13} \cdot e^{550/T}$
$BrO + ClO$	$\rightarrow$	$Br + Cl{+}O_2$	$2.3 \cdot 10^{-12} \cdot e^{260/T}$
$BrO + ClO$	$\rightarrow$	$BrCl + O_2$	$4.1 \cdot 10^{-13} \cdot e^{290/T}$
$BrO + BrO$	$\rightarrow$	$2 \cdot Br + O_2$	$1.5 \cdot 10^{-12} \cdot e^{230/T}$
$HBr + OH$	$\rightarrow$	$2 \cdot Br + H_2O$	$1.1 \cdot 10^{-11}$

reactions adopted from HAMMONIA-1 (*Schmidt et al.*, 2006)
rate coefficients updated to *Sander et al.* (2006)
rate coefficients for troe-reaction are given as
$k = \frac{k_0}{1+(k_0 \cdot am)/k_i} \cdot 0.6^{(1+(log(k_0 \cdot am/k_i))^2)^{-1}}$; am: air density (number per cm^{-3})

Table A.10— Halogens reactions with Cl or OH included in the model

reaction			rate
$CH_3Cl + Cl$	$\rightarrow$	$HO_2 + CO + 2{\cdot}HCl$	$3.2 \cdot 10^{-11} \cdot e^{-1250/T}$
$CH_3Cl + OH$	$\rightarrow$	$Cl + H_2O + HO_2$	$2.4 \cdot 10^{-12} \cdot e^{-1250/T}$
$CH_3CCl_3 + OH$	$\rightarrow$	$3 \cdot Cl + H_2O$	$1.6 \cdot 10^{-12} \cdot e^{-1520/T}$
$HCFC22 + OH$	$\rightarrow$	$Cl + H_2O{+}CF_2O$	$4.0 \cdot 10^{-12} \cdot e^{-1400/T}$
$CH_3Br + OH$	$\rightarrow$	$Br + H_2O{+}HO_2$	$2.35 \cdot 10^{-12} \cdot e^{-1300/T}$

reactions adopted from HAMMONIA-1 (*Schmidt et al.*, 2006)
rate coefficients updated to *Sander et al.* (2006)

Table A.11— Sulfate aerosol reactions included in the model

reaction		
N_2O_5	$\rightarrow$	$2 \cdot HNO_3$
$ClONO_2$	$\rightarrow$	$HOCl + HNO_3$
$BrONO_2$	$\rightarrow$	$HOBr + HNO_3$
$ClONO_2 + HCl$	$\rightarrow$	$Cl_2 + HNO_3$
$HOCl + HCl$	$\rightarrow$	$Cl_2 + H_2O$
$HOBr + HCl$	$\rightarrow$	$BrCl + H_2O$

reactions adopted from HAMMONIA-1 (*Schmidt et al.*, 2006)

Table A.12— Nitric acid di-hydrate reactions included in the model

reaction		
N_2O_5	$\rightarrow$	$2 \cdot HNO_3$
$ClONO_2$	$\rightarrow$	$HOCl + HNO_3$
$ClONO_2 + HCl$	$\rightarrow$	$Cl_2 + HNO_3$
$HOCl + HCl$	$\rightarrow$	$Cl_2 + H_2O$
$BrONO_2$	$\rightarrow$	$HOBr + HNO_3$

reactions adopted from HAMMONIA-1 (*Schmidt et al.*, 2006)

Table A.13— Ice aerosol reactions included in the model

reaction		
N_2O_5	$\rightarrow$	$2 \cdot HNO_3$
$ClONO_2$	$\rightarrow$	$HOCl + HNO_3$
$ClONO_2 + HCl$	$\rightarrow$	$Cl_2 + HNO_3$
$HOCl + HCl$	$\rightarrow$	$Cl_2 + H_2O$
$BrONO_2 +$	$\rightarrow$	$HOBr + HNO_3$
$HOBr + HCl$	$\rightarrow$	$BrCl + H_2O$

reactions adopted from HAMMONIA-1 (*Schmidt et al.*, 2006)

Table A.14— Ion/electron recombination reactions included in the model

reaction			rate	ref.
$O^+ + e^-$	$\rightarrow$	O	$3.24 \cdot 10^{-12} \cdot (300/T)^{0.66}$	k
$O_2^+ + e^-$	$\rightarrow$	$0.85 \cdot O(^1D) + 1.15 \cdot O$	$T_e < 1200K : 2.70 \cdot 10^{-7} \cdot (300/T_e)^{0.7}$	r
			$T_e \geq 1200K : 1.60 \cdot 10^{-7} \cdot (300/T_e)^{0.55}$	
$N^+ + e^-$	$\rightarrow$	N	$4.0 \cdot 10^{-12} \cdot (300/T)^{0.58}$	k
$N_2^+ + e^-$	$\rightarrow$	$1.1 \cdot N(^2D) + 0.9 \cdot N$	$1.8 \cdot 10^{-7} \cdot (300/T_e)^{0.39}$	v
$NO^+ + e^-$	$\rightarrow$	$0.85 \cdot N(^2D) + 0.15 \cdot N$	$4.2 \cdot 10^{-7} \cdot (300/T_e)^{0.85}$	v

taken from: k) *Kazil* (2002); r) *Roble and Ridley* (1987); v) *Verronen* (2006)

Table A.15— Ion neutral reactions and rate coefficients included in the model

reaction			rate	ref.
$O^+ + O_2$	$\rightarrow$	$O_2^+ + O$	$1.9 \cdot 10^{-11} \cdot (300/T)^{0.4}$	k
$O^+ + N_2$	$\rightarrow$	$NO^+ + N$	$1.2 \cdot 10^{-12} \cdot (300/T)^{0.74}$	k
$N_2^+ + O_2$	$\rightarrow$	$O_2^+ + N_2$	$5.1 \cdot 10^{-11} \cdot (300/T)^{0.8}$	k
$N_2^+ + O$	$\rightarrow$	$NO^+ + N(^2D)$	$1.4 \cdot 10^{-10} \cdot (300/T)^{0.44}$	k
$N_2^+ + O$	$\rightarrow$	$O^+ + N_2$	$1.0 \cdot 10^{-11} \cdot (300/T)^{0.23}$	k
$O_2^+ + NO$	$\rightarrow$	$NO^+ + O_2$	$4.4 \cdot 10^{-10}$	k
$O_2^+ + N$	$\rightarrow$	$NO^+ + O$	$1.2 \cdot 10^{-10}$	k
$O_2^+ + N_2$	$\rightarrow$	$NO^+ + NO$	$2.0 \cdot 10^{-18}$	v
$N^+ + O_2$	$\rightarrow$	$O_2^+ + 0.35 \cdot N + 0.65 \cdot N(^2D)$	$2.0 \cdot 10^{-10}$	v
$N^+ + O_2$	$\rightarrow$	$NO^+ + O$	$2.32 \cdot 10^{-10}$	k
$N^+ + O$	$\rightarrow$	$O^+ + N$	$1.0 \cdot 10^{-12}$	r
$N^+ + O_2$	$\rightarrow$	$O^+ + NO$	$3.0 \cdot 10^{-11}$	v
$e^- + N(^2D)$	$\rightarrow$	$N + e^-$	$3.6 \cdot 10^{-10} \cdot (300/T_e)^{-0.5}$	f

taken from: f) *Frederick and Rusch* (1977), k) *Kazil* (2002),
r) *Roble* (1995), v) *Verronen* (2006),

Table A.16— Exothermic chemical reactions and exothermicities adopted from HAMMONIA-1

reaction	exothermicity
$O + O_2 + M \rightarrow O_3 + M$	101.3 kJ/mol
$O + O_3 \rightarrow 2 \cdot O_2$	391.7 kJ/mol
$O + O + M \rightarrow O_2 + M$	493.0 kJ/mol
$H + O_2 + M \rightarrow HO_2 + M$	193.0 kJ/mol
$O + O_3 \rightarrow OH + O_2$	322.2 kJ/mol
$O + OH \rightarrow O_2 + H$	69.5 kJ/mol
$O + HO_2 \rightarrow OH + O_2$	230.6 kJ/mol

Table A.17— exothermic chemical reactions and exothermicities newly implemented in HAMMONIA-2

reaction	exothermicity
$O(^1D) + O \rightarrow O + O$	189.1 kJ/mol
$O(^1D) + O_2 \rightarrow O + O_2$	189.1 kJ/mol
$O(^1D) + O_3 \rightarrow O_2 + O_2$	189.1 kJ/mol
$O(^1D) + N_2 \rightarrow O + N_2$	189.1 kJ/mol
$O(^1D) + H_2O \rightarrow 2 \cdot OH$	118.7 kJ/mol
$O(^1D) + H_2 \rightarrow H + OH$	181.4 kJ/mol
$N(^2D) + O \rightarrow N + O$	229.6 kJ/mol
$N(^2D) + O_2 \rightarrow NO + O$	362.8 kJ/mol
$N(^2D) + NO \rightarrow N_2 + O$	543.2 kJ/mol
$N + NO \rightarrow N_2 + O$	313.6 kJ/mol
$N + O_2 \rightarrow NO + O$	135.1 kJ/mol
$N + OH \rightarrow NO + H$	202.6 kJ/mol
$NO + O_3 \rightarrow NO_2 + O_2$	200.7 kJ/mol
$NO + HO_2 \rightarrow NO_2 + OH$	33.8 kJ/mol
$NO_2 + O \rightarrow NO + O_2$	191.0 kJ/mol
$NO_2 + O_3 \rightarrow NO_3 + O_2$	104.2 kJ/mol
$H + O_2 + M \rightarrow HO_2 + M$	203.6 kJ/mol
$H + O_3 \rightarrow OH + O_2$	322.2 kJ/mol
$H + H + M \rightarrow H_2 + M$	436.1 kJ/mol
$H + HO_2 \rightarrow OH + OH$	155.3 kJ/mol
$H + HO_2 \rightarrow H_2 + O_2$	232.5 kJ/mol
$H + HO_2 \rightarrow H_2O + O$	225.8 kJ/mol
$OH + O_3 \rightarrow HO_2 + O_2$	167.0 kJ/mol
$OH + OH \rightarrow H_2O + O$	70.4 kJ/mol
$OH + HO_2 \rightarrow H_2O + O_2$	295.2 kJ/mol
$OH + H_2 \rightarrow H_2O + H$	62.7 kJ/mol
$OH + H_2O_2 \rightarrow H_2O + HO_2$	130.3 kJ/mol
$HO_2 + O_3 \rightarrow OH + 2 \cdot O_2$	118.7 kJ/mol
$HO_2 + HO_2 \rightarrow H_2O_2 + O_2$	165.0 kJ/mol
$CO + OH \rightarrow CO_2 + H$	103.2 kJ/mol
$CO + O + M \rightarrow CO_2 + M$	531.6 kJ/mol
$O^+ + O_2 \rightarrow O_2^+ + O$	150.1 kJ/mol
$O^+ + N_2 \rightarrow NO^+ + N$	105.0 kJ/mol
$O_2^+ + N \rightarrow NO^+ + O$	406.2 kJ/mol
$O_2^+ + NO \rightarrow NO^+ + O_2$	271.4 kJ/mol
$N^+ + O \rightarrow O^+ + N$	95.6 kJ/mol
$N^+ + O_2 \rightarrow O_2^+ + 0.35 \cdot N + 0.65 \cdot N(^2D)$	90.7 kJ/mol
$N^+ + O_2 \rightarrow NO^+ + O$	646.3 kJ/mol
$N_2^+ + O \rightarrow NO^+ + N(^2D)$	67.5 kJ/mol
$N_2^+ + O_2 \rightarrow O_2^+ + N_2$	339.6 kJ/mol
$NO^+ + e^- \rightarrow 0.15 \cdot N + 0.85 \cdot N(^2D) + O$	82.4 kJ/mol
$O_2^+ + e^- \rightarrow 1.15 \cdot O + 0.85 \cdot O(^1D)$	509.0 kJ/mol
$N_2^+ + e^- \rightarrow 1.1 \cdot N + 0.9 \cdot N(^2D)$	354.8 kJ/mol
$N(^2D) + e^- \rightarrow N + e^-$	229.6 kJ/mol

Appendix B

Acronyms

AIMOS Atmospheric Ionization Module Osnabrück

CMEs Coronal Mass Ejections

EUV Extreme Ultraviolet

GOMOS Global Ozone Monitoring by Occultation of Stars

HAMMONIA Hamburg Model of the Neutral and Ionized Atmosphere

IMF Interplanetary Magnetic Field

ISR Incoherent Scatter Radar

MEPs Magnetospheric Energetic Particles

MIPAS Michelson Interferometer for Passive Atmospheric Sounding

MLT Mesosphere (and) Lower Thermosphere

NH Northern Hemisphere

NOAA National Oceanic and Atmospheric Administration

NOEM Nitric Oxide Empirical Model

PEPs Precipitating Energetic Particles

POES Polar-orbiting Operational Environmental Satellite

SH Southern Hemisphere

SEPs Solar Energetic Particles

SSW Sudden Stratospheric Warming

SZA Solar Zenith Angle

TEM Transformed Eulerian Mean

UV Ultraviolet

List of Figures

List of Tables

Bibliography

Andrews, D. G., J. R. Holton, and C. B. Leovy (1987), *Middle atmosphere dynamics.*

Bailey, D. K. (1957), Disturbances in the Lower Ionosphere Observed at VHF Following the Solar Flare of 23 February 1956 with Particular Reference to Auroral-Zone Absorption, *J. Geophys. Res.*, *62*, 431–463, doi:10.1029/JZ062i003p00431.

Barth, C. A., K. D. Mankoff, S. M. Bailey, and S. C. Solomon (2003), Global observations of nitric oxide in the thermosphere, *J. Geophys. Res. (Space Physics)*, *108*, 1027–+, doi:10.1029/2002JA009458.

Bates, D. R. (1988), Recombination in the normal E and F layers of the ionosphere, *Planet. Space Sci.*, *36*, 55–63, doi:10.1016/0032-0633(88)90146-8.

Becker, E., and C. von Savigny (2010), Dynamical heating of the polar summer mesopause induced by solar proton events, *J. Geophys. Res.*, *115*, doi:10.1029/2009JD012561.

Brasseur, G. P., and S. Solomon (2005), *Aeronomy of the Middle Atmosphere*, Springer.

Breneman, H. H., and E. C. Stone (1985), Solar coronal and photospheric abundances from solar energetic particle measurements, *The Astrophysical Journal*, *299*, L57–L61, doi:10.1086/184580.

Callis, L. B., and M. Natarajan (1986), The Antarctic ozone minimum - Relationship to odd nitrogen, odd chlorine, the final warming, and the 11-year solar cycle, *J. Geophys. Res.*, *91*, 10,771–10,796, doi:10.1029/JD091iD10p10771.

Callis, L. B., R. E. Boughner, D. N. Baker, R. A. Mewaldt, J. B. Blake, R. S. Selesnick, J. R. Cummings, M. Natarajan, G. M. Mason, and J. E. Mazur (1996a), Precipitating electrons: Evidence for effects on mesospheric odd nitrogen, *Geophys. Res. Lett.*, *23*, 1901–1904, doi:10.1029/96GL01787.

Callis, L. B., D. N. Baker, M. Natarajan, J. B. Blake, R. A. Mewaldt, R. S. Selesnick, and J. R. Cummings (1996b), A 2-D model simulation of downward transport of NO_y into the stratosphere: Effects on the 1994 austral spring O_3 and NO_y, *Geophys. Res. Lett.*, *23*, 1905–1908, doi:10.1029/96GL01788.

Callis, L. B., M. Natarajan, D. S. Evans, and J. D. Lambeth (1998), Solar atmospheric coupling by electrons (SOLACE) 1. Effects of the May 12, 1997 solar event on the middle atmosphere, *J. Geophys. Res.*, *103*, 28,405–28,420, doi: 10.1029/98JD02408.

Chapman, S., and V. C. A. Ferraro (1931), A New Theory of Magnetic Storms., *Terr. Magn.*, *36*, 77.

Chapman, S., and G. C. Little (1957), The nondeviative absorption of high-frequency radio waves in auroral latitudes, *Journal of Atmospheric and Terrestrial Physics*, *10*, 20–31.

Chappuis, S. (1882), Surle spectre d'adsorption de l'ozone et de l'acide pernitrique, *Journal de Physique Théorique et Appliquée*, *1*, 494–504.

Charlton, A. J., and L. M. Polvani (2007), A New Look at Stratospheric Sudden Warmings. Part I: Climatology and Modeling Benchmarks, *Journal of Climate*, *20*, 449–+, doi:10.1175/JCLI3996.1.

Clilverd, M. A., A. Seppälä, C. J. Rodger, P. T. Verronen, and N. R. Thomson (2006), Ionospheric evidence of thermosphere-to-stratosphere descent of polar NO_X, *Geophys. Res. Lett.*, *33*, 19,811–+, doi:10.1029/2006GL026727.

Courant, R., K. Friedrichs, and H. Lewy (1967), On the Partial Difference Equations of Mathematical Physics, *IBM Journal of Research and Development*, *11*, 215–234, doi:10.1147/rd.112.0215.

Crutzen, P. J. (1970), The influence of nitrogen oxides on the atmospheric ozone content, *Q.J.R. Meteorol. Soc.*, *96*, 320.

Crutzen, P. J., I. S. A. Isaksen, and G. C. Reid (1975), Solar proton events - Stratospheric sources of nitric oxide, *Science*, *189*, 457–459, doi: 10.1126/science.189.4201.457.

Dobbin, A. L., E. M. Griffin, A. D. Aylward, and G. H. Millward (2006), 3-d gcm modelling of thermospheric nitric oxide during the 2003 halloween storm, *Ann. Geophys.*, *24*, 2403–2412.

Eather, R. H. (1967), Auroral Proton Precipitation and Hydrogen Emissions, *Reviews of Geophysics*, *5*, 207–285, doi:10.1029/RG005i003p00207.

Edgar, B. C., W. T. Miles, and A. E. S. Green (1973), Energy deposition of protons in molecular nitrogen and applications to proton auroral phenomena., *J. Geophys. Res.*, *78*, 6595–6606, doi:10.1029/JA078i028p06595.

Fahey, D. W., K. K. Kelly, D. M. Murphy, M. H. Proffitt, C. S. Eubank, M. K. W. Ko, G. V. Ferry, M. Loewenstein, and K. R. Chan (1989), Measurements of

nitric oxide and total reactive nitrogen in the Antarctic stratosphere - Observations and chemical implications, *J. Geophys. Res.*, *94*, 16,665–16,681, doi: 10.1029/JD094iD14p16665.

Farman, J. C., B. G. Gardiner, and J. D. Shanklin (1985), Large losses of total ozone in Antarctica reveal seasonal ClO_x/NO_x interaction, *Nature*, *315*, 207–210, doi:10.1038/315207a0.

Fell, C., J. I. Steinfeld, and S. Miller (1990), Quenching of N(2D) by O(3P), *J. Chem. Phys.*, *92*, 4768–4777, doi:10.1063/1.457694.

Forbush, S. E. (1946), Three Unusual Cosmic-Ray Increases Possibly Due to Charged Particles from the Sun, *Physical Review*, *70*, 771–772, doi: 10.1103/PhysRev.70.771.

Foster, J. C., J. M. Holt, R. G. Musgrove, and D. S. Evans (1986), Ionospheric convection associated with discrete levels of particle precipitation, doi: 10.1029/GL013i007p00656.

Frederick, J. E., and D. W. Rusch (1977), On the chemistry of metastable atomic nitrogen in the F region deducted from simultaneous satellite measurements of the 5200-A airglow and atmospheric composition, *J. Geophys. Res.*, *82*, 3509–3517, doi:10.1029/JA082i025p03509.

Funke, B., A. Baumgärtner, M. Calisto, T. Egorova, C. H. Jackman, J. Kieser, A. Krivolutsky, M. López-Puertas, D. R. Marsh, T. Reddmann, E. Rozanov, S.-M. Salmi, M. Sinnhuber, G. P. Stiller, P. T. Verronen, S. Versick, T. von Clarmann, T. Y. Vyushkova, N. Wieters, and J. M. Wissing (2011), Composition changes after the "halloween" solar proton event: the high-energy particle precipitation in the atmosphere (heppa) model versus mipas data intercomparison study, *submitted to Atmos. Chem. Phys.*

Hartley, W. N. (1880), On the probable absorption of solar radiation by atmospherico zone, *Chem.News*, *42*, 268.

Haynes, P. H., M. E. McIntyre, T. G. Shepherd, C. J. Marks, and K. P. Shine (1991), On the 'Downward Control' of Extratropical Diabatic Circulations by Eddy-Induced Mean Zonal Forces., *Journal of Atmospheric Sciences*, *48*, 651–680.

Heath, D. F., A. J. Krueger, and P. J. Crutzen (1977), Solar proton event - Influence on stratospheric ozone, *Science*, *197*, 886–889, doi:10.1126/science.197.4306.886.

Heelis, R. A., J. K. Lowell, and R. W. Spiro (1982), A model of the high-latitude ionospheric convection pattern, *J. Geophys. Res.*, *87*, 6339–6345, doi: 10.1029/JA087iA08p06339.

Herzberg, L. (1960), The Possible Importance of Nitric Oxide Formation during Polar-Cap Ionospheric Absorption Events, *J. Geophys. Res.*, *65*, 3505–+, doi: 10.1029/JZ065i010p03505.

Hines, C. O. (1997a), Doppler-spread parameterization of gravity-wave momentum deposition in the middle atmosphere. Part 1: Basic formulation, *Journal of Atmospheric and Solar-Terrestrial Physics*, *59*, 371–386, doi:10.1016/S1364-6826(96)00079-X.

Hines, C. O. (1997b), Doppler-spread parameterization of gravity-wave momentum deposition in the middle atmosphere. Part 2: Broad and quasi monochromatic spectra, and implementation, *Journal of Atmospheric and Solar-Terrestrial Physics*, *59*, 387–400, doi:10.1016/S1364-6826(96)00080-6.

Hong, S., and R. S. Lindzen (1976), Solar semidiurnal tide in the thermosphere, *Journal of Atmospheric Sciences*, *33*, 135–153, doi:10.1175/1520-0469(1976)033.

Huggins, W., and M. Huggins (1890), On a New Group of Lines in the Photographic Spectrum of Sirius, *Royal Society of London Proceedings Series I*, *48*, 216–217.

Hultqvist, B., M. Øieroset, G. Paschmann, and R. Treumann (1999), Magnetospheric Plasma Sources and Losses: Final Report of the ISSI Study Project on Source and Loss Processes of Magnetospheric Plasma, *Space Sci. Rev.*, *88*, doi: 10.1023/A:1017251707826.

Jackman, C. H., J. E. Nielsen, D. J. Allen, M. C. Cerniglia, R. D. McPeters, A. R. Douglass, and R. B. Rood (1993), The effects of the October 1989 solar proton events on the stratosphere as computed using a three-dimensional model, *Geophys. Res. Lett.*, *20*, 459–462, doi:10.1029/93GL00205.

Jackman, C. H., E. L. Fleming, and F. M. Vitt (2000), Influence of extremely large solar proton events in a changing stratosphere, *J. Geophys. Res.*, *105*, 11,659–11,670, doi:10.1029/2000JD900010.

Jackman, C. H., M. T. DeLand, G. J. Labow, E. L. Fleming, D. K. Weisenstein, M. K. W. Ko, M. Sinnhuber, and J. M. Russell (2005), Neutral atmospheric influences of the solar proton events in October-November 2003, *J. Geophys. Res. (Space Physics)*, *110*, 9–+, doi:10.1029/2004JA010888.

Jackman, C. H., R. G. Roble, and E. L. Fleming (2007), Mesospheric dynamical changes induced by the solar proton events in October-November 2003, *Geophys. Res. Lett.*, *34*, 4812–+, doi:10.1029/2006GL028328.

Jackman, C. H., D. R. Marsh, F. M. Vitt, R. R. Garcia, E. L. Fleming, G. J. Labow, C. E. Randall, M. López-Puertas, B. Funke, T. von Clarmann, and G. P. Stiller (2008), Short- and medium-term atmospheric constituent effects of very large solar proton events, *Atmospheric Chemistry & Physics*, *8*, 765–785.

Jackman, C. H., D. R. Marsh, F. M. Vitt, R. R. Garcia, C. E. Randall, E. L. Fleming, and S. M. Frith (2009), Long-term middle atmospheric influence of very large solar proton events, *J. Geophys. Res. (Atmospheres)*, *114*, 11,304–+, doi: 10.1029/2008JD011415.

Jones, R. A., and M. H. Rees (1973), Time dependent studies of the aurora-I. Ion density and composition, *Planet. Space Sci.*, *21*, 537–557, doi:10.1016/0032-0633(73)90069-X.

Jusinski, L. E., G. Black, and T. G. Slanger (1988), Resonance-enhanced multiphoton ionization measurements of N(^{2}D) quenching by O(^{3}P), *J. Chem. Phys.*, *92*, 5977.

Kallenrode, M. (2004), *Space physics : an introduction to plasmas and particles in the heliosphere and magnetospheres.*

Kazil, J. (2002), The University of Bern Atmospheric Ion Model: Time- Dependent Ion Modeling in the Stratosphere, Mesosphere and Lower Thermosphere, *PhD Thesis, University of Bern, Switzertland.*

Kertz, W. (1971), *Einführung in die Geophysik II.*

Kinnison, D. E., G. P. Brasseur, S. Walters, R. R. Garcia, D. R. Marsh, F. Sassi, V. L. Harvey, C. E. Randall, L. Emmons, J. F. Lamarque, P. Hess, J. J. Orlando, X. X. Tie, W. Randel, L. L. Pan, A. Gettelman, C. Granier, T. Diehl, U. Niemeier, and A. J. Simmons (2007), Sensitivity of chemical tracers to meteorological parameters in the MOZART-3 chemical transport model, *J. Geophys. Res. (Atmospheres)*, *112*, 20,302–+, doi:10.1029/2006JD007879.

Kockarts, G. (1980), Nitric oxide cooling in the terrestrial thermosphere, *Geophys. Res. Lett.*, *7*, 137–140, doi:10.1029/GL007i002p00137.

Krivolutsky, A., A. Kuminov, and T. Vyushkova (2005), Ionization of the atmosphere caused by solar protons and its influence on ozonosphere of the Earth during 1994 2003, *Journal of Atmospheric and Solar-Terrestrial Physics*, *67*, 105–117, doi:10.1016/j.jastp.2004.08.004.

Krivolutsky, A. A., A. V. Klyuchnikova, G. R. Zakharov, T. Y. Vyushkova, and A. A. Kuminov (2006), Dynamical response of the middle atmosphere to solar proton event of July 2000: Three-dimensional model simulations, *Advances in Space Research*, *37*, 1602–1613, doi:10.1016/j.asr.2005.05.115.

Li, X., and M. A. Temerin (2001), The Electron Radiation Belt, *Space Sci. Rev.*, *95*, 569–580.

López-Puertas, M., B. Funke, S. Gil-López, T. von Clarmann, G. P. Stiller, M. Höpfner, S. Kellmann, G. Mengistu Tsidu, H. Fischer, and C. H. Jackman (2005), HNO_3, N_2O_5, and $ClONO_2$ enhancements after the October-November

2003 solar proton events, *J. Geophys. Res. (Space Physics)*, *110*, 9–+, doi: 10.1029/2005JA011051.

Maeda, K., and A. C. Aikin (1968), Variations of polar mesospheric oxygen and ozone during auroral events, *Planet. Space Sci.*, *16*, 371–+, doi:10.1016/0032-0633(68)90153-0.

Marsh, D. R., S. C. Solomon, and A. E. Reynolds (2004), Empirical model of nitric oxide in the lower thermosphere, *J. Geophys. Res.*, *109*, A07,301, doi: 10.1029/2003JA010199.

Marsh, D. R., R. R. Garcia, D. E. Kinnison, B. A. Boville, F. Sassi, S. C. Solomon, and K. Matthes (2007), Modeling the whole atmosphere response to solar cycle changes in radiative and geomagnetic forcing, *J. Geophys. Res. (Atmospheres)*, *112*, 23,306–+, doi:10.1029/2006JD008306.

McKenzie, R. L., and P. V. Johnston (1984), Springtime stratospheric NO2 in Antarctica, *Geophys. Res. Lett.*, *11*, 73–75, doi:10.1029/GL011i001p00073.

McPeters, R. D. (1986), A nitric oxide increase observed following the July 1982 solar proton event, *Geophys. Res. Lett.*, *13*, 667–670, doi:10.1029/GL013i007p00667.

Minschwaner, K., and D. E. Siskind (1993), A new calculation of nitric oxide photolysis in the stratosphere, mesosphere, and lower thermosphere, *J. Geophys. Res.*, *98*, 20,401–20,412, doi:10.1029/93JD02007.

Mlynczak, M. G. (2000), A contemporary assessement of the mesospheric energy budget, in *Atmospheric science across the stratopause*, edited by D. E. Siskind, S. D. Eckermann, and M. E. Summers, no. 123 in Geophys. Monogr. Ser., pp. 37–52, AGU, Washington, DC.

Mul, P. M., and J. W. McGowan (1979), Merged electron-ion beam experiments. III - Temperature dependence of dissociative recombination for atmospheric ions NO/+/, O2/+/, and N2/+/, *Journal of Physics B Atomic Molecular Physics*, *12*, 1591–1601, doi:10.1088/0022-3700/12/9/011.

Noxon, J. F. (1978), Stratospheric NO2 in the antarctic winter, *Geophys. Res. Lett.*, *5*, 1021–+, doi:10.1029/GL005i012p01021.

Picone, J. M., A. E. Hedin, D. P. Drob, and A. C. Aikin (2002), NRLMSISE-00 empirical model of the atmosphere: Statistical comparisons and scientific issues, *J. Geophys. Res. (Space Physics)*, *107*, 1468–+, doi:10.1029/2002JA009430.

Porter, H. S., C. H. Jackman, and A. E. S. Green (1976), Efficiencies for production of atomic nitrogen and oxygen by relativistic proton impact in air, *J. Chem. Phys.*, *65*, 154–167, doi:10.1063/1.432812.

Possner, A. (2011), The Resolution Dependency of Simulated Tracer Transport into the Antarctic Polar Vortex in ECHAM6, *Master Thesis, University Edinburgh.*

Randall, C. E., D. E. Siskind, and R. M. Bevilacqua (2001), Stratospheric NO_x enhancements in the southern hemisphere vortex in winter/spring of 2000, *Geophys. Res. Lett.*, *28*, 2385–2388, doi:10.1029/2000GL012746.

Randall, C. E., V. L. Harvey, G. L. Manney, Y. Orsolini, M. Codrescu, C. Sioris, S. Brohede, C. S. Haley, L. L. Gordley, J. M. Zawodny, and J. M. Russell (2005), Stratospheric effects of energetic particle precipitation in 2003-2004, *Geophys. Res. Lett.*, *32*, 5802–+, doi:10.1029/2004GL022003.

Randall, C. E., V. L. Harvey, C. S. Singleton, P. F. Bernath, C. D. Boone, and J. U. Kozyra (2006), Enhanced NO_x in 2006 linked to strong upper stratospheric Arctic vortex, *Geophys. Res. Lett.*, *33*, 18,811–+, doi:10.1029/2006GL027160.

Randall, C. E., V. L. Harvey, C. S. Singleton, S. M. Bailey, P. F. Bernath, M. Codrescu, H. Nakajima, and J. M. Russell (2007), Energetic particle precipitation effects on the Southern Hemisphere stratosphere in 1992-2005, *J. Geophys. Res. (Atmospheres)*, *112*, 8308–+, doi:10.1029/2006JD007696.

Randall, C. E., V. L. Harvey, D. E. Siskind, J. France, P. F. Bernath, C. D. Boone, and K. A. Walker (2009), NO_x descent in the Arctic middle atmosphere in early 2009, *Geophys. Res. Lett.*, *36*, 18,811–+, doi:10.1029/2009GL039706.

Reagan, J. B., R. E. Meyerott, R. W. Nightingale, R. C. Gunton, R. G. Johnson, J. E. Evans, W. L. Imhof, D. F. Heath, and A. J. Krueger (1981), Effects of the August 1972 solar particle events on stratospheric ozone, *J. Geophys. Res.*, *86*, 1473–1494, doi:10.1029/JA086iA03p01473.

Reddmann, T., R. Ruhnke, S. Versick, and W. Kouker (2010), Modelling disturbed stratospheric chemistry during solar-induced NO_x enhancements observed with MIPAS/ENVISAT, *J. Geophys. Res.*, *115*, doi:10.1029/2009JD012569.

Rees, M. H. (1975), Processes and emissions associated with electron precipitation, in *Atmospheres of Earth and the Planets*, pp. 323–333.

Rees, M. H. (1982), On the interaction of auroral protons with the earth's atmosphere, *Planet. Space Sci.*, *30*, 463–472, doi:10.1016/0032-0633(82)90056-3.

Rees, M. H. (1989), *Physics and chemistry of the upper atmosphere*.

Reid, G. C., S. Solomon, and R. R. Garcia (1991), Response of the middle atmosphere to the solar proton events of August-December, 1989, *Geophys. Res. Lett.*, *18*, 1019–1022, doi:10.1029/91GL01049.

Roble, R. G. (1992), The polar lower thermosphere, *Planet. Space Sci.*, *40*, 271–297, doi:10.1016/0032-0633(92)90065-V.

Roble, R. G. (1995), Energetics of the mesosphere and thermosphere, in *The upper mesosphere and lower thermosphere: A review of experiment and theory*, edited

by R. M. Johnson and T. L. Killeen, no. 87 in Geophys. Monogr. Ser., pp. 1–21, AGU, Washington, DC.

Roble, R. G., and M. H. Rees (1977), Time-dependent studies of the aurora - Effects of particle precipitation on the dynamic morphology of ionospheric and atmospheric properties, *Planet. Space Sci.*, *25*, 991–1010, doi:10.1016/0032-0633(77)90146-5.

Roble, R. G., and E. C. Ridley (1987), An auroral model for the NCAR thermospheric general circulation model (TGCM), *Annales Geophysicae*, *5*, 369–382.

Roble, R. G., J. M. Forbes, and F. A. Marcos (1987a), Thermospheric dynamics during the March 22, 1979, magnetic storm. I - Model simulations. II - Comparisons of model predictions with observations, *J. Geophys. Res.*, *92*, 6045–6081, doi:10.1029/JA092iA06p06045.

Roble, R. G., E. C. Ridley, and R. E. Dickinson (1987b), On the global mean structure of the thermosphere, *J. Geophys. Res.*, *92*, 8745–8758, doi:10.1029/JA092iA08p08745.

Rohen, G., C. von Savigny, M. Sinnhuber, E. J. Llewellyn, J. W. Kaiser, C. H. Jackman, M. Kallenrode, J. Schröter, K. Eichmann, H. Bovensmann, and J. P. Burrows (2005), Ozone depletion during the solar proton events of October/November 2003 as seen by SCIAMACHY, *J. Geophys. Res. (Space Physics)*, *110*, 9–+, doi:10.1029/2004JA010984.

Rozanov, E., L. Callis, M. Schlesinger, F. Yang, N. Andronova, and V. Zubov (2005), Atmospheric response to NO_y source due to energetic electron precipitation, *Geophys. Res. Lett.*, *32*, 14,811–+, doi:10.1029/2005GL023041.

Rusch, D. W., and C. A. Barth (1975), Satellite measurements of nitric oxide in the polar region, *J. Geophys. Res.*, *80*, 3719–3721, doi:10.1029/JA080i025p03719.

Rusch, D. W., and J. Gerard (1980), Satellite studies of N/D-2/ emission and ion chemistry in aurorae, *J. Geophys. Res.*, *85*, 1285–1290, doi:10.1029/JA085iA03p01285.

Rusch, D. W., J. Gerard, S. Solomon, P. J. Crutzen, and G. C. Reid (1981), The effect of particle precipitation events on the neutral and ion chemistry of the middle atmosphere. I - Odd nitrogen, *Planet. Space Sci.*, *29*, 767–774, doi:10.1016/0032-0633(81)90048-9.

Sander, S. P., R. R. Friedl, A. R. Ravishankara, D. M. Golden, C. E. Kolb, M. J. Kurylo, M. J. Molina, G. K. Moortgat, H. Keller-Rudek, B. J. Finlayson-Pitts, P. H. Wine, R. E. Huie, and V. L. Orkin (2006), JPL 2006: Chemical kinetics and photochemical data for use in atmospheric studies Evaluation 15, *JPL Publ. 06-2*.

Schmidt, H., G. P. Brasseur, M. Charron, E. Manzini, M. A. Giorgetta, T. Diehl, V. I. Fomichev, D. Kinnison, D. Marsh, and S. Walters (2006), The HAMMONIA Chemistry Climate Model: Sensitivity of the Mesopause Region to the 11-Year Solar Cycle and CO2 Doubling, *Journal of Climate*, *19*, 3903–+, doi: 10.1175/JCLI3829.1.

Semeniuk, K., J. C. McConnell, and C. H. Jackman (2005), Simulation of the October-November 2003 solar proton events in the CMAM GCM: Comparison with observations, *Geophys. Res. Lett.*, *32*, 15–+, doi:10.1029/2005GL022392.

Seppälä, A., P. T. Verronen, E. Kyrölä, S. Hassinen, L. Backman, A. Hauchecorne, J. L. Bertaux, and D. Fussen (2004), Solar proton events of October-November 2003: Ozone depletion in the Northern Hemisphere polar winter as seen by GOMOS/Envisat, *Geophys. Res. Lett.*, *31*, 19,107–+, doi:10.1029/2004GL021042.

Seppälä, A., C. E. Randall, M. A. Clilverd, E. Rozanov, and C. J. Rodger (2009), Geomagnetic activity and polar surface air temperature variability, *J. Geophys. Res. (Space Physics)*, *114*, 10,312–+, doi:10.1029/2008JA014029.

Siskind, D. E., C. A. Barth, and R. G. Roble (1989a), The response of the thermospheric nitric oxide to an auroral storm. I - Low and middle latitudes, *J. Geophys. Res.*, *94*, 16,885–16,898, doi:10.1029/JA094iA12p16885.

Siskind, D. E., C. A. Barth, D. S. Evans, and R. G. Roble (1989b), The response of thermospheric nitric oxide to an auroral storm. II - Auroral latitudes, *J. Geophys. Res.*, *94*, 16,899–16,911, doi:10.1029/JA094iA12p16899.

Siskind, D. E., S. D. Eckermann, L. Coy, J. P. McCormack, and C. E. Randall (2007), On recent interannual variability of the Arctic winter mesosphere: Implications for tracer descent, *Geophys. Res. Lett.*, *34*, 9806–+, doi:10.1029/2007GL029293.

Solomon, S. (1999), Stratospheric ozone depletion: A review of concepts and history, *Reviews of Geophysics*, *37*, 275–316, doi:10.1029/1999RG900008.

Solomon, S., D. W. Rusch, J. Gerard, G. C. Reid, and P. J. Crutzen (1981), The effect of particle precipitation events on the neutral and ion chemistry of the middle atmosphere. II - Odd hydrogen, *Planet. Space Sci.*, *29*, 885–893, doi:10.1016/0032-0633(81)90078-7.

Solomon, S., R. G. Roble, and P. J. Crutzen (1982), Photochemical coupling between the thermosphere and the lower atmosphere. I - Odd nitrogen from 50 to 120 km, *J. Geophys. Res.*, *87*, 7206–7220, doi:10.1029/JC087iC09p07206.

Solomon, S., G. C. Reid, D. W. Rusch, and R. J. Thomas (1983), Mesospheric ozone depletion during the solar proton event of July 13, 1982. II - Comparison between theory and measurements, *Geophys. Res. Lett.*, *10*, 257–2260, doi: 10.1029/GL010i004p00257.

Solomon, S. C., and L. Qian (2005), Solar extreme-ultraviolet irradiance for general circulation models, *J. Geophys. Res. (Space Physics)*, *110*, 10,306–+, doi: 10.1029/2005JA011160.

Swider, W., and T. J. Keneshea (1973), Decrease of ozone and atomic oxygen in the lower mesosphere during a PCA event, *Planet. Space Sci.*, *21*, 1969–1973, doi:10.1016/0032-0633(73)90126-8.

Thorne, R. M. (1977), Energetic Radiation Belt Electron Precipitation: A Natural Depletion Mechanism for Stratospheric Ozone, *Science*, *195*, 287–289.

Thorne, R. M. (1980), The importance of energetic particle precipitation on the chemical composition of the middle atmosphere, *Pure and Applied Geophysics*, *118*, 128–151, doi:10.1007/BF01586448.

Vegard, L. (1939), Hydrogen Showers in the Auroral Region, *Nature*, *144*, 1089–1090, doi:10.1038/1441089b0.

Vegard, L. (1948), Emission spectra of night sky and aurora, *Reports of the Gassiot Committee, The Physical Society of London*, p. 82.

Verronen, P. T. (2006), Ionosphere-atmosphere interaction during solar proton events, *PhD Thesis, Helsinki, Finland: Finnish Meteorological Institute Contributions.*

Verronen, P. T., E. Turunen, T. Ulich, and E. Kyrölä (2002), Modelling the effects of the october 1989 solar proton event on mesospheric odd nitrogen using a detailed ion and neutral chemistry model, *Ann. Gepophys.*, *20*, 1967–1976.

Verronen, P. T., A. Seppälä, M. A. Clilverd, C. J. Rodger, E. Kyrölä, C.-F. Enell, T. Ulich, and E. Turunen (2005), Diurnal variation of ozone depletion during the October-November 2003 solar proton events, *J. Geophys. Res.*, *110*, doi: 10.1029/2004JA010932.

Weeks, L. H., R. S. Cuikay, and J. R. Corbin (1972), Ozone Measurements in the Mesosphere During The Solar Proton Event of 2 November 1969., *Journal of Atmospheric Sciences*, *29*, 1138–1142, doi:10.1175/1520-0469(1972)029.

Wissing, J. M., and M. Kallenrode (2009), Atmospheric Ionization Module Osnabrück (AIMOS): A 3-D model to determine atmospheric ionization by energetic charged particles from different populations, *J. Geophys. Res. (Space Physics)*, *114*, 6104–+, doi:10.1029/2008JA013884.

Wissing, J. M., M. Kallenrode, N. Wieters, H. Winkler, and M. Sinnhuber (2010), Atmospheric Ionization Module Osnabrück (AIMOS): 2. Total particle inventory in the October-November 2003 event and ozone, *J. Geophys. Res. (Space Physics)*, *115*, 2308–+, doi:10.1029/2009JA014419.

Wissing, J. M., M. Kallenrode, J. Kieser, H. Schmidt, M. T. Rietveld, M. McCready, and P. Erickson (2011), Atmospheric Ionization Module Osnabrück (AIMOS): 3. Comparison of electron density simulations by AIMOS/HAMMONIA and incoherent scatter radar measurements, *submitted to J. Geophys. Res. (Space Physics)*, *115*.

Zadorozhny, A. M., G. A. Tuchkov, V. N. Kikhtenko, J. Lastovicka, J. Boska, and A. Novak (1992), Nitric oxide and lower ionosphere quantities during solar particle events of October 1989 after rocket and ground-based measurements, *Journal of Atmospheric and Terrestrial Physics*, *54*, 183–192.

Zadorozhny, A. M., V. N. Kikhtenko, G. A. Kokin, G. A. Tuchkov, A. A. Tyutin, A. F. Chizhov, and O. V. Shtirkov (1994), Middle atmosphere response to the solar proton events of October 1989 using the results of rocket measurements, *J. Geophys. Res.*, *99*, 21,059–+, doi:10.1029/93JD03194.

Zhu, X., E. R. Talaat, J. B. H. Baker, and J. Yee (2005), A self-consistent derivation of ion drag and Joule heating for atmospheric dynamics in the thermosphere, *Annales Geophysicae*, *23*, 3313–3322.

Zipf, E. C., P. J. Espy, and C. F. Boyle (1980), The excitation and collisional deactivation of metastable N/2P/ atoms in auroras, *J. Geophys. Res.*, *85*, 687–694, doi:10.1029/JA085iA02p00687.

Acknowledgements

At first, I thank my supervisor Dr. Hauke Schmidt for many helpful discussions, for motivation, and for giving me the opportunity to work on this interesting topic. Concerning the latter, I also thank the Max Planck Institute for Meteorology. I thank the staff of MPI administration, CIS, the library, and the DKRZ "Beratungs-Team" for their kind and straightforward support.
I thank Prof. Dr. Guy Brasseur for very constructive discussions, scientific advise, and ideas.
For scientific support I also thank Jan Maik Wissing, May-Britt Kallenrode, Pekka Verronen, Dan Marsh, and all the members of the HEPPA community.
A special thank goes to all current and former colleagues from the MPI and the Meteorological Institute of the University Hamburg for discussing and solving scientific, programming, and technical problems. In particular, I thank Michael Botzet, Felix Bunzel, Stefan Hagemann, Stefan Kinne, Daniel Klocke, Sven Kotlarski, Stergios Misios, Norbert Noreiks, Ronny Petrik, Sebastian Rast, and Kevin Sieck.
I acknowledge the German science foundation (DFG) for founding the Priority Program CAWSES where this work has been included. I also acknowledge the DKRZ where HAMMONIA simulations were performed.
I'm deeply thankful to my family and Andrea's family for their support and confidence.

Most of all, I thank Andrea for all her love, encouragement, patience, and confidence.



ISSN 1614-1199